HYALURONAN POLYMER BRUSH STRUCTURE, TOPOGRAPHICAL CONTROL, AND ITS RESPONSE TO THE ENVIRONMENT: CHARACTERIZING A NOVEL ULTRA-THICK BIOMATERIAL

A Dissertation
Presented to
The Academic Faculty

by

Jessica L. Faubel

In Partial Fulfillment
of the Requirements for the Degree
Doctor of Philosophy in the
School of Physics

Georgia Institute of Technology
May 2021

HYALURONAN POLYMER BRUSH STRUCTURE, TOPOGRAPHICAL CONTROL, AND ITS RESPONSE TO THE ENVIRONMENT: CHARACTERIZING A NOVEL ULTRA-THICK BIOMATERIAL

Approved by:

Dr. Jennifer E. Curtis, Advisor
School of Physics
Georgia Institute of Technology

Dr. Peter J. Yunker
School of Physics
Georgia Institute of Technology

Dr. Blair K. Brettmann
School of Materials Science and Engineering, School of Chemical and Biomolecular Engineering
Georgia Institute of Technology

Dr. David Zeb Rocklin
School of Physics
Georgia Institute of Technology

Dr. James C. Gumbart
School of Physics
Georgia Institute of Technology

Date Approved: [April 05, 2021]

To my dear husband, Josh Faubel, who lovingly supports all my pursuits.

ACKNOWLEDGEMENTS

I wish to express my deepest appreciation to my advisor, Dr. Jennifer Curtis, for her insight and mentorship over the last four years. Her guidance has been invaluable and I will forever be grateful that she took me in. I would also like to thank my committee members for their discussion, ideas, and feedback; without which this thesis would have suffered. I am also grateful to Dr. Wenbin Wei for his training, guidance, and friendship throughout my graduate studies. My sincere thanks to my lab mates, Hemaa Selvakumar and Shlomi Cohen, for stimulating scientific discussions and friendship. I have also appreciated the contributions of Riddhi Patel and Ellen Park to the data collection and technique development in this thesis. I would also like to thank the teachers throughout the years who have instilled in me a love of learning and a love of science: Leigh Hethcox, Gary Headrick, Kelli Schuyler, Bill Schuyler, and Dr. Mark C. Spraker.

Without the generous donation of materials from Dr. Paul Weigel, this thesis work would be impossible. I am also grateful for the financial support from NSF DMR #0955811, #1709897 and NSF PoLS SRN # 1205878.

Last, but not least, I thank my family and friends. My parents, Suzanne and Donald Easley, encouraged my learning and molded my work ethic from a young age. My friends have been some of my biggest cheerleaders over the last couple years. My son, Robin, for his smiles after long days. Finally, I'll be forever grateful to my husband, Josh, for supporting my decision to change careers and encouragement throughout this long process.

TABLE OF CONTENTS

LIST OF TABLES

LIST OF FIGURES

LIST OF ABBREVIATIONS

AFM	Atomic Force Microscopy
HA	Hyaluronic Acid (or Hyaluronan)
GlcNAc	N-acetylglucosamine
GlcUA	D-glucuronic acid
UV	Ultraviolet
HAS	Hyaluronan Synthase
seHAS	*Streptococcus equisimilis*
E. coli	*Escherichia coli*
UDP	Uridine diphosphate
SCF	Self-consistent field
SEC-MALLS	Size Exclusion Chromatography – Multi Angle Laser Light Scattering
PEI	Polyethylenimine
EDC	1-Ethyl-3-(3-dimethylaminopropyl)carbodiimide
NHS	N-hydroxysuccinimide
SDS	Sodium dodecyl sulfate
EDTA	Ethylenediaminetetraacetic acid
ECD	Event Charge Deficit
MW	Molecular Weight
LC-MS	Liquid chromatography–mass spectrometry
DTT	Dithiothreitol
NA	Numerical Aperture
STDEV	Standard Deviation

PBS	Phosphate buffered saline
BSA	Bovine Serum Albumin
GA	Glutaraldehyde
GlcNAz	N-azidoacetylglucosamine tetraacylated
M_N	Number averaged molecular weight
M_W	Weight averages molecular weight
R_H	Hydrodynamic radius
XPS	X-ray Photoelectron Spectroscopy
ELISA	Enzyme-linked immunosorbent assay
HPLC	High-Performance Liquid Chromatography
NMR	Nuclear Magnetic Resonance
DLS	Dynamic Light Scattering
CV	Coefficient of Variation
PEG	Polyethylene glycol
DMSO	Dimethyl sulfoxide
ROS	Reactive Oxygen Species
GT	Georgia Institute of Technology
PDMS	Polydimethylsiloxane

SUMMARY

Polymer brushes are dense assemblies of end-grafted polymers which have a wide range of applications in lubrication, colloidal stabilization, surface functionalization, and fundamental polymer physics. This thesis focuses on developing and leveraging a new class of polymer brush generated by the enzyme, hyaluronan synthase. The hyaluronan brushes are tunable and can reach heights of up to ~22 um – 2 orders of magnitude thicker than most brushes and more than one order of magnitude thicker than any previously reported brush. These ultra-thick brushes enable unprecedented characterization through direct visualization with confocal microscopy, as well as manipulation for future applications.

In this thesis, I first establish control over brush synthesis, the ability to stop and start the brush growth, and demonstrate the inherent regenerative capability of the brushes. Then, building on those results, my focus is to elucidate and manipulate the internal brush structure and response to stimuli by exploiting the rapid characterization capabilities of confocal microscopy. Techniques to fluorescently label the brush were developed to acquire high-resolution concentration profiles of the hyaluronan brush versus brush height. The profiles are consistently convex and decay in an exponential-like fashion consistent with theoretical predictions for polydisperse brushes. When coupled with experimentally acquired molecular weight distribution, these profiles can be used to directly test theoretical polymer physics, especially in the domain of polyelectrolytes where theory is still being established. Next, spatial manipulation of the local brush grafting density was developed to enable precision patterning and sculpting of the topography of the thick brush. Careful

studies revealed that the mechanism behind the grafting density alteration arises from the indirect laser deactivation of the HA synthase enzymes via the generation of reactive oxygen species from light-substrate interactions, specifically the bacterial membrane fragments containing the HA synthase. The patterning is most efficient at shorter wavelengths (405nm), but also can be achieved using wavelengths in the visible spectrum. The same technique can also be used to make binary-brush landscapes consisting of brush-rich and brush-free regions. The stimulus-responsiveness of the brush was explored as both an exercise in polymer physics, as well as for future materials applications. In response to varying salt concentration ($NaNO_3$), the hyaluronan brushes reversibly traverse through the osmotic and salted brush regimes, while irreversibly collapsing in the presence of 90% ethanol, a poor solvent.

Groundwork for future studies of the time-dependent nature of the stimulus response and of the dynamics of flow over the brushes has been established. These studies will be integral for potential applications such as anti-microbial implant coatings, where understanding the stimulus response time and flow-dependent decay of the brush will be key. The knowledge and tools gained in this work will aid in a spectrum of rich research arenas ranging from polymer physics to cell biophysics to materials science.

CHAPTER 1. INTRODUCTION

Polymer brushes are a result of end-grafting polymer chains where dense grafting causes deformation of the chains and extension away from the surface, forming a polymer brush.[1] This structure is a result of balancing elastic and entropic forces, steric constraints, as well as Van der Waals and electrostatic forces.[2] When polyelectrolytes, charged polymers, are used to form a polymer brush, stretching away from the surface is even stronger than with non-charged polymers and the brush size and configuration is sensitive to additional stimuli, such as ionic strength,[3] pH,[4] solvent,[5-8] and ion valency.[5-7]

Polyelectrolyte brushes are generally prepared through grafting to (tethering preformed polymers to the surface) or grafting from (synthesizing the polymers from an initiator on the surface) approaches and are typically on the scale of tens to hundreds of nanometers, with rarer realizations into single-digit microns.[9-12] These types of brushes have been employed as antifouling surfaces,[8] used to control wettability and lubrication,[13] and developed as biochemical sensors.[14, 15] As the importance of brushes for these applications has increased, so has interest in the physical nature of the conformational changes and molecular level phenomena occurring as the local environment is changed.

In examining brush height (or the thickness of the polymer layer) and stimuli-responsive behavior, the height is measured before and after changes in the environmental conditions. This is typically done through surface forces apparatus measurements,[3, 16] ellipsometry,[17] quartz crystal microbalance with dissipation monitoring,[9, 17] solution

phase atomic force microscopy (AFM), [7, 18] and fluorescent labeling of polymer chain ends.[19] Due to the small size of the brushes, experimental studies are typically limited to solely brush height measurements, though some measurements of polymer density as a function of distance from the grafting surface have been made through neutron reflectivity,[11] of 2D collapsed brush structure through AFM,[7] and of the kinetics of brush collapse and expansion with ellipsometry.[17] It remains challenging to characterize detailed 3D brush conformations and time-dependent behavior of the brush when exposed to new stimuli.

As a member of a growing class of polymer brushes and films fabricated by enzymes,[20, 21] our lab recently devised a microns-thick polymer brush assembly composed of the polyelectrolyte hyaluronic acid (HA or hyaluronan), generated by the enzyme hyaluronan synthase.[22] HA is an anionic biopolymer composed of alternating N-acetyl-D-glucosamine and D-glucuronic acid that is present in a large number of human tissues and fluids and is a common material for tissue engineering and therapeutics.[23-25] In nature, HA may be found in the cell glycocalyx, assembled in a brush configuration from a cell surface through the enzyme HA synthase. HA synthase can generate polymers up to 25 microns (10 MDa) via addition of a monomer at the base of the polymer brush and extrusion of the HA polymer further through the cell membrane, a mechanism quite distinct from grafting to or grafting from. [22, 26-28]

Due to the incredibly long polymers that HA synthase can generate, the brush height can be tuned from a few hundred nanometers to tens of microns by adjusting polymerization time, ionic strength or solvent. These results showcase the potential for leveraging nature’s biological machines in designing extraordinary functional materials.

The main advantage in this system arises from the order of magnitude increase in brush height, which provides more substrate/volume for interactions, access to more complex topographies, and direct visual characterization of the brush. This also enhances the scale of conformational changes by the polymer chains when solution conditions, such as solvent quality, are changed.

The aim of this work is to probe the internal structure and response of the hyaluronan polymer brushes to stimulus. Fundamental polymer physics underlies existing theory for the distribution of polymers within the brush and general brush response to environmental changes. The ultra-thick nature of the HA brushes fills an empty niche of polymer brushes whose characteristics can be directly studied, time-dependently monitored, and modified with ease. Specifically, the work outlined here demonstrates that the grafting density (and hence both brush height and topography) can be controlled and modified, the polymer concentration profile within the brush is a convex, exponential-like shape that is consistent with theoretical predictions for polydisperse brushes, multiple paths to fluorescently labeling the HA contained within the brush including the successful incorporation of an azide modified monomer into the synthesized HA that will open up the door to all the possibilities afforded by click chemistry, and that the brushes respond to environmental changes in a predictable way despite their incredible thickness. It also lays the foundation for future study of time-dependent changes due to solvent quality and flow, dynamic changes in polymer concentration profiles, and even biomedical applications such as cell-substrate viability and biofilm interaction.

CHAPTER 2. BACKGROUND

2.1 Hyaluronan

Hyaluronan (HA) is a glycosaminoglycan composed of alternating N-acetylglucosamine (GlcNAc) and D-glucuronic acid (GlcUA) (Figure 1). It is considered a weak polyelectrolyte due to the carboxyl group on the D-glucuronic acid being partially dissociated in most solutions (pH 2.8-12, pKa of 3-4) [29, 30] with increasing dissociation with increasing pH [31].

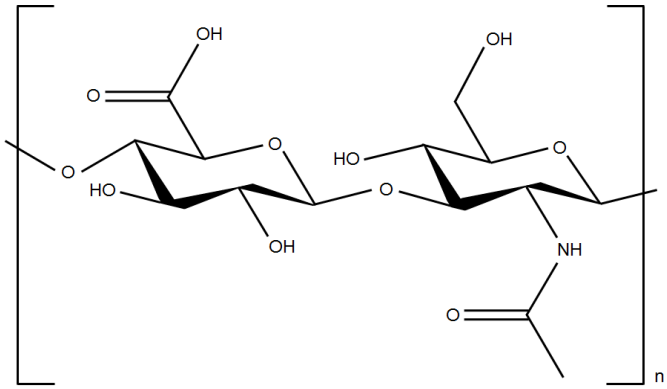

Figure 1. Chemical skeleton of a hyaluronan disaccharide. Created with Chem3D and Microsoft PowerPoint.

HA can be found in the human epidermis, synovial fluids, and the vitreous humor.[32-34] In a 70 kg individual, there are 15 g of HA, one-third of which is replenished every day.[35] HA in the skin is digested and replenished every 1-2 days.[36] It has viscoelastic and hydrophilic properties which aids in the lubricating and cushioning properties of synovial fluid.[37] It can be found on six bacteria species where they have a thick extracellular capsule made of hyaluronan that protects them from antibacterial agents

and immune cells.[32-34].HA is also a main component in the polymer brush coats of epithelial cells.[38]

Due to the basic linear structure of HA and its biocompatibility, HA has been widely used in therapeutics. Mice who experienced a decrease in hyaluronan production in the skin based on UV irradiation showed in increase in skin moisture when low molecular weight hyaluronan was administered orally.[39] After injecting hyaluronic acid into the knee joints of 25 patients with rheumatoid arthritis, a study found significant improvement in pain and inflammation.[40] High-molecular weight hyaluronan (4 MDa), such as that used by Campo et al, can be used as an anti-inflammatory since it has the effect of modulating receptors which would normally result in a cascade of signaling that results in pro-inflammatory cytokine production.[41].It can be made into a hydrogel and used as a cell growth scaffold or aid in drug delivery.[42] This technique can be powerful in wound healing. Given that low molecular weight hyaluronan can sometimes be a factor in causing inflammation during wound healing, one study showed that when complexed with high-molecular weight hyaluronan, wound closure rates increased when compared to non-complexed forms.[43]

2.2 Hyaluronan synthase

HA is made by the transmembrane enzyme hyaluronan synthase (HAS). Hyaluronan can be made intracellularly and then expelled into the area surrounding the cells, as is the case for HA found in synovial fluid.[44] HA can also be made by synthases found embedded in the cell membrane and where it is extruded out of the cell during its fabrication, much like a store receipt being extruded from a register. All class 1 HAS

enzymes processively build the hyaluronan and share sequence and membrane domain similarities, whereas a class 2 HAS enzyme (of which there is only one known), is non-processive and has a different gene sequence which results in very different membrane incorporation.[27, 45] HAS derived from the bacteria *Streptococcus equisimilis* (seHAS) is the particular isoform of a class 1 HAS used in the system described in this report. In 1997, it was shown that by transfecting Sure II *E. coli* with the seHAS gene, the *E. coli* will synthesize HA when the necessary substrates are provided.[46] These genetically-modified *E. coli* can subsequently be broken up and the fragments of their HAS-rich membranes can be collected. In this way, extensive work has been completed in an attempt to understand how the enzyme makes HA, characterize its kinetics, and its limitations.[27, 45, 47-49] It is now understood that the enzyme facilitates the generation of HA via the following reactions[27]

$$(HA_d)\text{-}UDP + GlcUA\text{-}UDP \rightarrow UDP + (HA_d)\text{-}GlcUA\text{-}UDP \quad (1)$$

$$(HA_d)\text{-}GlcUA\text{-}UDP + GlcNAc\text{-}UDP \rightarrow UDP + (HA_d)\text{-}GlcUA\text{-}GlcNAc\text{-}UDP \quad (2)$$

with energy supplied by uridine diphosphate (UDP) and in the presence of magnesium ion cofactors, where d indicates the number of disaccharide units in the HA chain.[50] HA is assembled processively, where the UDP-sugar monomers are supplied by the cell and the resulting HA chain is extruded out of the cell through the HA synthase (Figure 2).

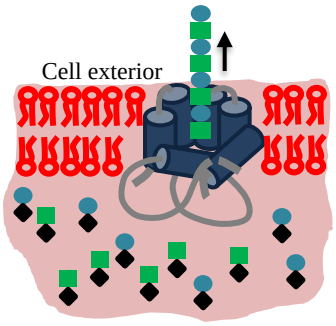

Figure 2. HA synthase (blue) embedded in a bacterial membrane (red) polymerizes and extrudes the growing HA polymer through the pore. The sugar substrates UDP-GlcUA (circle) and UDP-GlcNAc (square) are alternatively bound at the intracellular glycotransferase sites where processive assembly takes place. HA is extruded at an average rate of ~1 nm/s corresponding to 1 disaccharide/s.

2.3 Polymer brushes

Polymer brushes are structures of end-grafted polymers densely arranged on a surface such that the distance between their anchor points is less than the radius of gyration.[1, 51] Due to the close quarters resulting in steric, electrostatic, and van der Waals interactions, the polymers stretch up and away from the grafting surface.[2] The distance between the grafting surface and the edge of this polymer layer is the brush thickness or height. Generally, if the distance between the polymer's anchor points, or the grafting density, increases then the height of the brush layer increases according to the scaling law in Equation 3 [52]:

$$H \sim l_c \sigma^{\frac{1}{3}} \tag{3}$$

Polymer brushes are ubiquitous in nature. They can be found surrounding some bacteria, forming a protective capsule that serves to inhibit antibiotics from reaching the membrane.[53, 54] They can also be found surrounding animal epithelial cells and have

been shown to aid in transmitting exterior forces to the cytoskeleton, and serve as a protective, permeability barrier in vascular tissues.[55] They are also widely used to tune the properties of surfaces and give improved functionality, including tuning surface wettability [56], controlling particle and protein penetration [57], drug delivery [58], and stabilizing colloidal suspensions as surfactants [57].

The method of brush fabrication depends on the polymer and the desired qualities of the final brush. With the grafting-to method, existing polymers can be anchored to binding sites on a surface. With the grafting-from method, polymers are synthesized from an initiator on the surface. Higher grafting densities can be achieved with grafting-from methods because grafting to methods are limited by steric hindrances which restrict the number and sizes of polymers that can bind to a surface. Brushes can be made of a single polymer type, mixed polymers, and multiple types of polymers synthesized in layers, as demonstrated in Figure 3.[57]

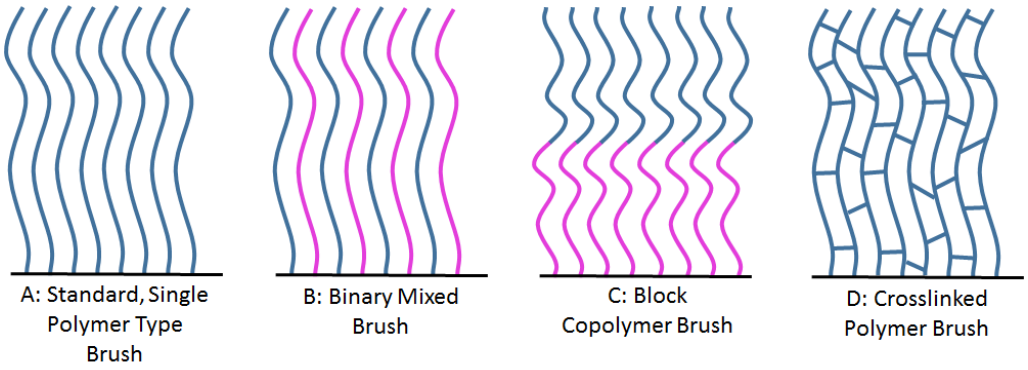

Figure 3. Schematics of common brush styles and configurations. A) Standard polymer brush constructed of one type of polymer, like the brushes described in this proposal. B) Brush made of a mixture of two polymer types. C) Brush fabricated in

layers where each layer of brush is made of a different type of polymer. D) Standard polymer brush that has been crosslinked. Figure adapted from [59].

2.3.1 Monodisperse and polydisperse brush structure

The internal structure of polymer brushes remains a relatively open question. How do the individual polymers arrange themselves? How does the balance between elasticity, entropy, osmotic pressure, and excluded volume determine the conformation of the polymers and therefore the overall brush structure and final properties? How does the grafting density and molecular weight affect the brush? Many of these questions have been studied individually, in pairs, or in theoretical treatments, but it's hard to answer all these questions about one system.

The dispersity of a system is a measure of how heterogenous the sizes of the molecules are in the sample. The polydispersity index (PDI) is a measure of the distribution of sizes as determined by:

$$PDI = \frac{M_W}{M_n} \tag{4}$$

where M_W is the weight averaged molecular weight and M_n is the number averaged molecular weight. A value close to 1 for the PDI indicates a uniform chain length for the polymers in the sample, aka a monodisperse sample. As the PDI begins to deviate from unity, the polymer sample will become polydisperse.

Theoretical predictions for monodisperse polymer brushes were first presented by de Gennes. de Gennes *et al* predicted monomer concentration profiles would appear as box profiles, where the density is constant throughout the brush until the edge is reached.[52,

60] After the polymer physics community transitioned to self-consistent field (SCF) models, the predicted concentration profile shifted from a box to a parabolically decreasing density out to zero at the edge (Figure 4A) where the height of the brush is predicted to scale as in Equation 3. The free ends of the polymers are expected to be found throughout the brush (Figure 4B), with no height being free of polymer ends within the brush, or dead zones.[1, 61]

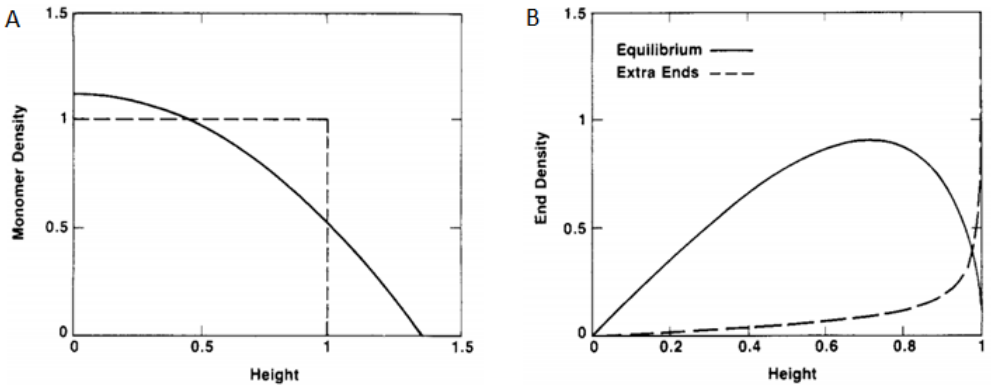

Figure 4. A) The monomer density profiles for the box-profile (dotted line) and parabolic profile (solid line). B) The density of free ends derived from self-consistent field theory. The solid line represents the equilibrium state of the brush. The dotted line can be ignored for uncompressed brushes. These images were originally published by Milner et al [1, 61]. Reprinted here under the Attribution-NonCommercial 4.0 International (CC BY-NC 4.0).

Polymer brushes composed of monodisperse polymers have been widely studied, both theoretically [1, 60, 62] and experimentally [63, 64]. Polydisperse polymer brushes have been studied theoretically, but there are not extensive experimental studies to verify theory. Compared to monodisperse brushes, significantly more open questions remain in the field related to polydisperse brushes and they pertain to the physical structure and conformation of the polymers within the brush, how that structure is affected by confinement and underlying surface topography, and the collapse dynamics.

Brushes comprised of two contour lengths, or bimodal brushes, are frequently used as model systems for polydisperse brushes. Theoretical work predicts that longer chains will always find their free ends furthest from the grafting surface, compared to shorter chains in the brush, as is demonstrated in Figure 5A.[65, 66] In a bimodal brush, this results in two regions. The first region is located closest to the grafting layer and is where all the shorter chains are located. The longer chains will be more strongly stretched in this region, but beyond this first region, only the monomers belonging to longer chains will be present, Figure 5B.[63, 64] A more physically realistic model of what happens to the longer chains beyond the region of shorter chains was described by Vos *et al* where the longer chains have an extended stem-like conformation in the region of shorter chains and a more collapsed conformation in the upper area, Figure 5C.[67]

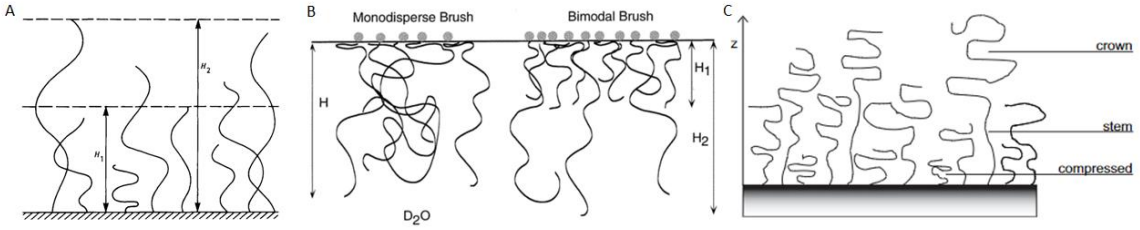

Figure 5. A) Schematic representation of the distribution of ends in a bimodal brush. B) Schematic representation of the segregation of different molecular weight polymers in a bimodal brush vs a monodisperse brush. C) Schematic representation of the stem-and-flower-like conformation of long polymers in the presence of short polymers in a bimodal brush. These images were originally published by, respectively, Birshtein et al [65, 66], Currie et al [63, 64], and Vos et al [67]. Reprinted here under the Attribution-NonCommercial 4.0 International (CC BY-NC 4.0).

If the difference between the chain lengths in a bimodal brush is small, then the density profile will be similar to the parabolic profile of a monodisperse brush (Figure 6A). As the difference in polymerization between the two chains increases, the profile changes to incorporate two parabolic profiles that overlap.[67] With increasing differences in the

chain lengths, the separate parabolic profiles can begin to be distinguished and the bump in the plot becomes more pronounced. With increasing polydispersity and more variability in chain lengths, the demarcation between these regions becomes fuzzier and the layers begin to blend together. The average height of the brush increases and the monomer concentration profile shifts from a convex parabolic-like profile to a concave profile (Figure 6B).[67] This is due to the longer chains being strongly stretched by the presence of short chains.[65, 67]

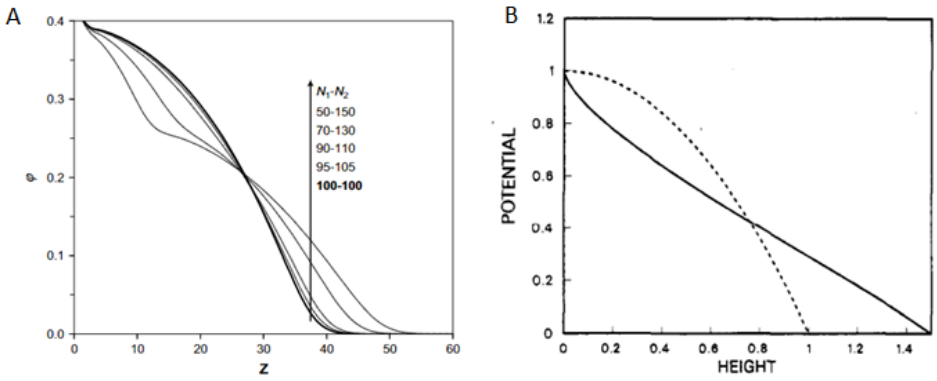

Figure 6. A) The effect of increasing difference in polymerization in a bimodal brush on the monomer density profile. The solid line represents a monodisperse brush with all polymers of N = 100 units. Increasing differences in N yields more pronounced deviations from the pure parabolic profile. B) The effect on the monomer density profile due to changing from a monodisperse brush (dotted line) to a polydisperse brush (solid line). These images were originally published by, respectively, Vos et al [67] and Milner et al [65]. Reprinted here under the Attribution-NonCommercial 4.0 International (CC BY-NC 4.0).

2.3.2 Polyelectrolyte brushes

The choice of polymer used in the brush will often dictate the type of functionality of the brush and its ability to respond to the environment. Neutral brushes have been fairly well understood for quite some time and experimental results validate existing theoretical work [68, 69]. If the polymer chosen is a polyelectrolyte, having ionizable groups present,

the resulting brush will have additional functionality. The charge of a weak polyelectrolyte is easily controlled by pH, especially if it has carboxyl side groups, where as a strong polyelectrolyte will have a charge that is independent of pH.[59] Weak polyelectrolytes are particularly responsive to changes in ionic strength, ion valency, pH, and solvent quality due to the presence of functional groups that can carry a charge.[5, 70-72] The strength of the response of the polyelectrolyte brush layer is a result of how easily the charge on the polymer can be manipulated. Only recently, since the late 1980's to mid 1990's, have weak polyelectrolyte polymer brushes begun to be studied in earnest. Theoretical work on polyelectrolyte brushes is interested in the scaling relationships between brush thickness, average polymer conformation, and key solvent characteristics.[68, 70, 73, 74] Experimental studies of polyelectrolyte brushes tend to focus more on their interesting solvent responses [64, 75], effects of interacting polyelectrolyte brushes [76, 77], collapse structures [78, 79], and rather than their internal structure, leaving an opening for the studies outlined in this work.

2.4 The hyaluronan brush

Parts of the following subheading have been previously published:

Wei, W., Faubel, J.L., Selvakumar, H. et al. **Self-regenerating giant hyaluronan polymer brushes**. *Nat Commun* **10**, 5527 (2019). DOI: 10.1038/s41467-019-13440-7

2.4.1 Immobilization of hyaluronan synthase membranes

Hyaluronan synthase activity is robustly preserved in fragments of bacterial membrane. The activity of the HA synthase within the membranes can be dynamically

switched on and off by controlling the availability of Mg^{2+} or the UDP-sugars used by the enzyme to make HA [80, 81]. Previous studies used HA synthase-rich membrane fragments to investigate the function and kinetics of HA synthase, including the Group C *Streptococcus equisimilus* HA synthase used in this thesis [80, 82]. The work also extensively characterized the molecular weight distribution produced by the HAS fragments using SEC-MALS (size exclusion chromatography – multi angle light scattering). Those studies show the HAS fragments produce a wide distribution of HA sizes, whose average molecular weight increases with time and plateaus at 4 h to 8 h with an average size of ~6 MDa (Mw).

Membrane fragments (~145 nm in diameter via light scattering and SEM imaging) immobilization onto surfaces is achieved by first coating glass surfaces with polyethyleneimine (PEI) and then activating with glutaraldehyde. The primed surface is used to crosslink with the numerous proteins in the membrane fragments (Figure 7). Surprisingly, despite the underlying glass interface, our data demonstrate that the UDP-sugar monomers must have access to the enzymes, which still manage to rapidly polymerize and extrude HA into the surrounding area. Indeed, the resultant HA at the interface is so extensive that it visibly excludes 200 nm particles from the underlying surface and establishes a giant gap of > 20 μm in low ionic strength conditions (Figure 8c, t_{growth}=16 h).

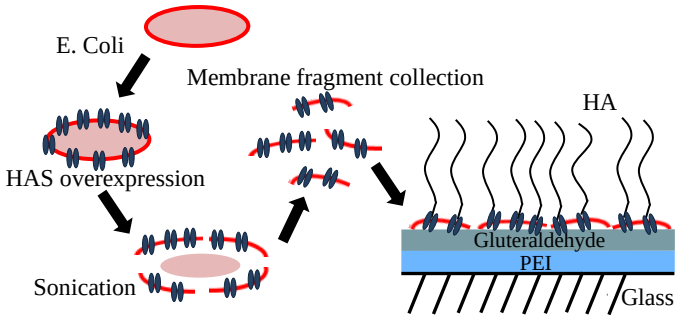

Figure 7. Preparation and immobilization of membrane fragments carrying HA synthase to glass substrates.

The ultrathick HA synthase generated brushes afford unusual access to spatial characterization via high resolution confocal microscopy. Measurements indicated that the brush height ranges from a few microns at early times up to 10.6 ± 1.0 μm after 16 h in physiological conditions (high ionic strength, 130 mM, ± is st. dev.) on planar surfaces (Figure 8A). On 8μm microspheres, the maximal spherical brush height is significantly lower, plateauing at 4.3 ± 0.4 μm after 8 h (130 mM, ± is st. dev.). The height difference between the planar and spherical surfaces likely arises from geometrical affects, which on positively curved surfaces like spheres leads to more accessible free volume as the polymers extend radially.[83] The HA brush height was determined using particle exclusion assays (Figure 8B), a common approach to characterizing HA-rich glycocalyx on cells.[84-86] Fluorescently labeled polystyrene nanoparticles >100 nm stop roughly at the interface of the brush. Therefore, we used 200 nm fluorescent nanoparticles to locate the top of the brush.

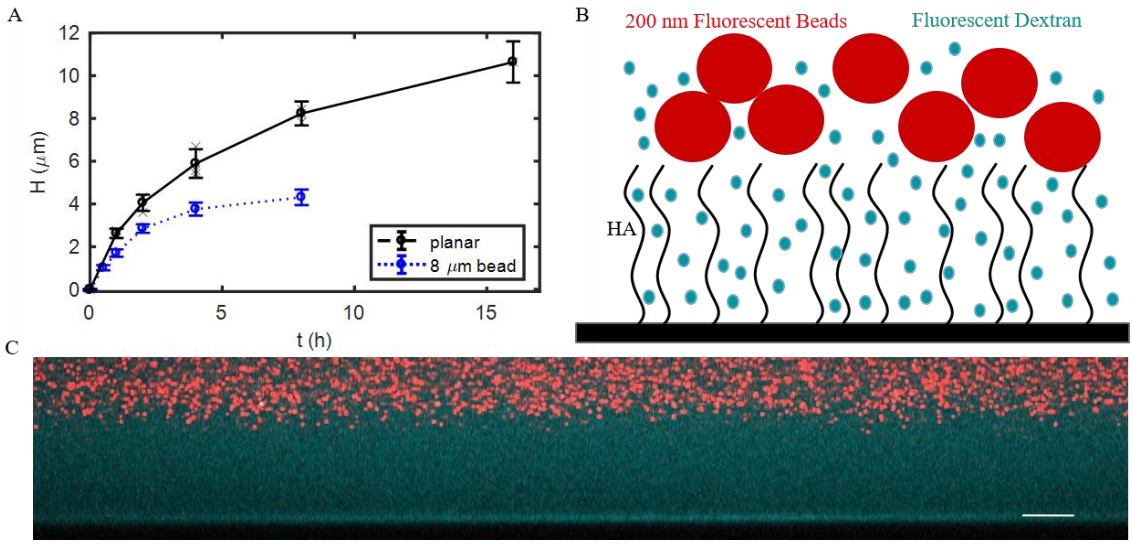

Figure 8. A) Dynamic growth of hyaluronan brushes generated by HA synthase (150 mM). The brush height reaches 2.62 ± 0.2 µm (st. dev.) in just 1 h (planar) in high ionic strength conditions. After 16 h the brush is 10.6 ± 1.0 µm (st. dev.). Measurements from individual brushes are shown in grey, averages and standard deviations are indicated in black. N_planar = 3 brushes, 12 regions per sample, except 16 h brush which is just 1 brush. The spherical brush plateaus at much earlier times (~ 5 h) at a final height of 4.3 ± 0.4 µm (st. dev.). N_spherical > 120 for spherical brush height measurements. All scale bars are 5 µm. B.) Particle exclusion assay. 200 nm fluorescent beads are excluded from the HA brush, outlining the top edge of the brush. Fluorescent dextran (~10kDa) can penetrate through the brush and allow visualization of the gap between the 200 nm fluorescent beads and the black, non-fluorescent glass under the brush. C) Side view confocal image of HA brush grown for 16 h and imaged at low ionic strength (1.5 mM). The brush region is imaged by the contrast generated by its accessibility to fluorescent dextran (cyan, 10 kDa), but exclusion of nanoparticles (red, 200 nm). The brush height is ~ 22 µm. Scale bar 10 µm.

2.4.2 Unique grafting style

This enzyme-generated giant polymer brush is distinct from traditional polymer brushes in several ways. Notably, rather than grafting-from or grafting-to the surface, the HA brush is generated by a transmembrane protein which extrudes the HA through a protein pore. The enzyme is able to polymerize much higher molecular weight molecules

than most other techniques such as free radical polymerization with rare exception.[87, 88] Further, the polymer grows from the base of the interface rather than the tip of the polymer. The extraordinary brush height results in the unusual ability to directly visualize the brush with detailed spatial resolution. Last, but importantly, the enzymes enable the option of brush regeneration.

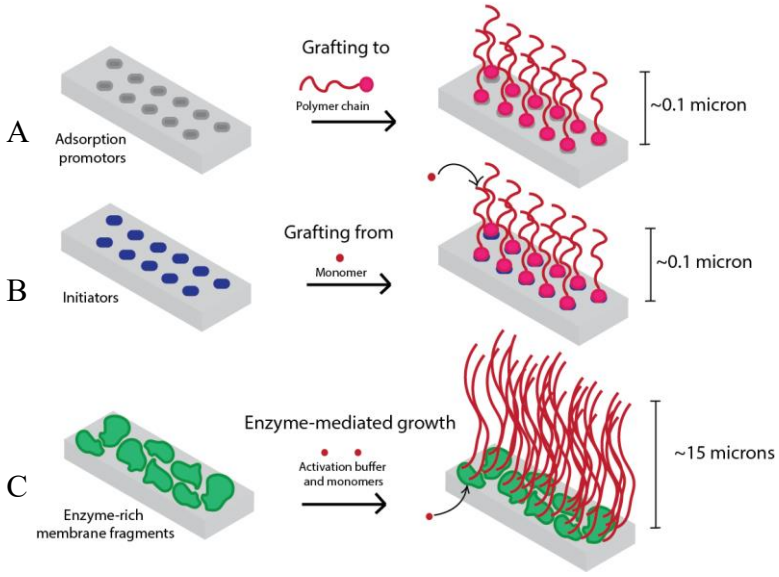

Figure 9. Illustration of three methods to form polymer brushes. A) Grafting to, where a pre-formed polymer chain adsorbs on the surface, B) Grafting from, where the chains are polymerized from initiators on the substrate and monomers are added to the growing chain end and C) Enzyme-mediated growth, where chains are polymerized from enzyme-rich membrane fragments on the substrate and monomers are added at the base of the growing chain.

2.4.3 Nanoparticle penetration

Examination of the size-dependent penetration of the brushes by nanoparticles has revealed that under physiological conditions, 200 nm and larger diameter particles are repelled from entry into the brush, while 100 nm and smaller penetrate to varying extents. Dilute 20 nm particles penetrate the brush, with approximately 30% of the bulk concentration value reaching the surface. Fluorescent negatively charged dextran (~10

kDa, ~ 5 nm diameter[89]) shows a 30-50% approximately linear decrease in intensity in the presence of 200 nm and 20 nm particles at high ionic strength. Traditional dense synthetic brushes exclude molecules [90], but the partial penetration into these HA brushes is not unexpected given the low grafting densities and the broad polydispersity – all of which are expected to enhance particle penetration into brushes.[91] These studies show the potential to use HA brushes to sieve objects and molecules.

2.4.4 Reinforcement to stabilize brushes long-term

Some applications like lubrication or anti-fouling interfaces or fundamental polymer physics studies, will require a permanently stabilized brush. This is not possible with HA synthase binding alone, as the polymers release from the enzymes over a few days. Thus, stabilized brushes can be generated by crosslinking the HA to the underlying PEI surface chemistry with EDC-NHS chemistry. The EDC activates the carboxyl groups on HA for conjugation to secondary amine groups available from the PEI of the underlying grafting surface.

The surface-reinforced brushes are slightly reduced in height after processing but remain stable for up to a year with weak decay in thickness over long times. For reinforced HA brushes, SDS does not eliminate the brush. SDS, a detergent, disrupts the membrane fragments on the grafting surface and thus will result in a loss of HA grafting. The reinforced brush's invulnerability to SDS demonstrates the achievement of the covalent linkage of HA to the underlying surface (PEI) rather than the membrane fragments or the HA to itself.

CHAPTER 3. METHODOLOGIES

Select protocols are available in a Google Drive Protocols folder or available through Dr. Jennifer E. Curtis upon request:

https://drive.google.com/drive/folders/0B1RW_VxHNl4MVmthem1pX0dyRlU?usp=sharing

3.1 Preparing and reinforcing brush samples

The following methodologies outline how to prepare the brush samples and how to reinforce brushes for long-term use and storage.

3.1.1 Immobilizing bacterial membrane fragments on glass slides

Coverslips (VWR 48366 246 or VWR 48366 067) were sonicated in ultrapure water for 15 min and cleaned in reagent grade acetone in a sonicating water bath for 15 min. The coverslips were then rinsed with ultrapure water and dried with nitrogen and treated in a plasma cleaner (Harrick Plasma, PDC-32G, High RF power, air, 1 min). Poly(ethyleneimine) (PEI) (Sigma 482595, average Mw 1.3 kDa, 50% w/v in H_2O) was diluted with ultrapure water to 2.5% and the pH was adjusted to 7.0 using HCl. 200 µL PEI was dropped onto each coverslip (facing up) after plasma cleaning. The coverslips were incubated (allowed to sit at room temperature) for one hour before they were rinsed with ultrapure water and dried with nitrogen. Glutaraldehyde (Sigma G7651, average Mw 0.1 kDa, 50% w/v in H_2O) was diluted to 2.5% with PBS. 200 µL glutaraldehyde was sandwiched between a piece of parafilm and the coverslip, with the PEI coated side facing the solution. The coverslips were incubated for one hour before they were rinsed with ultrapure water and dried with nitrogen. The coverslips were then mounted on custom

Teflon rings using vacuum grease to seal. 30 µL of 0.2 mg/mL HA synthase-rich bacterial membrane fragments (diluted from 1 mg/mL in phosphate buffer) was pipetted into each teflon ring. The coverslips were incubated for 1 h. The solution in the sample holder was exchanged four times with Tris storage buffer (pH 7.3, 50 mM Tris (BDH 0312), 500 mM NaCl, 20 mM DTT, 5% glycerol). The samples were stored at -20 ºC.

3.1.2 Surface reinforcement

In order to form covalent bonds between the HA polymers and the grafting surface, carbodiimide conjugation was used to crosslink the carboxyl groups on HA to the primary amine groups ($-NH_2$) on the grafting surface. At the end of HA synthesis, solution was exchanged 3x with an EDC buffer (pH 7.0, 75 mM $NaKPO_4$, 50 mM NaCl). For this protocol, no DTT was added to the buffer because DTT reacts with EDC. Next, 100 mM EDC (1-Ethyl-3-(3-dimethylaminopropyl)carbodiimide, Sigma E1769) and 50 mM sulfo-NHS (sulfo-N-hydroxysuccinimide, Sigma-Aldrich 56485) was added to the sample. After 30 min, the solution was exchanged with newly dissolved EDC and sulfo-NHS (repeated twice). The sample was left overnight at room temperature. The next day, the solution was exchanged with a pH 8.0, 50 mM borate buffer (2 h) to quench the crosslinking reaction. Last, the reinforced brush was washed extensively with PBS.

3.1.3 Surface reinforcement optimization

To determine if the EDC/sulfo-NHS repeat exposures were necessary to achieve successful brush reinforcement, the number of "rounds" of EDC/sulfo-NHS refreshes was modified from 3 to 2 and 1. Additionally, no EDC Buffer was used to wash the sample. After brush synthesis, all the growth media was removed from the sample. 100 mM EDC

and 50 mM sulfo-NHS was dissolved in EDC buffer and added to the sample as usual. This was repeated for 1 or 2 rounds, as desired. The sample was left to sit overnight, washed with the target molarity, and the height measured the following day for initial heights and periodically afterwards for stability assessment.

3.1.4 Bacterial fragment removal with detergent

The detergent SDS (sodium dodecyl sulfate, Sigma-Aldrich L6026, 1 mg/mL) was used to disrupt the membrane fragments, including the embedded HA synthase in order to demonstrate that reinforced brushes are bound to the underlying surface; whereas in comparison non-reinforced brushes are destroyed along with the membranes.

3.2 Controlling brush synthesis

The following methodologies describe assorted techniques for initiating and halting brush growth, pausing and resuming synthesis, as well as regrowth of the brush after enzymatic removal.

3.2.1 Activating brush synthesis

The sample was removed from the -20ºC freezer and allowed to sit at room temperature for 40 mins to defrost. The storage buffer was exchanged with activation buffer (pH 7.3, 75 mM $NaKPO_4$, 50 mM NaCl, 20 mM $MgCl_2$, 0.1 mM EDTA). After warming the sample for 20 min in a 30˚C incubator, uridine 5-diphosphoglucuronic acid trisodium salt (UDP-GlcUA, Sigma-Aldrich U6751) and uridine 5-diphospho-N-acetylglucosamine sodium salt (UDP-GlcNAc, Sigma-Aldrich U4375) were added to a

final concentration of 5 mM each. The solution was pipette mixed and returned to the incubator for the desired growth time.

3.2.2 Quenching brush synthesis

To halt HA synthesis, the activation buffer was gently removed by pipetting. 100 µL of a quenching wash (300 mM NaCl, 20 mM EDTA) was added, pipette mixed once, and left to sit for one min. This solution was then removed from the sample and 100 uL of the quenching wash was added, mixed, and allowed to sit for one min. After one min, the quenching wash was removed and replaced with 100 uL of 150 mM NaCl, pipette mixed once, and removed. This was repeated once more. Finally, all of the NaCl solution was removed and the relevant imaging solution was added and pipette mixed gently three times.

3.2.3 On demand synthesis: pausing and restarting HA brush growth

The sample was washed three times with a mixture of the activation buffer (but with no UDP-sugars) and the quenching buffer in a ratio of 3:1, respectively. After replacing the volume with this mixture, the sample was allowed to sit, HA growth paused, for 30 min in the 30 ºC incubator. The sample was then washed with the activation buffer three times. After replacing the volume with the activation buffer, the UDP-sugars were added to a final concentration of 5 mM and growth was allowed to proceed again.

3.2.4 Regeneration

After exchanging the Tris storage media for activation buffer, the sample was incubated with 2% BSA (SeraCare 1900-0016) in PBS to a final concentration of 1% for 20 min in the 30 ºC incubator. If the sample is not “back-filled” with BSA, the brush will

never regrow as it seems that the surface retains hyaluronidase. HA synthesis was then activated and the sample was allowed to grow for the desired time. 0.5 units/uL bovine hyaluronidase dissolved in PBS was added to the sample to a final concentration of 0.025 units/μL and allowed to sit in the 30 ºC incubator for 30 min. The hyaluronidase was washed away by rinsing the sample with the activation buffer 20 times, ensuring to remove all the liquid with each wash. Excessive washing is necessary to ensure complete removal of hyaluronidase. HA synthesis was then reactivated and allowed to proceed for the desired time. Hyaluronidase addition and removal (followed by a growth period of 1 h) was repeated three times. The height was measured and averaged over five areas of the sample, each 211 x 211 μm^2.

3.3 Imaging

The following methodologies outline how the brush is visualized through confocal microscopy and how the height/thickness is measured.

3.3.1 Particle exclusion

Particle exclusion assays were performed using 0.7% w/v red, 200 nm latex FluoSpheres (carboxylate-modified Molecular Probes, Inc., F8810), 33 μg/mL fluorescent dextran (Molecular Probes, Inc. Alexa Fluor 647, 10 kDa), and 0.007% w/v of the green, 20 nm Fluospheres (Catalog number: F8787).[86, 92] Since 200nm beads and larger remain excluded from the brush region, image analysis of confocal images can be used to extract the location of the edge of the 200nm beads allows for estimate of brush height. The smaller 20nm beads penetrate the brush and stick to the underlying coverslip, providing a marker for the base of the brush. Images of the brush and beads were acquired

using a scanning laser confocal microscope (FV1000, Olympus, Tokyo, Japan; Objective: PlanApo N, ×60/1.42 NA oil). Imaging was completed within 1 h after halting HA synthesis in order to avoid significant desorption of the HA polymers.

3.3.2 Z-stack parameters

3.3.2.1 Growth curve and fluorescent profiles

To image, a z-stack was created by taking 100 nm vertical z-steps over a total distance of 20 µm.

3.3.2.2 General brush heights

To image, a z-stack was created by taking 500 nm vertical z-steps over a total distance of 20 µm.

3.3.2.3 Patterned squares

For height analysis of the squares in Figure 2, we measured the central portion of the 17.4 x 17.4 μm^2 squares (13.8 x 13.8 μm^2), eliminating data from the edges where polymer splay distorts the results of the patterning.

3.3.2.4 Patterned gradient

For height analysis of the gradient, the final brush height in each area was determined by eye (rather than the quantitative image analysis used for other experiments) due to the very small areas sampled.

3.3.3 Calculation of error for brush height

Generally, the error bars in plots represent the standard deviation of measurements, with the exception of the newest work presented in CHAPTER 5: Topography.

3.3.3.1 Measurements in CHAPTER 5

Error bars in plots report the propagation of the standard deviation of measurements with the systemic error in the axial resolution of the confocal microscope. Axial resolution on the confocal microscope was determined with the following equation:

$$Axial\ Resolution = \frac{1.4\ \lambda\ \eta}{NA^2}$$

λ = 543 nm was chosen because this laser is used to visualize the 200 nm particles that are excluded from the brush and used to determine the upper bound of the brush.

η = 1.518 for the oil used with the immersion lens.

NA = 1.42 for the objective used.

$$Axial\ Resolution = 572.3\ nm$$

Each sample's brush height was determined by measuring the brush height in n locations (n = 3-5). For N = 3 brushes, the average brush height was determined by averaging all the heights for each brush and their respective n-spots. For example, if n = 3 spots are measured per each of 3 samples, the average height is an average of all 9 heights measured and the standard deviation was determined from all 9 heights.

Final error in the brush height measured required an error propagation calculation of the standard deviation of the measurement and the axial resolution of the microscope.

$$Final\ Error\ in\ Brush\ Height = \sqrt{Stdev^2 + Axial\ resolution^2}$$

3.3.4 Calculation of confocal volume

The confocal volume is calculated according to the following:

$$V_C = \pi^{\frac{3}{2}} \kappa w^3$$

κ = the axial resolution divided by the resolution in XY.

w = beam radius or spot size.

$$w = \frac{1.22\ \lambda}{NA}$$

λ = 405 nm was chosen for the confocal volume calculation because this laser is used in patterning for the majority of the work in CHAPTER 5.

$$w = 348\ nm$$

XY resolution on the confocal microscope was determined with the following equation:

$$XY\ Resolution = \frac{0.61\ \lambda}{NA}$$

NA = 1.42 for the objective used.

$$XY\ Resolution = 174\ nm$$

The axial resolution for the 405 nm laser is calculated according to the previous section:

$$Axial\ Resolution = 426.9\ nm$$

$$\kappa = \frac{Axial\ Resolution}{XY\ Resolution} = 2.45$$

Therefore, the confocal volume is: $V_C = 5.7\ x\ 10^8\ nm^3$

3.3.5 Analysis of zstack intensity profiles to extract brush height

The intensity profiles of the green and red beads are plotted (Figure 10). The green profile corresponding to the smaller beads (20 nm) peaks at the surface of the sample. The red profile requires a linear fit of the intensity decay at high z positions above the object to correct for aberrations and absorption. The red profile is then corrected using this linear decay by normalization. The z-location of the 50% intensity value of the red profile is taken to be the average edge of the brush. Finally, the difference in the number of z-slices from the z-stack of the peak location of the green profile (the surface) and the 50% intensity value in the red profile (the average edge of the brush) is the thickness. Then, using the zstack step size parameter, one can convert the number of slices to a brush thickness value in microns.

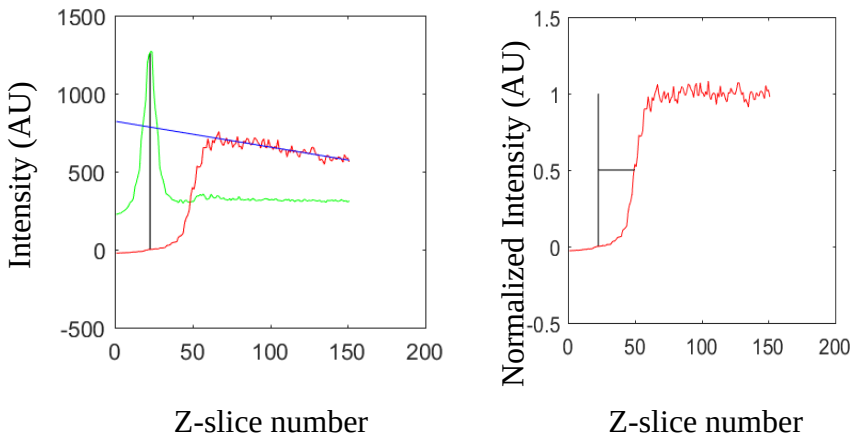

Figure 10. Left) Intensity profiles of green (20 nm) and red (200 nm) beads interacting with planar HA brush. The black vertical line denotes the surface and the blue line is the linear fit of the intensity decay in the red beads. Right) The normalized red bead intensity is plotted along with the same black vertical line denoting the surface. The difference in the number of slices in the z-stack between the black vertical line and the 50% intensity value in the red bead plot is used to determine the thickness of the brush.

3.4 Atomic Force Microscopy (AFM) scratch test

The following methodology describes a method of determining the grafting density of an HA brush.

Glass coverslips were prepared in the same method as described in the "Immobilizing bacterial membrane fragments on glass slides" methods section. Samples with PEI and glutaraldehyde components were dried with nitrogen. Samples containing bacterial membrane fragments but no brush grown yet were washed with ultrapure water and

allowed to dry overnight in a covered petri dish. Brushes were then grown on some of the samples in the same method as described in the "Activating HA synthesis" methods section. Post-HA synthesis, the brushes were gently washed (3x) with ultrapure water and baked at 50˚C overnight to dry. Brush thickness was then measured using probes with 80 kHz resonant frequency and 2.7 N m-1 spring constant on a Bruker Dimension Icon AFM in standard tapping mode at ambient conditions. Samples were scratched and then characterized at 30 nm scans with 30 nm pixel sizes. Height histograms were obtained using Nanoscope absolute depth analysis and the peaks were fit using the Fit Peaks (Pro) goal in OriginPro 8.5 software.

3.5 HA characterization

The following methodologies outline how to isolate HA from bacterial fragment components so that the HA MW can be determined. This section also describes three methods for determining the MW of the HA; solid-state nanopores, the Nanosight, and agarose gel electrophoresis.

3.5.1 HA purification

3.5.1.1 HA grown in solution

HA grown from bacterial membrane fragments in suspension was purified for later quantification by solid-state nanopore. After HA production, EDTA was added to a final concentration of 40 mM to quench the growth and the solution was put on ice for 10 min. The solution was then placed on a 90 ºC heat block for 10 min and subsequently put on again for 1-2 min to inactive the HA synthase [49]. To dissociate HA from the synthase,

the solution was mixed in a 3:1 ratio of Folch to HA solution and allowed to shake for 15 min. The Folch/HA solution was centrifuged for 7 min at 8,000 rpm and then the supernatant containing HA was removed and speed vacuumed until the solution volume was reduced to one-third.

3.5.1.2 HA grown in brushes

HA grown from bacterial membrane fragments in suspension was purified for later quantification by agarose gel electrophoresis and Nanosight. After HA production, the solution from each brush was gently removed and replaced with Quenching Wash (300 mM NaCl, 20 mM EDTA) and allowed to sit for 20 mins. SDS was added to a final concentration of 10 mg/mL, pipette mixed three times, and allowed to sit for 20 mins. The liquid from all samples was collected into one centrifuge tube. (Pipette tips were removed from the glass coverslips to allow all the liquid to be seen and removed.) EDTA was added (again for good measure) to a final concentration of 40 mM to quench the growth and the solution was put on ice for 10 min. The solution was then placed on a 90 ºC heat block for 10 min and subsequently put on again for 1-2 min to inactive the HA synthase [49]. To dissociate HA from the synthase, the solution was mixed in a 3:1 ratio of Folch to HA solution and allowed to shake for 15 min. The Folch/HA solution was centrifuged for 7 min at 8,000 rpm and then the supernatant containing HA was removed and speed vacuumed at 45ºC until the solution volume was reduced to one-half.

3.5.2 Solid-state nanopore determination of HA molecular weight distribution

Enzymatically-generated HA samples were mixed with measurement buffer (6 M LiCl, 10 mM Tris, 1 mM EDTA, pH 8.0) to a final concentration of 30 ng/µl and stored at

-20 ºC until measurement. Solid-state nanopore analysis was performed on 10 µl aliquots of the samples as described previously[93]. Briefly, a single pore (6-8 nm diameter) was fabricated[94] in a 19 nm thin, free standing silicon nitride membrane supported by a silicon chip (4 mm) and was placed in between one reservoir of clean measurement buffer and one reservoir of sample mixture. Ag/AgCl electrodes (Sigma Aldrich, St. Louis MO) were placed in each reservoir and an Axopatch 200b patch clamp amplifier (Axon Instruments, Union City, CA) was used to both apply a voltage of 200 mV and record trans-pore ionic current and resistive pulses caused by HA translocation through the pore. Data was collected at a rate of 200 kHz with a four-pole Bessel filter and an additional 5 kHz low-pass filter was applied using custom software. Resistive pulses ('events') in the current signal were identified as transient interruptions in the ionic current >5σ in amplitude from the baseline and with a time duration range of 25 µs-2.5s. The Event Charge Deficit (ECD[95]) (defined as the integrated area of the event) was determined for each translocation event and converted to molecular weight using a calibration standard produced with synthetic, quasi-monodisperse HA [93]. A MW distribution histogram was generated for each sample with these values and used for subsequent analyses.

3.5.3 Nanosight

1 mg of 2500 kDa Select-HA (Hyalose, HYA-2500K-1)was hydrated in 100 µL of LC-MS grade water (ThermoFisher, 51140) (to a final concentration of 10^{18} particles per mL), vortexed, and allowed to sit, refrigerated, for 1 week. When establishing protocols, 25 mg polydisperse Rooster Comb HA (Sigma, H5388-100MG) was dissolved in 5 mL to a final concentration of 10^{15} particles per mL, assuming 1 MDa MW. Using a positive displacement pipette, the Select-HA was serially diluted to reach the ideal range (for

Nanosight measurement) of 10^7-10^9 particles per mL. Each dilution was allowed to slowly mix for 2 hrs or overnight. LC-MS grade water was flowed through the Nanosight (NS300 Model) first to flush the lines and take a quick measurement and verify cleanliness of the water (seeing 10^6-10^7 particles per mL). Then, the HA was measurement with the standard measurement settings (5 measurements, 2 mins loading, 60 seconds equilibrating (to allow flow to cease), room temperature. If flow was applied during the course of the measurement, the flow rate was set to 100.

3.5.4 Agarose gel electrophoresis

A 0.5% agarose gel was made by dissolving 0.25 g agarose powder (Invitrogen, 16500-100) in 50 mL of 1x TAE buffer (diluted with ultrapure water from 10X TAE solution (Invitrogen, 15558-042). To dissolve, the powder/TAE solution was microwaved for ~25 seconds, mixed gently, and microwaved again for ~12 seconds (or until the solution started to bubble). The solution was mixed again and visually checked for any undissolved agarose powder. The agarose was poured into the gel holder/machine (ThermoFisher, Owl Easycast B1A) that had either the 6 well or 10 well comb. The gel was allowed to cool for 35-40 mins while covered (to reduce evaporation). After the gel was setup, it was arranged such that the wells were on the black anode end of the electrophoresis machine and 1x TAE buffer was poured over the gel and into the electrophoresis machine until it was full and completely covering the gel. The samples were prepared as follows. If using a wide 6 well gel, 12 uL of the sample + 2.4 uL of the loading dye (BioLabs, #B7021S) were carefully micropipetted into the well. If use a skinnier 10 well gel, 5 uL of the sample + 2.4 uL of the loading dye were carefully micropipetted into the well. Select-HA ladders were used as a standard. (Fisher Scientific, Select-HA MegaLadder NC1775814, Select-HA

HiLadder NC1744600, Select-HA LoLadder NC1774599.) The samples were run through the gel for 3.5 hrs at 34 V. Once complete, the gel was placed in a 0.005% StainsAll (Sigma Aldrich, E9379-1G) solution in 50% ethanol overnight. The next day, the gel was moved to a 10% ethanol solution and allowed to sit for 6 hrs. Finally, the wet gel was placed on a light pad and photographed.

3.6 Patterning

The following methodologies describe how the HA brush is patterned, as well as the protocols that were used to determine the underlying patterning mechanism of ROS.

3.6.1 Optimizing patterning settings

A resolution of 512 x 512 pixels was always used. For each wavelength, the number of times the desired region was scanned (aka, the necessary exposure time) by the confocal microscope was varied. The minimum number of scan times necessary for brush elimination was determined using each laser set to 100% intensity. For λ = 405 nm, $P_{max,405}$= 561 μW, the number of scans necessary was 5. For λ = 488 nm, $P_{max,488}$= 458 μW, the number of scans necessary was 9. For λ = 635 nm, $P_{max,635}$= 548 μW, the number of scans necessary was 60. For λ = 405 nm, the pinhole size is automatically determined by the software to be 85 μm. The axial resolution for λ = 405 nm is calculated according to the Supporting Information to be 426.9 nm. Once the number of scans was determined, this value would be set for all future experiments with that wavelength and only the intensity of the laser would be varied between 0-100%. To determine how the number of scans and laser intensity translated to an applied energy density, measurement of the laser power at the objective was measured using a Coherent PowerMax-USB sensor (type 5499G16R) or

a ThorLabs S170C Microscope Slide Power Sensor. This measurement was taken once every 6 months. In between measurements, the maximum energy density necessary to eliminate the brush appeared to drift over time, so the power rating of each laser according to the microscope software was used to calibrate for this drift which likely arose from slow deterioration of alignment. A description of the energy density calculation based on patterning parameters is provided in the Supporting Information.

3.6.2 Prepatterning (binary/variable/gradient)

After exchanging the Tris storage media for growth buffer and the sample was placed in a stage-top incubator at 30°C with wet sponges to maintain humidity. A low concentration of 8 μm silica microspheres (Cospheric, SiO2MS-1.8 7.75um) were added and brought into focus with bright field microscopy. The focus was adjusted by an amount equal to the radius below the center such that the focus should now be on the surface of the sample – at the plane of the membrane fragments. (Figure S1 shows that slight error in this focusing method of a few microns does not result in significantly different resulting brush heights.) The area of interest was chosen by setting the zoom factor (for square areas) or by setting the zoom factor for the area width and extending one side length to create a rectangle (such as for creating the gradient, where the area of the rectangle always matched that of the square area used for calibration). A resolution of 512 x 512 pixels was always used. The microscope's 405 nm laser raster (line) scanned the area using optimized settings. To apply the laser to a new area, we refocused on the fragment surface using the microspheres, then proceeded with the same steps as before. After all desired areas were laser treated, we activated HA synthesis and the sample grew for the desired time.

3.6.3 Postpatterning (unreinforced and reinforced brushes)

For unreinforced brushes, after HA synthesis has been halted, the solution on the sample is removed and replaced with the imaging solution. For reinforced brushes, after reinforcement, the sample is washed with 150 mM NaCl four times. This solution is then replaced with the imaging solution. The green, 20nm nanoparticles stick to the PEI-GA layer on the glass interface which makes focusing on the fragment layer straightforward and avoids the use of the 8 μm silica microspheres. Once the focal plane is set, patterning can proceed as previously described: setting the size of the area of interest with the zoom settings, defining the laser intensity or number of scans to set the energy density applied to the surface, allowing the laser to scan the area, refocusing for each new area, repeating until all desired areas have been treated. Imaging can then proceed as normal since all the appropriate nanoparticles are already present on the sample.

3.6.4 Comparing high and low DTT concentration effects on patterning

The growth buffer was used for low DTT concentration experiments (pH 7.3, 75mM NaKPO4, 50mM NaCl, 20mM $MgCl_2$, 0.1mM EDTA, 5mM DTT). For high DTT concentration experiments, the molarity was increased 10x to 50mM DTT while all other components remained unchanged. Patterning of each brush time proceeded according to their previously described protocols where the brush was first patterned in the presence of the low DTT growth buffer. Then, after patterning was completed, the solution was exchanged three times for the high DTT growth buffer. Then, patterning was repeated, and the results compared.

3.6.5 Impact of laser focus height above the surface during patterning

We investigated the impact of the uncertainty of the laser focus on the patterning outcome since the center of the 8 µm silica microspheres is determined by eye. We patterned different regions using several different focal planes above the presumed glass interface. To achieve this, the microspheres were brought into focus (at their expected center and widest point). The focus was adjusted by remotely moving the stage position varying amounts (0, 1, 2, 3, and 4 µm) in different patterned regions below the bead center such that the focus will be different heights above the glass interface. The same patterning settings were used in each scenario and the resulting brush heights of each area was extracted. No significant dependence on the position of the focal plane was found (Figure 11).

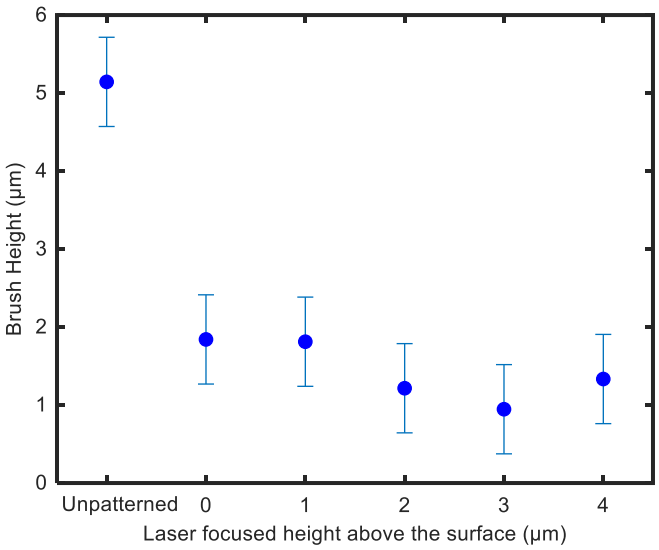

Figure 11. Height of patterned regions *versus* the height above the glass interface where the laser was focused during patterning. Height on unpatterned region included for reference. N = 1 brush.

3.6.6 Calculation of energy density

$$Energy\ Density = \frac{(Power\ Output\ at\ Objective) * (Fraction\ of\ laser\ intensity) * (Total\ scan\ time\ per\ pixel)}{Area\ per\ pixel}$$

Power Output at Objective was determine as described in Section 3.6.1. Fraction of laser intensity is a decimal value between 0 and 1 representing the % intensity of the laser light. Total scan time per pixel is determined by the software settings of the confocal microscope and the number of scans chosen. The slowest raster scan setting in the software is 200 µs/pixel. Multiplying this value by the number of scans gives the total scan time per pixel. Area per pixel is determined by the zoom setting (which adjusts the size of the field of view) and the resolution setting.

3.7 Scratch testing for splay

The following methodology describes an experiment that was used to determine if polymer splay or brush curvature along the edges of patterned regions was a purely mechanical effect.

A brush was grown for the desired amount of time and synthesis is quenched. All the liquid was removed from the sample. The pipette tip was removed from the glass coverslip. Using a lab marker, a straight line is drawn across the coverslip that would intersect with the center of the sample, but not actually drawn inside the grease ring. This line shows where the scratch was and served as a landmark when imaging. Holding a clean razor blade (VWR, 55411-050) at an angle such that the blade will only touch the glass with the very

corner, the razor is dragged along the line sketched with the lab marker in one swift motion with pressure (but not too much to crack the glass). The pipette tip was replaced, and fresh grease added, if necessary. The imaging solution was added and then the sample was imaged.

3.8 Stimulus response

The following methodologies outline protocols used to determine how the HA brush responds to changes in salt concentration (ionic strength) and solvent quality.

3.8.1 Stimulus response to ionic strength

The (unreinforced or reinforced) sample was first imaged to establish a baseline height for the brush (using a particle exclusion assay) in the standard ~130 mM imaging buffer (75 mM $NaKPO_4$, 50 mM NaCl, 10 mM $MgCl_2$, 0.1 mM EDTA, 2.2% glycerol, 5 mM DTT). The media was then gently exchanged two times with a 300 mM NaNO3 solution. Then, the solution was gently exchanged two times for the target ionic strength. To image again, the nanoparticles outlined in the brush height measurement section were added to the sample, but with a concentration of $NaNO_3$ to match the target ionic strength. If the sample was unreinforced, the sample was discarded after one target ionic strength measurement. If the sample was reinforced, after each target ionic strength measurement, the solution was gently exchanged with a 300 mM $NaNO_3$ solution two times and then exchanged with the new ionic strength two times. Then, the sample could be imaged at the new ionic strength with particle exclusion.

3.8.2 Slope calculation for salted brush regime

Using the LINEST function in Microsoft Excel (2013), the slope and its standard error were calculated. The LINEST function uses the “least squares” method to find the slope of a straight line that fits the data.

3.8.3 Stimulus response to poor solvent [All at once]

A reinforced brush sample was first imaged in ultrapure water with particle exclusion assay. The media was then gently exchanged four times for pure ethanol. The sample was closed to the outside environment to stop ethanol evaporation by applying a parafilm cover that is attached to the pipette tip with vacuum grease. Then, the sample was imaged with particle exclusion.

3.8.4 Stimulus response to poor solvent [Incrementally]

A reinforced brush sample was first imaged in ultrapure water with particle exclusion assay. The media was then gently exchanged four times with a solution of the target ethanol concentration and the sample was covered by applying a parafilm cover that is attached to the pipette tip with vacuum grease. To image, the nanoparticles outlined in the Particle Exclusion Assays section were added to the sample, but in a solution of ethanol to match the target concentration. After each concentration was imaged, the solution was removed and the sample was washed four times with the next target concentration. This continued until all target ethanol concentration measurements were completed.

3.9 Labeling

The following methodologies outline fluorescent labeling methods that can be used to extract a polymer concentration profile of the HA brushes.

3.9.1 Alexa-hydrazide labeling post-growth

In order to form covalent bonds between the HA polymers and a hydrazide-Alexa Fluor dye, carbodiimide conjugation was again used to crosslink the carboxyl groups on HA to the amine group on the hydrazide-dye. After brush growth is complete, the sample is washed 3x with a low pH version of the EDC buffer (pH 4.75, 75 mM $NaKPO_4$, 50 mM NaCl). Next, and importantly, EDC (1-Ethyl-3-(3-dimethylaminopropyl)carbodiimide, Sigma E1769) and sulfo-NHS (sulfo-N-hydroxysuccinimide, Sigma-Aldrich 56485) were quickly dissolved in the low pH EDC buffer to a final concentration of 100 mM and 50 mM, respectively. If the pH 7.0 EDC buffer is used, labeling will not occur. The 2 mg/mL stock hydrazide-dye was diluted to 1 mg/mL with the EDC/sulfo-NHS solution and then added directly to the sample. After 1hr, the sample was washed 6x with 150 mM NaCl (or the target molarity for imaging). The profile of the labeled brushes was extracted by imaging in only their target molarity solution, 100 nm steps, 20-30 µm zstacks (depending on growth time and molarity of imaging solution). The height of the labeled brushes was extracted by imaging in the target molarity in the presence of 0.7% w/v green, 200 nm latex FluoSpheres (carboxylate-modified Molecular Probes, Inc., F8848).

3.9.2 Azide-modified HA brush

For normal brush growth, a 1:1 ratio of GlcNAc:GlcUA is added with a 5 mM concentration of each. To incorporate azide-modified N-acetylglucosamine (N-azidoacetylglucosamine tetraacylated, aka GlcNAz) sugars into the HA brush, a ratio of 1:9:10 GlcNAz:GlcNAc:GlcUA was used instead[44]. This sugar mixture was added instead of the normal sugars after sample warmth, per *Activating brush synthesis*. After

growth, if brush reinforcement is desired, the *Surface reinforcement optimization* protocol was followed and only one round of EDC/sulfo-NHS was used. The EDC/sulfo-NHS was allowed to sit overnight at room temperature on the lab bench and washed out 3x with water the following day. All the liquid was removed from the sample. To label the brush (unreinforced or reinforced): 100 mM of AFdye 546 DBCO (Click Chemistry Tools, 1286-1) was diluted to 10 mM in ultrapure water, added to the sample, and allowed to sit at room temperature for 6 hrs (up to overnight) while covered in aluminium foil. After 6 hrs, the sample was washed 6x with the target imaging molarity. The profile of the labeled brushes was extracted by imaging in only their target molarity solution, 100 nm steps, 20-30 µm zstacks (depending on growth time and molarity of imaging solution). The height of the labeled brushes was extracted by imaging in the target molarity in the presence of 0.7% w/v green, 200 nm latex FluoSpheres (carboxylate-modified Molecular Probes, Inc., F8848).

CHAPTER 4. THE HYALURONAN BRUSH

Parts of the following chapter have been previously published:

Wei, W., Faubel, J.L., Selvakumar, H. et al. **Self-regenerating giant hyaluronan polymer brushes**. *Nat Commun* **10**, 5527 (2019). DOI: 10.1038/s41467-019-13440-7

The HA brush, generated by the enzyme HA synthase and comprised of incredibly long polymers, is a novel biomaterial that opens doors for studies in fundamental polymer physics, biophysics, materials science, and biomolecular engineering. Its ultra-thick quality allowing for easy visualization through confocal microscopy increases the ease with which these studies can be conducted. The following chapter outlines key characteristics of the HA brush system such as its grafting density, pause-ability, regenerative qualities, methods for extracting the MW of the HA, and methods for obtaining the monomer concentration profile. This foundational knowledge of the brush system will be valuable in all future studies.

4.1 Grafting density determination

To estimate the grafting density of the HA polymer brushes, we measured the density of HA synthase in the membrane fragments. Typical bacterial membranes have a density of 30,000 proteins per μm^2.[96] Protein gel electrophoresis analysis of the HA synthase-enriched membrane fragments previously indicated that 6.8% of membrane proteins by weight are HA synthase. This yields an estimate for HA synthase density of 2040 molecules per μm^2 (0.002 chains per nm^2) corresponding to a ~22 nm spacing in the membrane fragments. Further, the membrane fragments cover an estimated 30% of the

surface with an average spacing of a few hundred nanometers as previously determined by SEM.

Measurements of the grafting density extracted from the height of the dried HA brush (4 h) compare well with the above estimate. The dry brush height was measured to be 12.5 ± 0.7 nm (n = 3, ± is st. dev.) using atomic force microscopy (AFM, Figure 12). The grafting density can be found using the relationship:

$$H = \frac{N\,\sigma\,b^3}{\tau} \tag{5}$$

where H is the dry brush thickness, N is the number of monomers, b is the monomer length (1 nm for HA), σ is the grafting density, and τ is the second virial coefficient indicating the solvent quality (τ = 1 for poor solvent).[97]

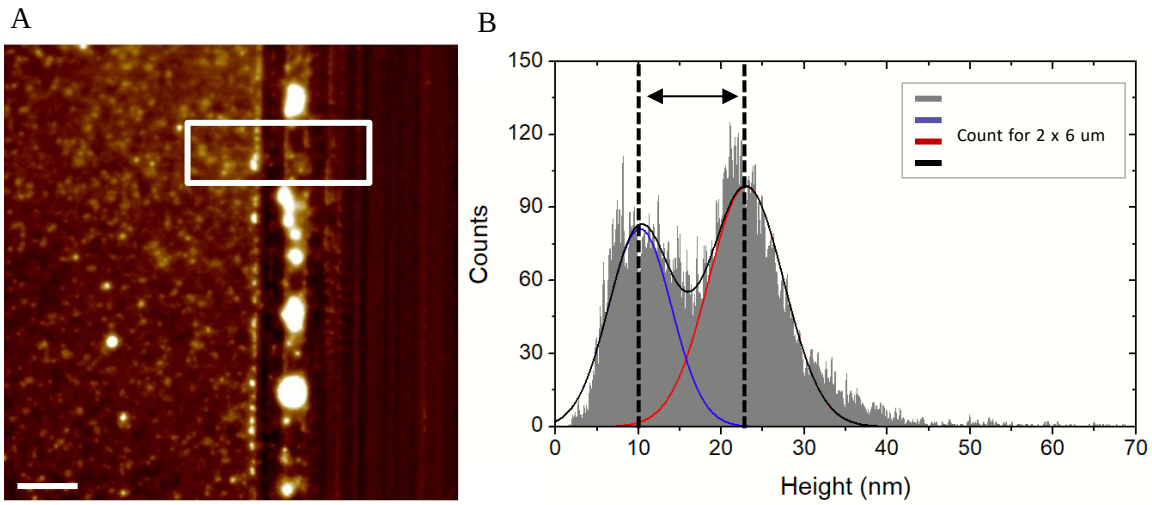

Figure 12. Representative AFM result of the brush scratch test. A) Topography image with histogram analysis area outlined in white. Scale bar 2 µm. The measurement was repeated on three surfaces in order to acquire an average dry brush height of H_{dry} = 12.5 ± 0.7 nm (st. dev.). B) Corresponding height histogram. Z scale = 70 nm.

To estimate the monomer number, N, for a polydisperse system at t_{growth} = 4 h, we can use the number-averaged molecular weight M_n, 2.42 MDa as measured by the solid-state nanopore sensor technology, which yields N = 6050; or we can use the weight-averaged molecular weight M_w, 6.76 MDa, which yields N = 16,900. Hence, examining a range of 6050 < N < 16,900 and H = 12.5 nm, we arrive at a grafting density range of 0.00074 ± 0.0021 chains per nm^2, or equivalently, 740-2100 chains per μm^2. Notably, these values are two orders of magnitude smaller than those for a typical synthetic brush generated via controlled radical polymerization (typically ~0.1 to 1 chain per nm^2). However, the density is still effectively high for this system, considering the micrometer lengths of the grafted polymers. Since we expect that about 50% of the fragments are upside down and only 30% of the surface is covered by HAS fragments, an approximate grafting density of 740 chains per μm^2 as compared to a maximum 2100 HAS density in the fragments (predicted from protein analysis) seems reasonable, as it is 35% of the estimated enzyme density.

4.2 Validation of brush regime

HA synthase generated HA films thicker than H ~ 300 nm should lie well within the brush regime, which is defined by the requirement that the average distance between grafting points is less than the diameter of the polymer in solution. The hydrodynamic radius for HA is $R_H \sim M_W^{\nu}$, where $0.6 < \nu < 0.8$ for high MW HA [98]. Using $\nu \sim 0.7$, we find that at 1 hr, $R_H \sim 324$ nm. Since the brush height increases linearly in early times, at 10 min the brush height should be approximately ~333 nm. Correspondingly, the HA M_W increases linearly at early times as well [82], yielding 0.72 MDa or $R_H \sim 100$ nm. The grafting density is 740 chains per μm^2 or 1 chain every 37 nm, much less than a chain

diameter of 200 nm. Hence at 10 min, with a 300 nm brush, the typical chain will have a diameter five times the average distance between chains, putting the system well into the brush regime.

4.3 Regeneration

The HA synthase maintains the ability to generate multiple polymers sequentially after natural release or external degradation of the HA [82]. Hence, the HA synthase interfaces should be able to regenerate or continuously replenish a HA reservoir as needed. To demonstrate this, we grew the brush for one hour on planar interfaces, removed it by enzymatic degradation (hyaluronidase) and then regrew it three times - each time, after enzymatic removal (Figure 13). Little deviation in final brush height from the initial height is detectable with each subsequent regeneration. The small decay in brush height after each regeneration step may be due to the hyaluronidase sticking to the surface. We found that we had to minimize hyaluronidase adsorption to the surface using bovine serum albumin (BSA), or no brush would grow. It is possible that small amounts of hyaluronidase still bind to the surface, increasing with each exposure. These experiments demonstrate the potential for HA synthase brushes to be employed as regenerative interfaces.

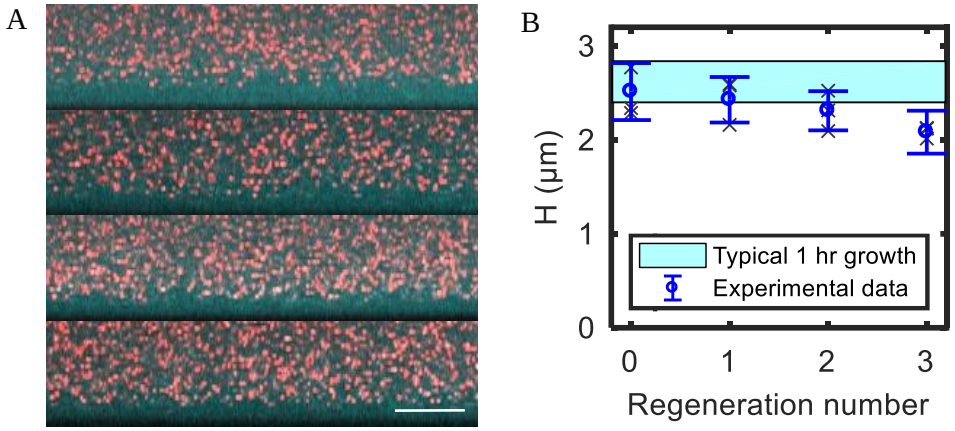

Figure 13. A) Regeneration of HA brush after enzymatic degradation with hyaluronidase. Top image shows brush after one hour of growth before digestion. The next three images show the regenerated brush following digestion and one hour regrowth 1, 2, and 3 times. Scale bar is 5 μm. B) Brush height versus the number of regeneration times (N=3 brushes, where grey x's correspond to average of five measurements of each brush and blue is the mean and st dev).

4.4 Pausing brush growth

The system also has capability for on demand synthesis. Figure 14 shows how the HA polymerization and brush growth can be halted at a desirable height and then later, reinitiated by controlling the availability of Mg^{2+} ions and sugar substrates. In this experiment, the brush growth was halted after 2 h, paused for 30 min and then reinitiated for 2 h. Despite the pause, the final brush height was in the expected range of brush heights after 4 h uninterrupted growth.

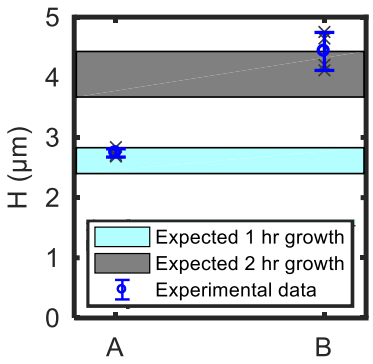

Figure 14. Interrupted growth (A) followed by an additional growth period of 1 h (B). (Grey x's correspond to five measurements from one sample.)

4.5 Brush deterioration from handling (pipetting)

We tested the impact on brush height of exchanging solvents. Since the HA is not permanently bound to the HA synthase, some HA loss is expected. Every 20 min for 1 h, while the sample sat on the confocal microscope stage at 30°C, six gentle pipette pumps were administered to the sample (18 total). The effect was to mimic conditions of exchanging solvents. Over the course of one hour and 18 gentle pipette pump actions, the average height of the planar brushes was relatively stable (Figure 15A), showing a slight decrease in average values. This induced height decrease is more significant than for a brush measured every 20 min with no solvent swaps (Figure 15B). Hence shear induced desorption driven by pipetting increases brush decay relative to the decay from natural desorption.

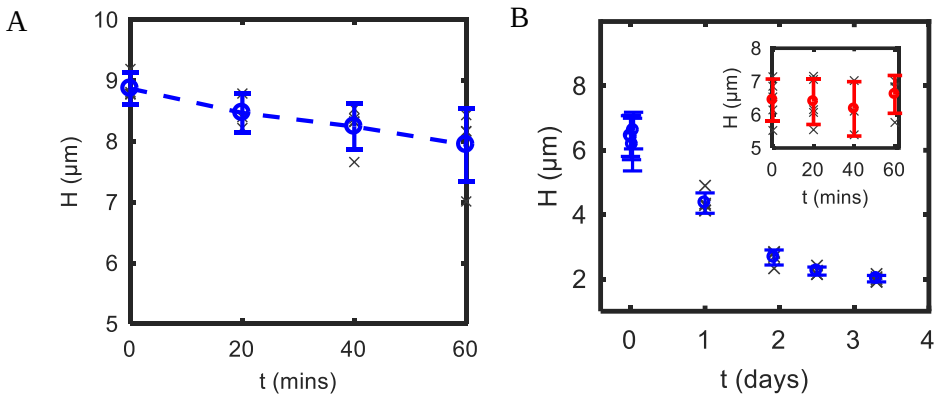

Figure 15. A.) Each blue circle represents the average brush height after 6 gentle pipetting pumps (t_{growth} = 5.5 h) for one brush. Error bars report st. dev. The grey x's are the height measurements on the same brush from at least four unique areas on the same sample. B) Brush stability versus time (unreinforced, natural brush). For both A and B, N = 1 brush, grey x's correspond to measurements on same brush, blue reports the mean and st. dev.

4.6 XPS

We examined the HA brush interface with X-ray photoelectron spectroscopy (XPS) to provide additional evidence that the growing polymer is HA. Importantly, the interface from which the HA brushes grow is complex. It is comprised of glass, poly(ethyleneimine) (PEI), glutaraldehyde (GA), and bacterial membrane fragments, which are rich in membrane proteins. After growth, the HA brush is attached to the surface by HA synthase located in the membrane fragments.

We first investigated surfaces with and without HA to understand the spectral contributions of each component. HA films drop-cast directly on glass exhibit three C(1s) photoelectron peaks near 287.7, 286.0, and 284.3 eV [2, 3], corresponding to O-C-O/O=C-O, C-O, and C-C-/C-H bonds, respectively. A typical C(1s) spectrum acquired in our lab for HA prepared in this manner is shown in Figure 16a. Peak values from three HA samples

matched those reported in literature, with 287.8, 286.1, and 284.3 eV. The intermediate binding energy peak (C-O) is the most intense at 286 eV.

The glass/PEI/GA/fragment surface from which our HA brush is synthesized, because it is rich in the same chemical bonds as HA, exhibits C(1s) photoelectron peaks with similar binding energies (287.4 eV, 285.8 eV, 284.2 eV) but distinct relative intensities. A typical C(1s) spectrum of a glass/PEI/GA/fragment (i.e., HA-free) surface is shown in Figure 16b. The value of the two highest binding energy peaks (O-C-O/O=C-O and C-O) is small relative to those for HA drop-cast directly on glass. However, the lowest binding energy peak (C-C/C-H) is substantially larger.

A sufficiently thick HA brush on top of the complex glass/PEI/GA/fragment interface would ideally screen the underlying chemistry and produce a spectrum identical to an HA film drop-cast on glass (Figure 16a). However, as can be seen in Figure 16d, e, we did not find that this is the case for our HA brushes nor HA dropcast onto the PGF interfaces (Figure 16c). The underlying glass/PEI/GA/fragment surfaces influence the spectrum.

Table 1. Change in Area of C-O Peak (286 eV) with HA Addition. Change in area under Peak 2 corresponding to C-O (~286 eV) when HA is added to glass/PEI/GA/fragment surfaces either by dropcasting or HA brush growth. The change in area increases with increasing amounts of HA. The PGF average area was obtained from N=4 samples.

	Change in Area	SD	N
HA Dropcast	+39,318	1038	3
4 h Brush	+14,421	3857	2
4 h Brush, Reinforced	+11,778	5036	2

To confirm that the polymer brush is HA, we investigated a series of surfaces exposed to HA. Figure 16c displays the C(1s) spectrum after drop-casting HA onto the glass/PEI/GA/fragment surface. As expected, the intensity of the two highest binding energy peaks increases with the addition of HA. However, unlike the case of HA drop-cast on glass (Figure 16a), the lowest binding energy peak from the underlying PEI/GA/fragment surface (arising from C-C/C-H) still dominates the spectrum. We next examined spectra from HA brushes with different known amounts of HA deposited on glass/PEI/GA/fragment surfaces: a 4 h unreinforced brush (Figure 16d) and a 4 h reinforced brush (Figure 16e). Both samples have XPS spectra similar to that of the glass/PEI/GA/fragment/HA dropcast surface (Figure 16c) as opposed to the glass/PEI/GA/fragment surface with no HA (Figure 16b). As seen in Table 1, the area of the intermediate binding energy peak (C-O) increases the most for the HA drop-cast

directly onto glass. The peak area for C-O also increases for the 4 h brushes, both unreinforced and reinforced. As expected, area increase is less for 4 h brush, than for the drop cast HA. Further, as we might predict, the area increase for the unreinforced brush is larger than for the reinforced 4 h brush. This is consistent with our reports that reinforcement stabilizes the brush but at the cost of some HA loss.

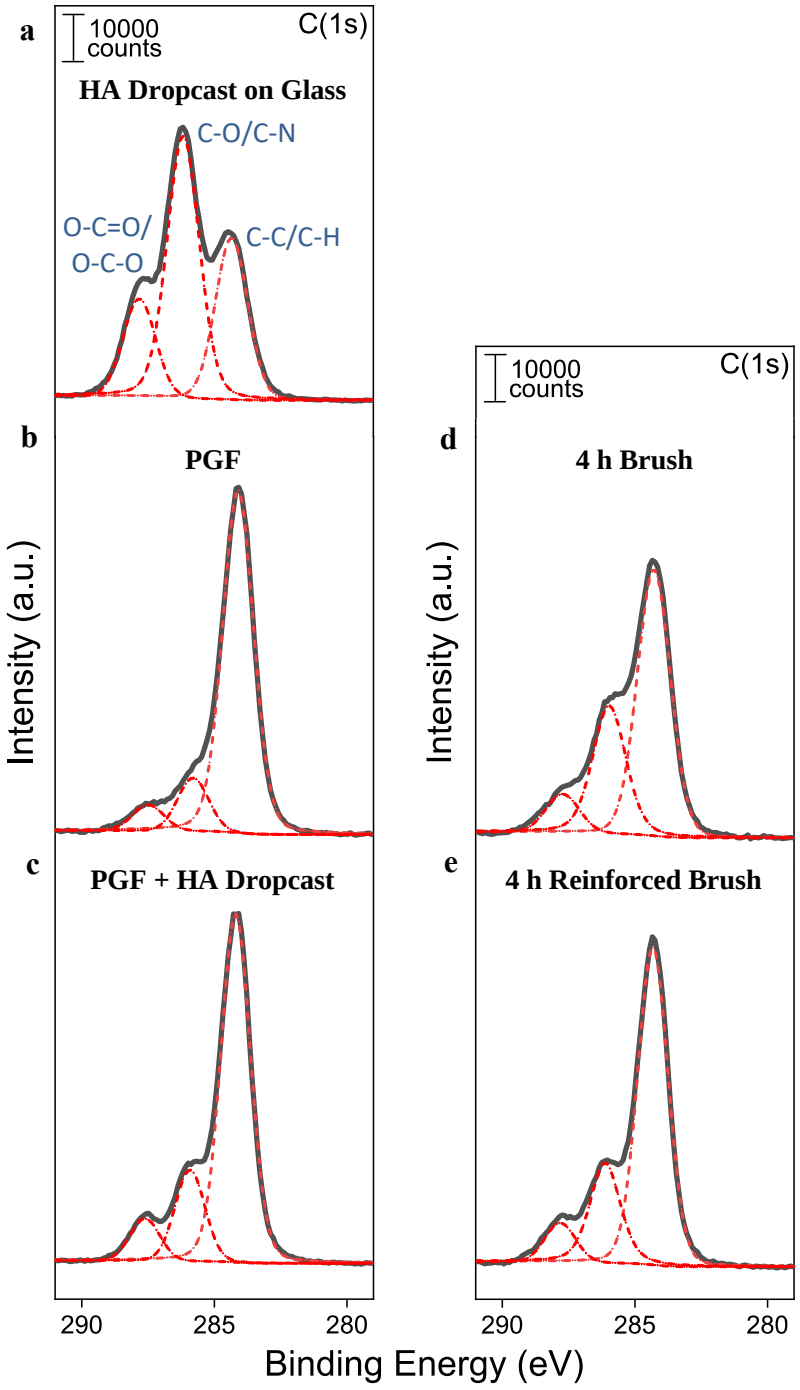

Figure 16. Curve fitted C1s XPS spectra obtained for a, HA dropcast on glass, b, PGF (PEI, GA, membrane fragments only), c, HA dropcast on PGF, d, 4 h brush, and e, 4 h reinforced brush.

In summary, XPS data of the HA synthase fragment surfaces with and without HA support the claim that the polymer brushes are comprised of HA. Although the spectrum is not a traditional HA spectrum, due to the underlying complex surface of PEI/GA/fragments, the evolution of the spectrum with addition of HA – specifically the increasing area of peak 2 with increasing HA deposition – confirms a polymer with C-O bonds (e.g. HA) is being deposited on the surface.

4.7 Molecular weight distribution of hyaluronan grown in solution

We used solid-state nanopore sensor technology [93] to characterize the output of the HA enzyme by the membrane fragments over time. This data is complementary to our already published data from SEC-MALLS, but is more accurate because of the sensor's ability to measure high molecular weight polymers and the full molecular weight distribution. A snapshot of the HA molecular weight distributions at 1, 2, and 8 h of synthesis is shown in Figure 17. The resulting HA is polydisperse, spanning two orders of magnitude. At 8 hours, the distribution has an average contour length of ~12.8 μm, corresponding to 5.13 MDa (M_w). Notably, much longer chains were detected (up to 50 MDa). The average M_w and M_n versus growth time are summarized in Table 2.

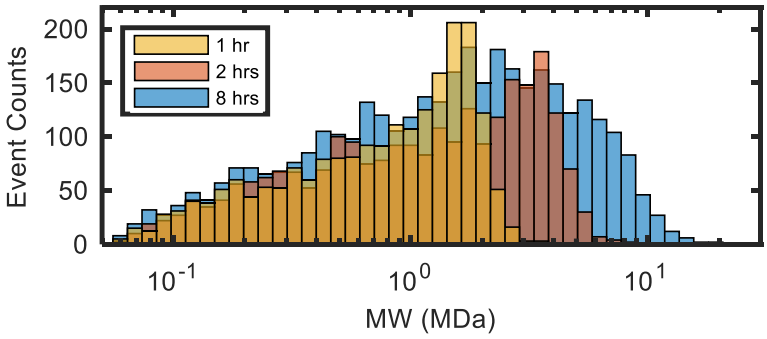

Figure 17. HA molecular weight distributions assayed by solid state nanopore (N=2091, 1 h; N=2500, 2 h; N=3699, 8 h).

Table 2. Analysis of the average molecular weight distribution of the HA produced by HA synthase rich membrane fragments. Data was collected using the single molecule nanopore assay at four time points: 1 h, 2 h, 4 h, 8 h. The number and weight averaged molecular weight peaks at 4 hours, with maximal polydispersity (PDI, polydispersity index) at that time point as well. The average length corresponding to the Mw is calculated using 1 nm = 400 Da for the HA polymer. The # of chains is the total number of HA molecules measured for the given brush growth time. The reported standard deviation (st. dev.) captures the width of the distribution. $RH \sim MW^{0.7}$.

t_{growth}	M_n (kDa)	M_w (kDa)	St Dev (kDa)	PDI (M_w/M_n)	Length (μm)	R_H (nm)	# chains
1 h	971	1430	665	1.5	3.6	162	2091
2 h	1690	3020	1500	1.8	7.5	273	2500
4 h	2420	6760	3240	2.8	16.9	450	4823
8 h	2410	5130	2560	2.1	12.8	395	3699

4.8 Molecular weight distribution of hyaluronan grown in a brush configuration

It is incredibly useful to know the molecular weight distribution of HA as generated by the membrane fragments (Figure 17), but it is unlikely that there would be a matching distribution generated from a brush configuration. This is because the fragments in solution have a maximal accessibility to the UDP-sugars and are less crowded. When immobilized on a planar surface, despite using significantly more UDP-sugars than minimally necessary (5mM each vs 1mM each [80, 99]), there will still be crowding between adjacent polymers which could create a physical feedback loop with the hyaluronan synthase and slow synthesis.

We are interested in determining the molecular weight distribution of the HA brush configuration because the precise nature of the polymer size influences the way the polymers themselves are distributed throughout the brush. There is a distinct lack of experimental work with polydisperse brushes and being able to characterize the HA brush MW distribution would be a significant addition to the field – to validate current theory and provide real distributions for simulation. Extracting and characterizing the HA from the brush surface is a non-negligible obstacle that the following sections aims to surmount.

4.8.1 Comparison of HA measurement techniques

Working with our solid-state nanopore collaborators was straightforward, but for the measurement needs we anticipate having as this work progresses, we soon saw the need for an alternative method for extracting HA molecular weights from our polydisperse system. There are many methods of determining polymer molecular weight, each with their advantages and disadvantages, particularly when measuring high molecular weight polymers like HA. A survey of these methods is summarized in Table 3. [100-112]

Table 3. Summary of major advantages and disadvantages for a variety of molecular weight measurement techniques.

Method	Advantages	Disadvantages	MW/Sizes and Concentrations
Dynamic Light Scattering	Ensemble measurement Preserves sample	Scattering puts emphasis towards larger MW particles Best with monodisperse samples	~0.01 mg/mL – 5% mass *Depends on size, density, and scattering angle
Agarose Gel Electrophoresis	Semi-quantitative detection of HA Sample can be recovered and used in another technique	Large volumes required Requires standards/ladders	~10 kDa – 10 MDa *Depends on agarose gel concentration
ELISA (Enzyme-linked immunosorbent assay)	Quantitative detection of HA	Poor MW differentiation Can miss low MW	Min: ~20 kDa Min: ~0.027-0.200 ng/mL Max: ~40 ng/mL
SEC (Size exclusion chromatography)	Discrete detection of HA sizes	High cost Long run times	~100 Da – 1 MDa
MALLS (Multi-angle laser light scattering)	Qualitative detection of HA	Can miss low MW Limited precision Must be paired with SEC for MW determination	Rg: ~10 nm – 100's nm
Mass Spectrometry	Quantitative detection of HA	High cost	Max: <100 kDa

Solid-state nanopores	Molecule-by-molecule MW determination	Overestimation of low MW HA Can miss very low MW	Min: ~10 ng/10 uL Min: ~80 kDa
HPLC (High-Performance Liquid Chromatography)	Capable of detecting low concentrations Highly reproducible	Expensive and complex equipment	Min: ~ 3-11 µg/mL
NMR (Nuclear Magnetic Resonance)	Qualitative detection of HA	Poor resolution between MW's Some require modification/enrichment of HA	Min: ~ 50 mg/0.5mL
Carbazole Assay	Quantitative detection of HA Basic protocol	Inaccurate concentration readings at very high and very low MW Requires calibration curve Sensitive to salt content	Max: ~1 mg/mL

4.8.2 Development of Nanosight to access molecular weight distributions of polymers

Many of these methods are often used in an orthogonal fashion to exploit their respective perks and compensate for their individual failings, such as with SEC-MALLS. Recently, a new technology from Malvern, the Nanosight, has become a complementary partner to DLS, being especially useful for dilute, polydisperse samples.[113] The Nanosight pairs light scattering with particle tracking to determine particle concentrations and size distributions in a 100 µm x 80 µm x 10 µm field of view.[103] By tracking the Brownian motion of particles (or polymers) to determine a mean squared displacement (Equation 6, where x is the displacement, D is the diffusion constant, and t is the time) and

subsequently applies the Stokes-Einstein equation (Equation 7, where D is the diffusion constant, k_B is the Boltzmann constant, T is temperature, η is the solution viscosity, R_H is the hydrodynamic radius7), the size of the particles can be extracted.[114] Since the Nanosight tracks individual polymers in a known volume, it then can extrapolate concentration. The same approach is effectively done for ensemble averages in light scattering, and this is done with polymers all the time.

$$< x^2 > = 4Dt \tag{6}$$

$$D = \frac{k_B T}{6\pi\eta R_H} \tag{7}$$

DLS can be sensitive to larger particles and miss smaller ones, but the Nanosight can fully characterize a wide distribution of particle sizes in one sample. The Nanosight is even able to measure fluorescent samples, which as it turns out may be crucial to detect polymers like HA which only weakly scatter light.[101] An advantage of the Nanosight over HPLC is the ease of equipment use, quick data collection, and molecule-by-molecule counting so that full molecular weight distributions like that shown in Figure 17 can be achieved. Like the solid-state nanopore, the Nanosight can also make a molecule-by-molecule measurements of the concentration and size distribution of a sample. For weakly scattering samples like polymers, the smallest detectable particle by the Nanosight is about 40 nm in diameter and the largest is about 2000 nm. To determine the corresponding molecular weight for a 40 nm diameter particle and evaluate if the Nanosight has an advantage over the nanopore in measuring molecular weight, polymer physics predicts a relation between the polymer radius and the molecular weight as

$$R_H \sim MW^{\upsilon} \quad (8)$$

where R_H is the hydrodynamic radius, MW is the molecular weight and υ is the flory exponent, here assumed to be 0.7 for a linear polymer in a good solvent.[115] (See Section 4.2 for discussion of this choice for the flory exponent.) Therefore, the range of 40 nm - 2000 nm diameter particles corresponds to approximately 200 kDa – 20 MDa. The nanopores are more likely to detect particles between 80-200kDa, but the Nanosight can more reliably detect very large polymers, which we know the HA synthase is capable of synthesizing.

To the best of our knowledge, nobody has used the Nanosight to estimate molecular weight distributions of polymers. In hindsight, this may well be because polymers scatter light too weakly to be easily detected, even when they are large. However, the analysis presented below suggests that it should work if the scattering from the HA molecules is detectable, which we propose can be achieved when the polymers are fluorescently labeled. Additionally, we expect that ultimately the prefactors for the relation in Equation 8 can be determined using this technique with well-defined HA samples, and then we will be able to give accurate quantitative results for the molecular weight distribution of HA.

The key to single particle analysis like that of the Nanosight is to have sufficient statistics, but also to examine individual particles with no interactions, so that the analysis is not skewed. This leads to the requirement that the samples introduced to the Nanosight be ‘dilute’. Rule of thumb suggests that to avoid any kind of interactions, especially hydrodynamic which are the longest range, one wants to have an average distance of at least 10 times the radius of the particle. This sets a maximum concentration which will

allow for the maximal number of particles in the field of view without problems of coupling. It also makes it easier for the particle tracking algorithm to confidently identify the individual trajectories of each object so that the diffusion coefficient and hence radius can be determined.

A useful relation to find is the concentration (in mg/mL) needed to acquire a given number of particles/mL, since the Nanosight instructions suggest that the typical working range is 10^7 - 10^9 particles/mL:

$$c = 1.661 * 10^{-21} \frac{mg}{Da} * \ N * \langle MW \rangle \tag{9}$$

where c is the concentration of the HA solution (in mg/mL) and N is the number of particles per mL and <MW> is the average molecular weight in Daltons and we use the conversion for mg/Da, 1 amu.

However, our calculations suggest that for HA, the predicted spacing between the polymers that is associated with 10^7 - 10^9 particles is too low, so that we are well below the limit of the desirable ~100 particles per field of view. Therefore, we propose an independent calculation to generate an expression that shows what concentration (mg/mL) of HA should be used for a given average molecular weight, <MW>, such that the polymer spacing is ~xR, where x is a prefactor that we select and R is the polymer radius in microns. When xR = 10 μm, we achieve the goal of ~100 particles per field of view on average. This is a slightly larger spacing than the dilute criteria discussed above, but it also works and it conforms to the Nanosight instructions to have on average ~100 particles per field of view,

where the field of view is approximately 100 μm x 80 μm. Working through the math leads to the useful expression for the concentration:

$$c = \frac{10^{18}\,\frac{\mu m^3}{mL} * 1.661 * 10^{-21}\,\frac{mg}{Da} * \langle MW \rangle}{x^3 R^3} \tag{10}$$

where R is the radius of the particle in microns and x is a unitless measure of the number of radii we want between particles (distance between particles = x*R). The other prefactors ensure that the final units of the concentration, c, is in mg/mL. To summarize, this is the concentration of HA solution in mg/mL that one should use for a given average molecular weight and a desired spacing D, between particles of D = xR or in terms of the average molecular weight of the polymer, a desired spacing D = xR ~ x(<MW>$^{\upsilon}$). To minimize hydrodynamic coupling and other interactions, the value of x should be at least x = 10 so the particles are separated by 10 radii. For example, if we want D = 10 um between particles and the radius of the particle is ~ 0.5 μm, as it is for our Select-HA with a MW of 2500 kDa, then x = 20, and this leads to a calculation that the relevant concentration is 10^{-5} mg/mL HA or equivalently 10^{-2} ug/mL.

In what follows we present our efforts to 1) demonstrate the Nanosight works with monodisperse nanoparticles in measuring particle concentration and size; 2) establish high molecular weight HA is detectable; 3) measure monodisperse Select-HA. The fourth step would be to characterize the molecular weight distribution of HA produced by fragments in solution, to verify the validity of the technique compared to Figure 17, and produced in a brush conformation. This last step is obviously the motivation of development of this technique. However, to date, we have not quite reached this goal as the first three steps

have not been completed satisfactorily. Because much has been learned, and we are nearly to the point of determining whether the proposed technique is viable for our purposes, the details of the work thus far are included.

4.8.2.1 Control 200 nm nanoparticles

We first wanted to show that we had command of the machine and a thorough understanding of the software by measuring a well-defined sample. 200 nm polystyrene latex particles or beads (Fluospheres from ThermoFisher) come as a 2% solids solution in water. The number of particles/mL is defined by

$$\frac{Number\ of\ particles}{mL} = \frac{6\,C * 10^{12}}{\rho\,\pi\,\phi^3} \tag{11}$$

where C is the concentration of suspended beads per mL (2% solids corresponds with 0.02 g/mL), ρ is the density of polystyrene (1.05 g/mL), and ϕ is the diameter of the bead in microns. Therefore, the stock concentration of the beads is on the order of 10^{12} particles/mL. This solution was diluted to 10^9 particles/mL and measured (Figure 18).

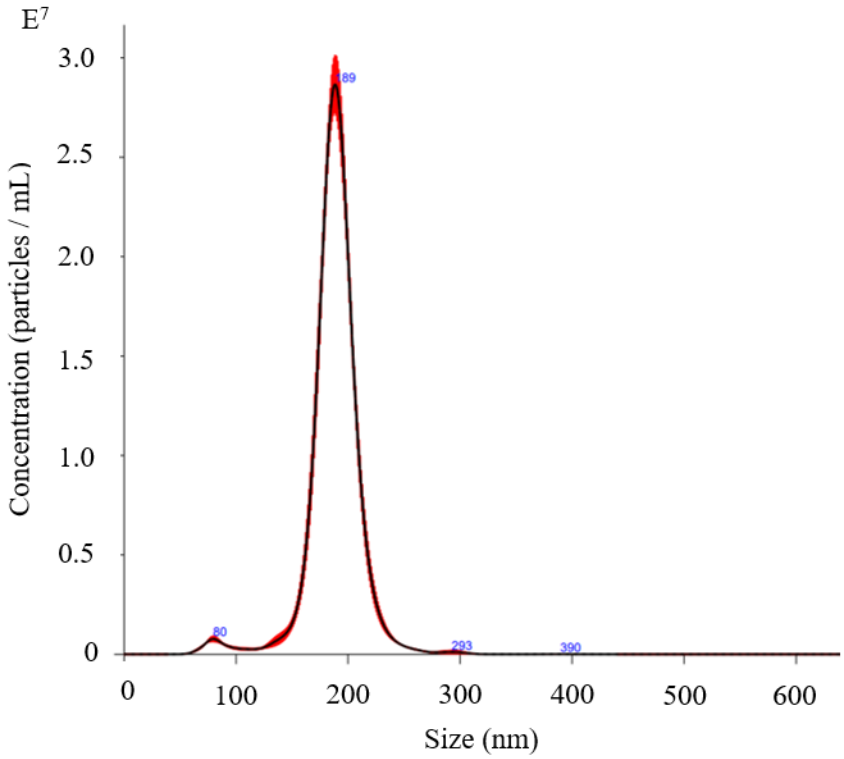

Figure 18. Size vs concentration for 200 nm particles measured by Nanosight over the course of 5, 60 second video captures. The black line is the average and the red is the error from the 5 separate measurements.

The Nanosight reported a total concentration of $1.10 \times 10^9 \pm 1.12 \times 10^7$ particles/mL and a mean size of 188 nm ± 24 nm. As reported by the manufacturer, the coefficient of variation (CV) for 0.02 µm beads is 20%, 0.1 µm beads is 5%, and 10-15 µm beads is 1%. Calculating the CV for the 200 nm particles (Equation 12) yields a value of ~13%, which falls between the 0.02 µm and 0.1 µm beads, while being closer in value to the 0.1 µm bead – as expected. Therefore, the results of the Nanosight measurement can be trusted in this case.

$$CV = \frac{Standard\ deviation}{Mean} \tag{12}$$

After a couple months break, a return to the Nanosight yielded unsettling results. Remeasuring the 200 nm particles as a control before measuring any new samples revealed a leak in the microfluidic device. As a result, the particles no longer remained in the main field of view during the video captures, but slowed drifted off screen over the course of the measurement. This increase in movement (in addition to the Brownian motion) resulted in a smaller calculated radius due to the MSD increasing, which increased D, and decreased R_H. The resulting size for the sample then was 139 ± 50 nm with a CV of 36%, clearly beyond the bounds of the technical specifications given by the manufacturer (Figure 19). Until the microfluidic device is replaced, all future size data reported will have a caveat of likely being smaller than the size of the actual sample. This unfortunately includes the data in the following sections, but it will become clear that the size information is not the reason for the failure of the technique thus far.

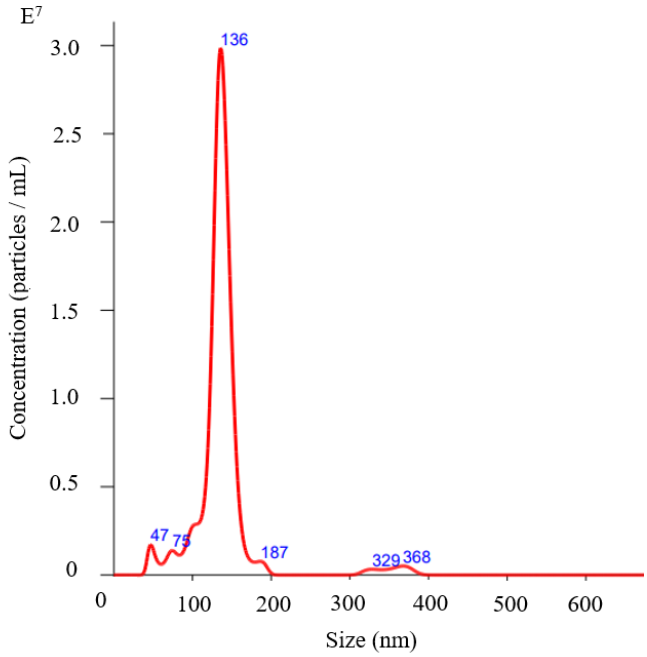

Figure 19. Size vs concentration for 200 nm particles measured by Nanosight over the course of 1, 60 second video capture represented by the red line.

4.8.2.2 Rooster comb HA (expected average molecular weight 1 MDa).

Rooster comb HA is known for its ultra-high molecular weight, with lengths as large as 25 μm (10 MDa). To measure any sample in the Nanosight, the first step is to calculate the approximate concentration necessary. For the experiments reported in the thesis, we had not yet understood that the default Nanosight instructions should be adjusted for HA samples, so we followed the operator's manual where the ideal concentration is 10^7 – 10^9 particles per mL. Furthermore, while we expected large polymers according to the manufacturer, troubleshooting later revealed that the HA <MW> is closer to 100 kDa rather than 1 MDa. This will be discussed in Section 4.8.3.

In our experiments, we titrated the rooster comb HA and made measurements at c = 0.1 mg/mL, 2 mg/mL, and 5 mg/mL with increasing concentrations because nothing could be 'seen' at the lower concentrations. Assuming a <MW> = 100 kDa, this corresponded to separation distances of ~ 11 μm, ~4 μm, ~3 μm, respectively, and an estimated 57, 420, and 774 particles per field of view. Consistently, for any concentration, the detected number of particles was very low and the Nanosight's reported sample concentration (~10^6 - 10^7 particles/mL) was lower than predicted (10^7 - 10^8 particles/mL) by orders of magnitude. Most concerning, the expected R_H for a 100 kDa sample (according to Equation 8) is ~50 nm and the reported size distribution has much larger particles present and the error (represented by the width of the red band around the mean in black) is very wide, indicating big differences in size distribution from one video capture measurement to another within one sample and no consistency from one concentration to another (Figure 20).

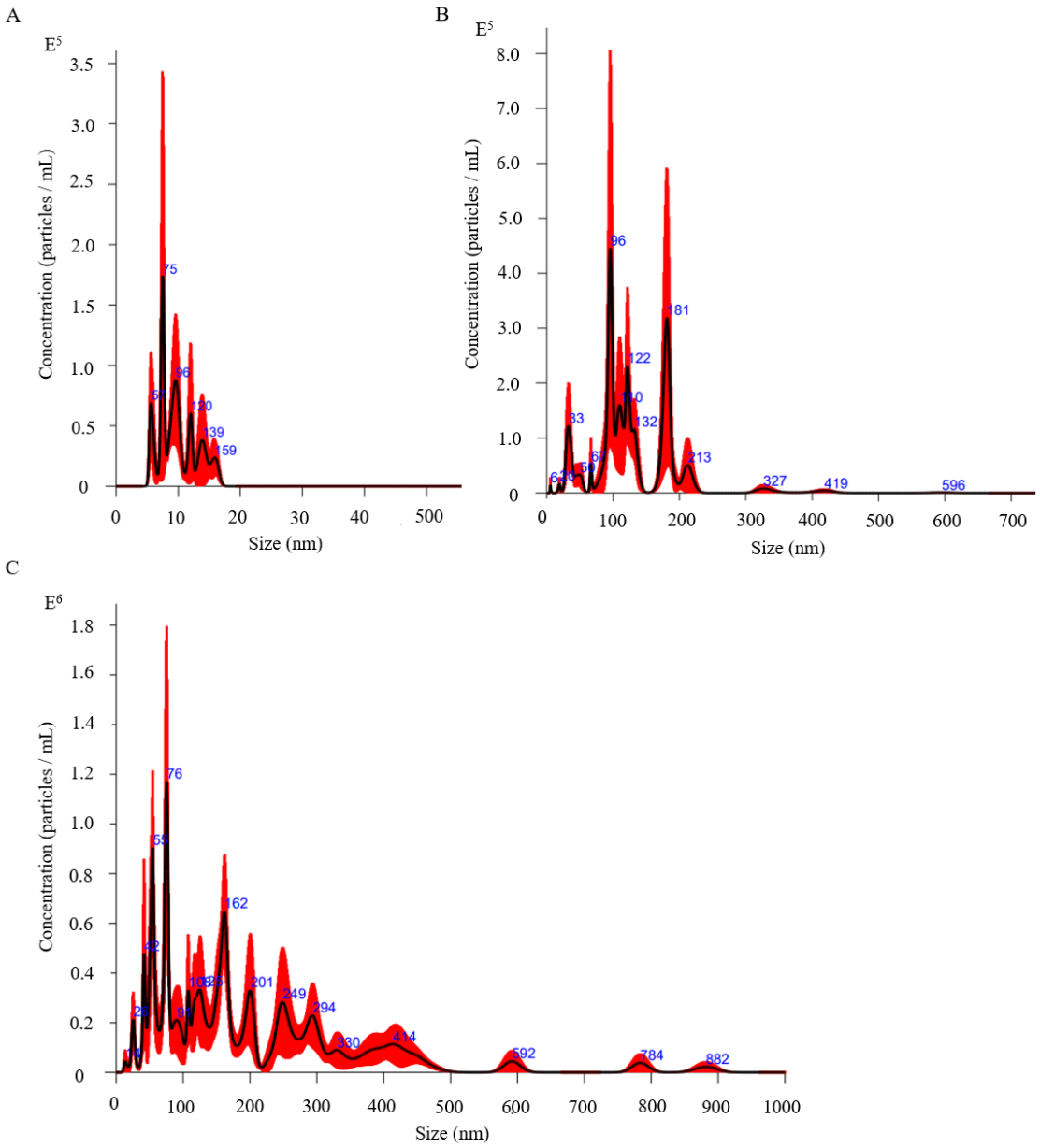

Figure 20. Size vs concentration for rooster comb HA measured by Nanosight over the course of 5, 60 second video captures under slow flow. The black line is the average and the red is the error from the 5 separate measurements. A) 0.1 mg/mL B) 2 mg/mL C) 5 mg/mL.

We naively thought that the issue was the sticking of the HA to the tubing, loss somewhere along the way of sample prep, or issues with rehydrating the HA during dilution. Changing the containers to glass or tubing meant for minimal polymer losses (low binding) did not effect the order of magnitude reported for concentration. The Nanosight is capable of applying a flow in the case of low concentrations in an effort to increase the number of particles measured per capture, but even this did not increase the reported particle concentration or narrow the error. However, in hindsight, we now understand that the HA likely scatters too little to be detectable.

4.8.2.3 Monodisperse Select-HA, 2500 kDa

Our original efforts focused on rooster comb HA because it is both cheap and we naively assumed it would have a bigger average MW than 1 MDa, since literature repeatedly states rooster comb is 25 μm in length, corresponding to 10 MDa. Calling the manufacturer (after lots of troubleshooting) revealed their expected value of 1 MDa and gel electrophoresis revealed ~100 kDa. Hence, we moved on to another sample with larger polymers and a well-defined molecular weight. Select-HA from Hyalose (now Echelon) is monodisperse HA with a molecular weight of 2500 kDa.

Again, estimating the concentration of HA proved to be a significant hurdle in preparing the HA samples for the Nanosight. Rehydrating the lyophilized HA from the manufacturer resulted in a very thick gel-like solution which would be incapable of being run through the Nanosight. To reach the ideal Nanosight concentration range, serial dilutions were performed. The resulting calculated concentrations were very different from

the reported concentrations from measurements. Generally, the reported measurements were many orders of magnitude lower than the expected/calculated concentrations.

We titrated the Select-HA and made measurements at c = 0.001 mg/mL, 0.01 mg/mL, and 0.1 mg/mL where the predicted particles/mL are 10^{14}, 10^{15}, and 10^{16}, respectively. 10^{14} – 10^{16} particles/mL should be well above the maximum resolvable concentration for the Nanosight, but still nothing could be 'seen' at the lower concentrations. As outlined in Section 4.8.2, these concentrations should be much too high for a reasonable number of particles in the field of view. Despite this expectation, the Nanosight's reported sample concentration (~10^7 particles/mL) was lower than predicted (10^{14} – 10^{16} particles/mL) by many orders of magnitude. Even more troubling, size distributions do not indicate a monodisperse sample whose expected R_H is ~ 500 nm (Figure below). The Select-HA has been stored in the lab for a long time, so it is possible that the sample has degraded over time resulting in smaller MW pieces than expected which would affect the expected concentration calculations. Ordering newer samples of Select-HA is a non-negligible solution to the aging hypothesis due to there only being one company that provides this product and, as of this writing, they are out of stock with no known restock date.

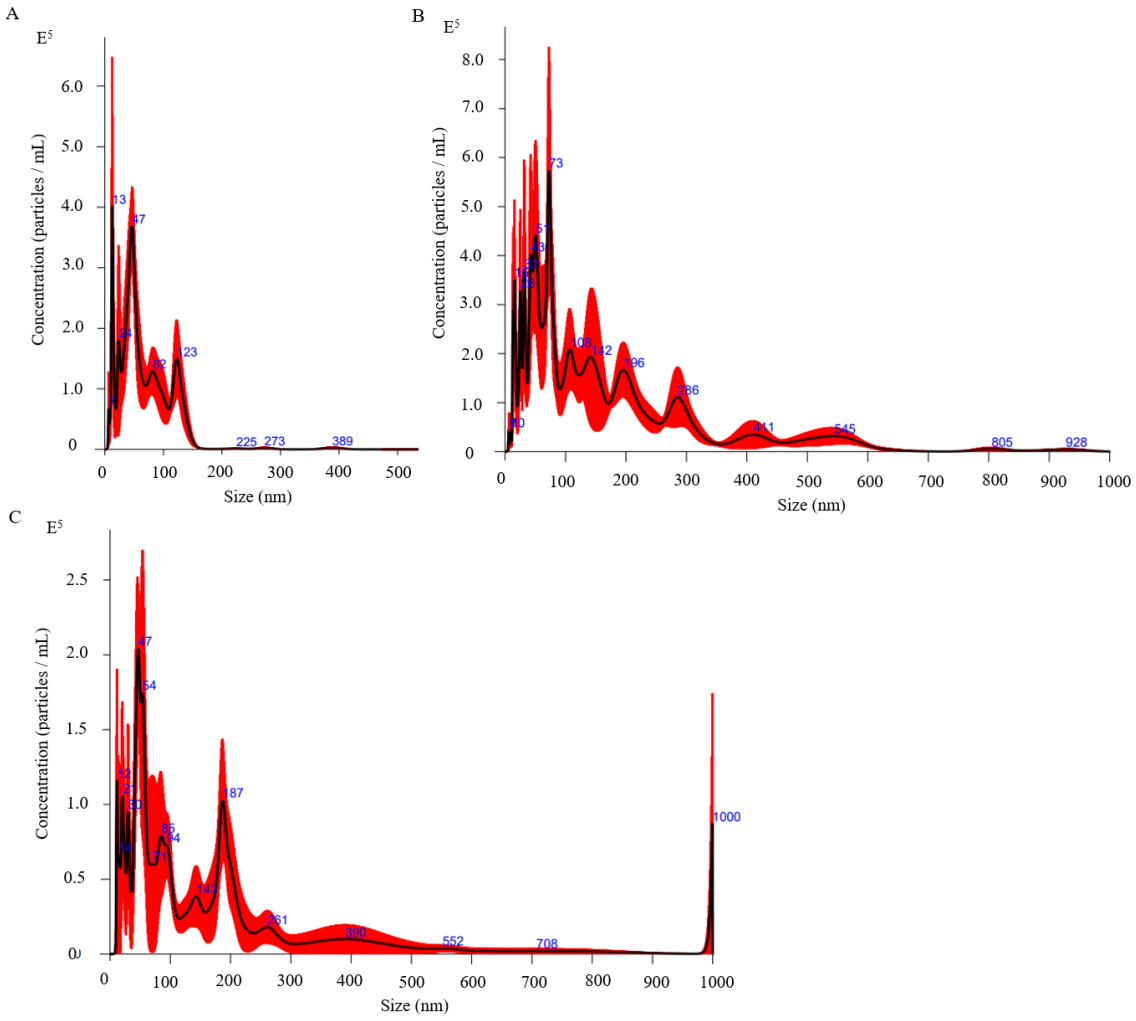

Figure 21. Size vs concentration for 2500 kDa HA measured by Nanosight over the course of 5, 60 second video captures under slow flow. The black line is the average and the red is the error from the 5 separate measurements. A) 0.001 mg/mL B) 0.01 mg/mL C) 0.1 mg/mL.

Currently, the success of this project has been limited thus far. However, we have established deep familiarity with the various aspects necessary to make this project work ranging from sample prep and handling, the Nanosight, the use of HA within the Nanosight, and a good understanding of what concentrations to use. Most importantly, the troubleshooting has led to the clear conclusion that the fundamental limiting factor thus far is the fact that HA scatters too weakly. We missed this point originally because we had

positive results when measuring at much higher concentrations of HA, but where the Nanosight reported low concentrations in the right ballpark – so we missed this basic issue. Moving forward, we are optimistic that fluorescently labeling the HA and working with the Nanosight in fluorescence detection mode, will resolve the issues we have reported thus far, and allow us to establish this powerful method to extract length distributions of HA. For our lab, this will be a game changer, because there are many scenarios where having this information would be incredibly valuable to link the experimental results to theoretical predictions.

4.8.3 Complementary agarose gel molecular weight distribution

Agarose gel electrophoresis is a quick way to establish the range of molecular weights in a sample when compared to a standard or ladder. Due to the inconsistent results from the Nanosight, it seemed like a good idea to verify the MW of the rooster comb and the Select-HA since the rooster comb HA MW distributions were inconsistent and the Select-HA MW was not monodisperse.

Figure 22 shows the results of running the samples on a 0.5% agarose gel for 3.5 hrs at 34 V and stained with 0.005% StainsAll.[100] The ladders are dimmer than expected, likely due to the choice of a wide well. The rooster comb HA showed an average of ~100 kDa (the widest part of the banding) rather than expected 1 MDa. The 2500 kDa HA appears to have the appropriate MW, but there is a distinct smear of smaller sizes, especially when compared to the ladders which have clear banding and little smear. This supports our hypothesis of possible degradation due to the presence of smaller polymers.

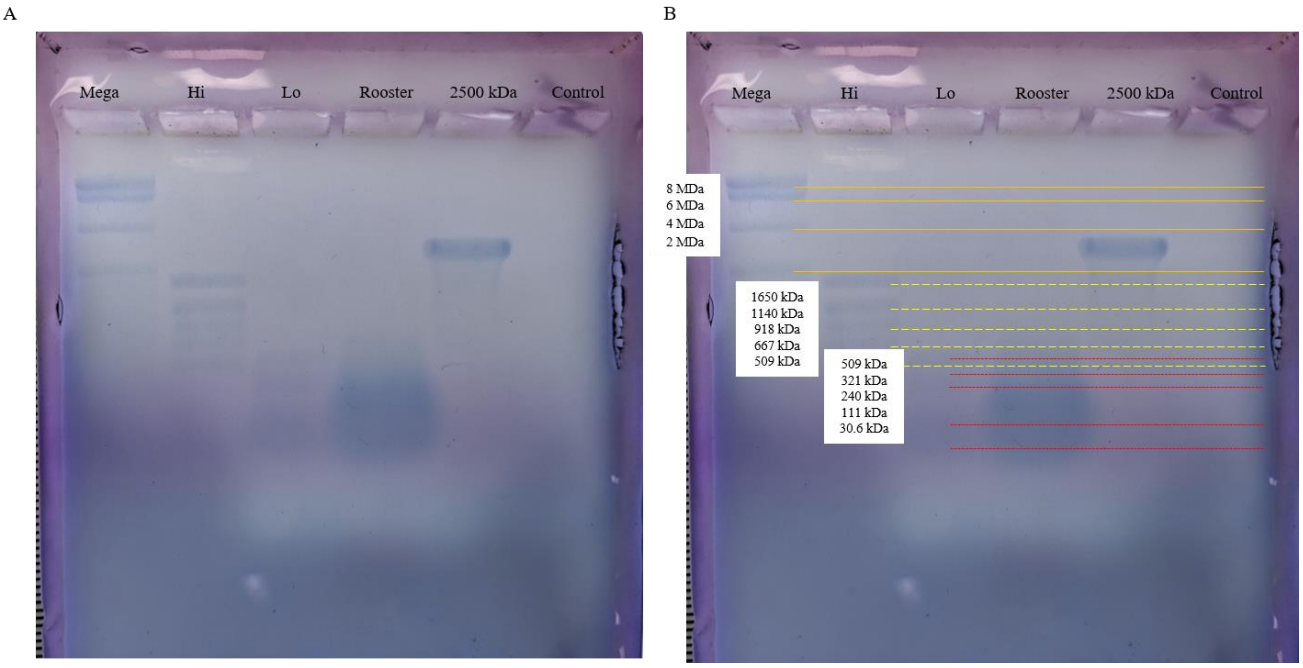

Figure 22. Agarose gel after staining with StainsAll – both A and B are the same gel. From left to right: Select-HA MegaLadder, Select-HA HiLadder, Select-HA LoLadder, Rooster Comb HA (5 mg/mL), Select-HA 2500 kDa (0.1 mg/mL), Control (water). A) Gel with wells labeled. B) Gel with ladder sizes labeled. Mega (orange), Hi (yellow, wide dashes), Lo (red, skinny dashes).

Finally, we wanted to look at the MW distribution of HA grown in a brush configuration. A 4 hr brush was chosen due to the extensive characterization done on brushes of that growth time and since a complementary MW distribution exists (Figure 17) for HA grown in solution for 4 hrs as measured by the nanopores. Briefly, the HA was collected from the brush using SDS to disrupt the membranes which would cause the brush to fall apart. The collected solution (SDS, fragments, and HA) was heat-shocked to denature the HAS enzymes and cause them to release any bound HA into solution. Following a Folch treatment which separates the lipids from the carbohydrates, the purified

HA solution was concentrated and measured in a gel along with other known solutions (Figure 23).

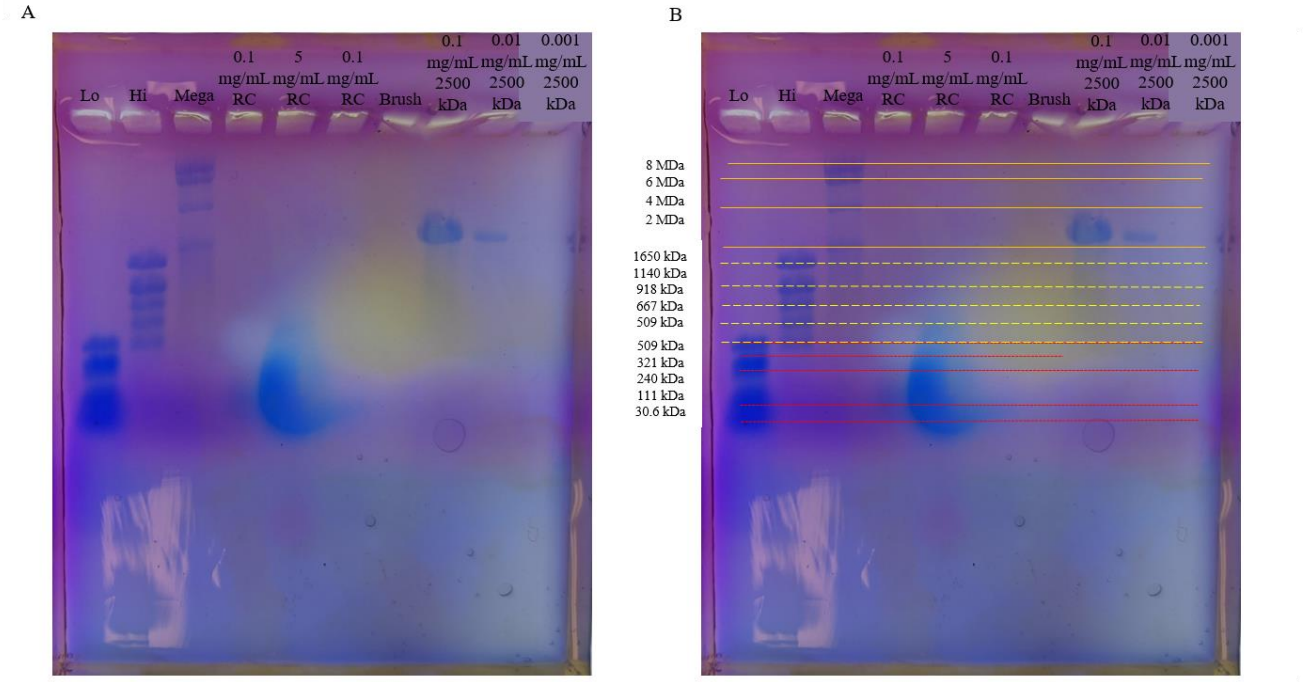

Figure 23. Agarose gel after staining with StainsAll – both A and B are the same gel. From left to right: Select-HA LoLadder, Select-HA HiLadder, Select-HA MegaLadder, Rooster Comb HA (hydrated at 0.1 mg/mL), Rooster Comb HA (hydrated at 5 mg/mL), Rooster Comb HA (0.1 mg/mL, diluted from 5 mg/mL), HA from 4 hr brush, Select-HA 2500 kDa (0.1 mg/mL), Select-HA 2500 kDa (0.01 mg/mL), Select-HA 2500 kDa (0.001 mg/mL). A) Gel with wells labeled. B) Gel with ladder sizes labeled. Mega (orange), Hi (yellow, wide dashes), Lo (red, skinny dashes).

Skinnier wells were chosen to improve the saturation of the ladder banding. A few concentrations of rooster comb were measured to check dilutions and check for reproducibility. A few concentrations of 2500 kDa HA were also measured as a sanity check on the dilutions. The high concentration (5 mg/mL) rooster comb had a similar billowing out side-to-side and mostly obscured the adjacent lanes. It's difficult to determine if this billowing/spilling to the adjacent lane is an effect of size or concentration since the lower concentration lanes are nearly invisible comparatively. The decreasing

concentrations of 2500 kDa have decreasing saturations due to staining which is a nice sanity check on the validity of the dilution protocol.

The worst upset here is that the lane with the HA purified from a brush is yellow. The StainsAll turns carbohydrates blue, but it turns lipids yellow. Despite the Folch procedure, there appears to be a significant amount of lipid still in the sample. Previous HA purification during nanopore sample prep did not require the use of SDS since the fragments and HA did not need to be removed from a surface. The SDS, a detergent, is likely forming hybrid micelles with the lipids from the membrane fragments and these lipids are remaining in the Folch layer for carbohydrates rather than being separated. When there is SDS in a liquid sample, bubbles tend to form during pipetting. The purified HA solution forms small bubbles on the surface during pipetting, qualitatively indicating the presence of SDS in the final solution. SDS can easily be removed from the solution by ethanol precipitation of the HA. The HA will be precipitated and the supernatant removed, with the SDS along with it. Then, the HA can be rehydrated and run on a fresh gel. After verifying the removal of SDS by the lack of yellow staining in the gel, the sample can be run through the Nanosight for a complementary measurement of size, and therefore MW.

Other optimizations need to be performed, such as verifying that the gel is a consistent 0.5% agarose gel. Some protocols call for a step where the agarose powder is allowed to sit for a few minutes in the TAE buffer before dissolving with the aid of heat. It is possible that the powder is not properly dissolved or the gel is not properly mixed since the parameters chosen for the voltage and timing were motivated by Rivas et al. and the samples should be running further than only halfway through the gel.[100] The gel should also be stained and washed under gentle agitation, such as a with a gentle rocking motion,

but the rocker in the lab is broken so the gels sat undisturbed in the lab bench during both staining and washing. New parts are being tracked down to fix the rocker and it is possible that a more even staining will result if the rocker is used in the future.

4.9 Brush concentration profile and comparison with theory

The HA brushes are very polydisperse, but they're also incredibly thick and the HA is not anchored in a uniform lattice structure on the surface. Therefore, it is not a given that the monomer concentration profile would naturally follow the theory presented in Section 2.3.1 of a convex-like profile. There are many methods used in the literature to extract a polymer concentration profile, such as quartz microbalance and ellipsometry. The most straightforward method though would be fluorescent labeling of the brush itself. Again, due to the very thick nature of these brushes, we are able to visualize the fluorescent brush with confocal microscopy – something that thinner brushes would be incapable of achieving and offers a unique perspective and unprecedented spatial resolution.

We developed two methodologies to fluorescently label the HA brushes: 1) Covalent binding fluorophores using EDC/NHS carbiomide chemistry, 2) incorporating an azide-modified N-acetylglucosamine (N-azidoacetylglucosamine tetraacylated, aka GlcNAz) into the synthesized HA strands and then "clicking" in a fluorophore to the azide link on the HA. We performed a quantitative assessment of the brush concentration profile versus growth time, compared the heights indicated by the fluorescent labeling with the particle exclusion assays, and considered how the differences in profile reflect the time-dependent molecular weight distribution of the HA brush. This might seem like a natural and straightforward progression of analysis, but they are only available to us due to the

huge thicknesses of the brushes and the ease of analysis with confocal microscopy. As we will discuss in detail below, both labeling schemes worked well (Figure 24) and have convex profiles as expected for polydisperse brushes (Figure 6B). However, in order to perform a quantitative analysis of the brush profile, we had to first deal with background resulting from dye sticking non-specifically to the substrate.

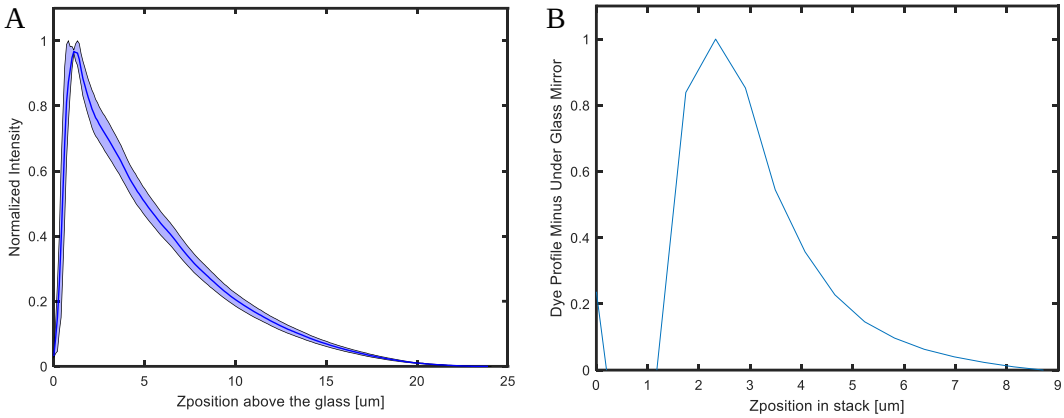

Figure 24. A) Fluorescent brush profile (4 hr unreinforced brush) from covalently binding fluorophores using EDC/NHS carbiomide chemistry, B) Fluorescent brush profile (16 hr unreinforced brush) from incorporating GlcNAz into the synthesized HA strands and then "clicking" in a fluorophore to the azide link on the HA.

4.9.1 Surface labeling and self-quenching

During labeling experiments, it became increasingly obvious that the fragment surfaces were incredibly "sticky". The fluorescent dyes used to label the brush also stick to the surface, resulting in a bright peak of intensity located at the surface. This unwanted intensity from the underlying substrate interferes with the quantitative assessment of the brush concentration profile. We therefore attempted multiple treatments to passivate the surface by 1) incubating the surface with BSA (bovine serum albumin), an inert protein, 2) using NHS-ester to bind to any amines on the PEI that might be free to otherwise allow

dye to bind, and 3) using adipic dihydrazide to bind to any carboxyl groups on the GA that might be free to otherwise allow dye to bind. In this way, a hydrazide-fluorophore would be unable to bind to the surface, chemically or non-specifically. 4.) Decreasing the concentration of the dye. Unfortunately, our efforts in this regard were unsuccessful. Dye always found a way to bind to the surface, even with all tree treatments applied to the same surface. We even scaled back the surface complexity to just PEI on glass to troubleshoot one layer at a time and never successfully kept the dye from binding. In the future, backfilling with short PEG (polyethylene glycol) polymers, known for their inert nature, might offer a path forward to passivating the surface.

Another issue that arose was that of fluorescence self-quenching. Quenching occurs when the fluorescent intensity of a substance is decreased [116]. Self-quenching is a special case where the fluorophore and the quencher are the same molecule and often occurs when there are high concentrations of fluorophores [116, 117]. Photobleaching is a result of dye being altered permanently by laser light and results in the fluorophore's inability to fluoresce. Over time, this will appear as if the sample fluorescence is fading. In our case, we have a high concentration of fluorophores bound to the fragment surface. When we imaged the surface, we noticed that the regions imaged would appear to get brighter over time, rather than dimmer. Due to the high density of dye stuck to the surfaces, we had reached a self-quenching scenario. (Figure 25A) Over time and with repeated laser application, this self-quenching would eventually be overcome and the surface would finally become dimmer than its initial intensity. (Figure 25B)

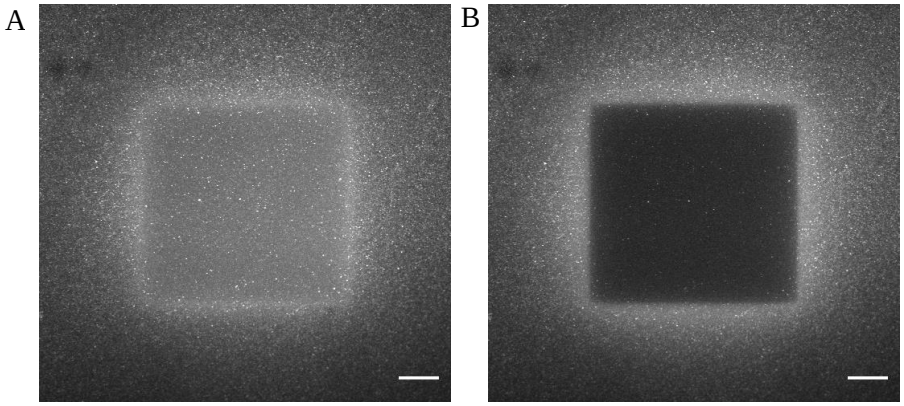

Figure 25. Wide (~200 x 200 μm^2) view of a ~100 x 100 μm^2 area that was imaged. A) Brighter dye inside the imaged area indicates self-quenching. B) The imaged area finally is photobleached beyond self-quenching regime.

Figure 26 shows an Alexa Flour-hydrazide fluorescently labeled fragment surface with no brush present. Repeated zstacks were taken at the same location with no parameter adjustments between images. The numbering in the legend represents the sequence of zstacks. After the first zstack, the intensity of the surface (at the peak, 0 μm) increases and remains higher than the original intensity for the next 3 stacks. It is not until stack 4 that the intensity begins to drop incrementally with each following stack. This surface labeling make extracting the true dye profile near the surface tricky, but it does provide an alternative avenue to finding the z-position of the underlying fragment, a necessary parameter in the extraction of the brush height.

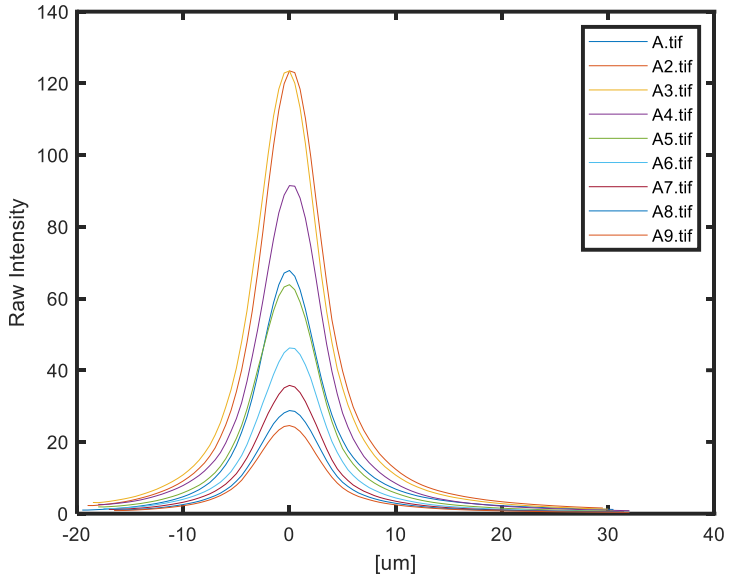

Figure 26. Fluorescent profiles of dye on a fragment surface with no brush present. Increasing numbering in the legend corresponds to subsequent zstacks, demonstrating an initial increase in surface brightness and then a slow decrease in brightness due to photobleaching from repeated laser exposures.

To decrease the effect of this surface peak on the resulting brush profile, we investigated decreasing the dye concentration so that less binds to the surface, and as an additional bonus, we might possibly eliminate the self-quenching. Figure 27 shows that as the fluorescent dye is decreased by orders of magnitude from 1 mg/mL to 0.0001 mg/mL, the brush profile vanishes (approaching a Gaussian shape that reflects only dye on the surface, such as in Figure 26) due to the lack of sufficient dye bound within the brush, necessitating the continued use of 1 mg/mL of dye.

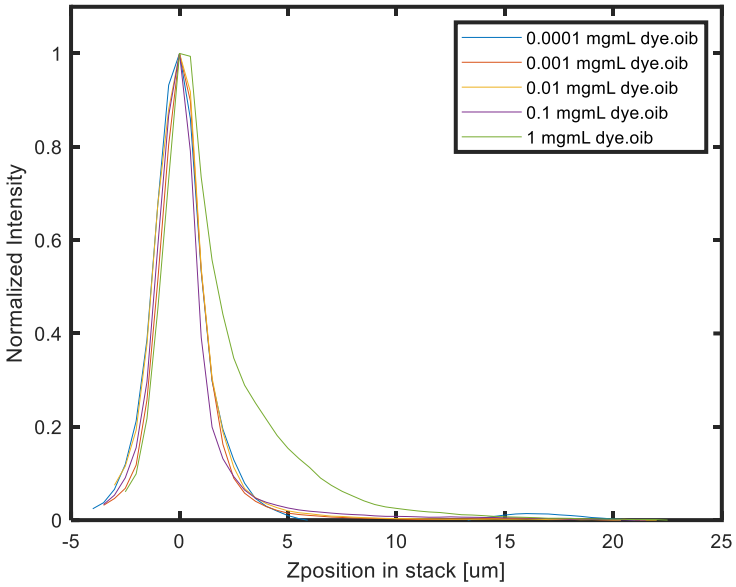

Figure 27. Fluorescent dye profiles for varying concentrations of dye for a 4 hr reinforced brush. For any concentrations lower than 1 mg/mL, the fluorescent profile vanishes (approach a Gaussian shape).

4.9.2 Mirrored background subtraction

To deal with the unmitigated surface binding of any fluorophore, we devised a method to perform a background subtraction such that the influence of the surface brightness could be subtracted from the profile leaving just the intensity profile representative of the fluorophore in the brush. The profiles of the dye on a fragment surface without brush are beautifully fit with a Gaussian (Figure 26), demonstrating equal intensity above and below the glass interface (the peak of the intensity). A brush profile is not Gaussian, as evidenced in Figure 24 and is rather more convex, exponential-like. Therefore, despite a Gaussian being a good fit for dye alone, a Gaussian fitted to a brush profile would not be centered at the glass interface and therefore should not be used to subtract the surface brightness (henceforth referred to as background).

A straightforward way to mimic a Gaussian profile would be to copy the left half of the curve and mirror it about the peak. Figure 28 demonstrates how closely this mimics the Gaussian. To use this 'mirrored subtraction' method, the part of the profile under the glass (to the left of the peak) will be mirrored about the peak. This will unfortunately not contain enough data to subtract this background from more than the first couple of microns of the brush. Therefore, the rest of the background profile will be filled in with the first value of the intensity profile (deepest under the glass, furthest to the left). Now that we have two profiles of equal length arrays, they can easily be subtracted, leaving the profile of just the fluorophore inside the brush.

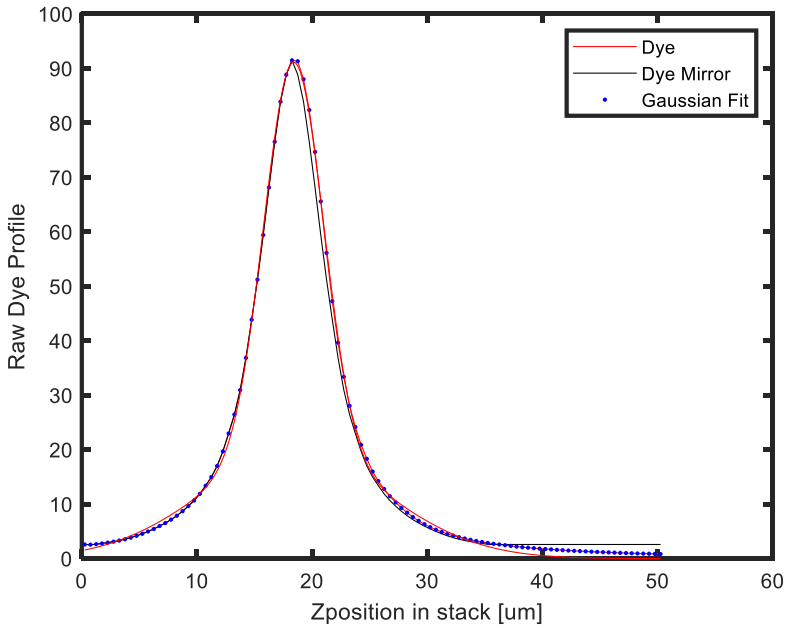

Figure 28. Fluorescent dye profile (red) on fragment-only surface, no brush. The Gaussian fit (blue) and 'mirrored background' (black) both fit the dye profile well.

It became clear in designing this 'mirrored subtraction' method that smaller z-steps would need to be taken during imaging. If larger steps, like the 500 nm steps usually taken, are used, then the true peak of the dye on the glass substrate could be lost. Figure 29

demonstrates a case where the finite steps taken during a zstack will not always precisely capture the true peak. Subsequently, the 'mirrored subtraction' method will be unable to located the true glass interface and the mirrored profile will be inaccurate and result in an incorrect subtracted profile. The error introduced here can be mitigated by taking sufficiently small zstack steps of 100 nm.

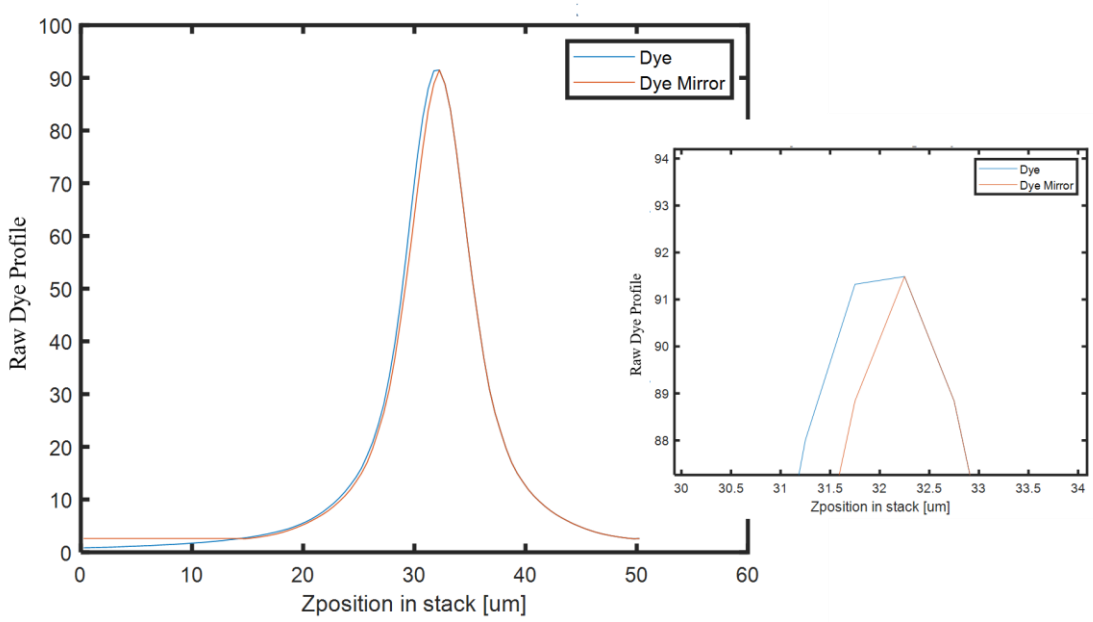

Figure 29. Fluorescent dye profile with the mirrored background. The inset shows the peak zoomed to highlight the stepwise cutoff of the real peak of the dye profile. The mirror will then be shifted slightly due to an alignment with the left or right side of the broken peak. N = 1 spot measured per labeled brush.

4.9.3 Carbodiimide chemistry

Figure 30 shows brushes grown for different time points (1, 2, and 4 hrs) and labeled with an Alexa Fluor-hydrazide dye in both 150 mM NaCl and water. Figure 30 shows that the familiar convex-shaped profile (recall Figure 6B) appears for all brushes. Each profile report the mean from two measurements per sample and a standard error represented by the wider band around the mean. As one might expect, in 150 mM NaCl,

the profiles extend further as the brushes grow for longer. Recall that inside polydisperse brushes that the presence of shorter polymers causes extension of the longer adjacent polymers. In a salt solution, charges along the polymer backbone will be more screened and the polymer will be in a more coiled state than in water. In water, when the polymers are fully extended, there is an interesting crossover between the 2 hr and 4 hr profiles, likely a hint at the changing polydispersity index and molecular weight distribution within the brush.

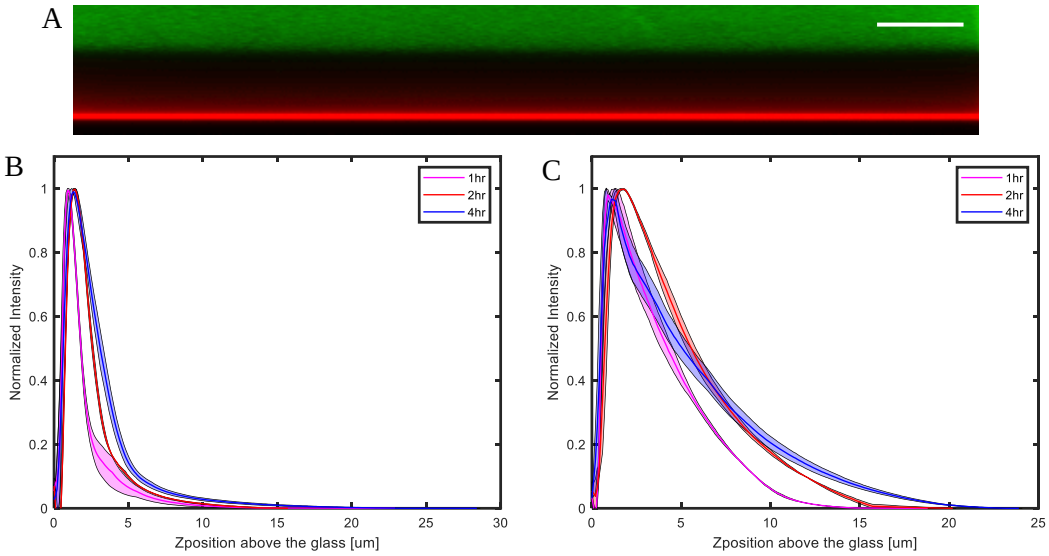

Figure 30. A) Fluorescently labeled 4 hr, unreinforced brush. Dye is red, 200 nm green nanoparticles are excluded from the brush and highlight the upper bound. Scale bar is 10 µm. B and C) Fluorescent dye profiles for brushes grown 1 (pink), 2 (red), and 4 (blue) hrs. Each profile is represented by a mean with a corresponding color band representing standard error from N = 2 spots measure per N = 1 sample. A) 150 mM NaCl, B) Water.

The comparison of a 4 hr brush to a 16 hr brush (Figure 31) produces an unexpected result. In contradiction to particle exclusion assay results (in 150 mM NaCl, Figure 8A), the 16 hr brush has a more compressed profile when compared to the 4 hr brush in salt solution. Particle exclusion assays on these fluorescently labeled brushes suggest that the 16 hr brush is ~ 4.5 μm tall rather than the expected ~10 μm in 150 mM NaCl. Meanwhile, in ultrapure water, the very same brush, now stretched due to the removal of salt, measures ~18 um in water using particle exclusion assay, which is close to the ~20 μm expected height from previous experiments (Figure 8C). In fact, after fluorescent labeling, we find that all the brushes are slightly shorter than expected in salt solution and generally taller than expected in water (Table 4). Even more interesting is that the average height of the brushes in water for fluorescent brushes is ~ 400% taller than in salt, compared to ~ 200% for unlabeled brushes. Both the 4 hr and 16 hr brushes in water have similarly extended profiles and even similar heights when measured with a particle exclusion assay.

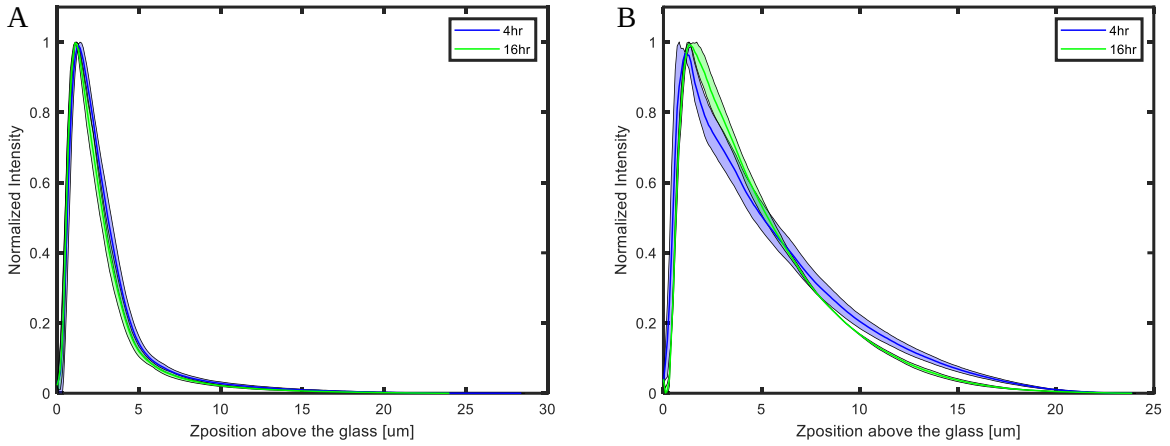

Figure 31. Fluorescent dye profiles for brushes grown 4 (blue) and 16 (green) hrs. Each profile is represented by a mean with a corresponding color band representing standard error from N = 2 spots measure per N = 1 sample. A) 150 mM NaCl, B) Water.

Table 4. Brush heights for fluorescently labeled and unlabeled brushes grown for various times and measured in 150 mM NaCl (salt) and water.

	Fluorescently Labeled Brushes					Unlabeled Brushes			
	Salt		Water			Salt		Water	
t_{growth}	Avg	stdev	Avg	stdev	Extension	Avg	stdev	Approx	Extension
1	2.39	0.01	8.68	0.05	363%	2.62	0.22	unknown	
2	3.43	0.16	14.94	0.52	436%	4.05	0.38	unknown	
4	4.77	0.06	22.28	0.34	467%	5.89	0.67	15	255%
16	4.27	0.23	18.23	0.78	427%	10.64	0.97	22	207%

In every case (all growth times and both solutions), the brush height is different than expected. The presence of the fluorophore must be the reason. The fluorophore binds to the carboxylic acid, which is responsible for the negative charge along the backbone of

HA. So when there is a fluorophore bound, it removes one of these charges and reduces the charge of the HA, but also adds some additional bulk to the polymer (MW of the Alexa Fluor 647 hydrazide is ~ 1200 Da). Figure 32 shows the molecular structure of the fluorophore which is highly sulfated and therefore highly negatively charged.[118] In salt, the brushes are likely shorter than when unlabeled due to loses from the labeling protocol and washing. In water, the fluorophore, being more negatively charged, will attract more water molecules than an individual carboxyl group and therefore the brushes become significantly more hydrated than they would have without the fluorophore. In the case of the 16 hr brush, we know we are already reaching a plateau in brush height (Figure 8) and therefore a maximum in polymer length. Thus, the polymers are already stretched out to nearly their maximum in water and the added fluorophore does not add additional extension.

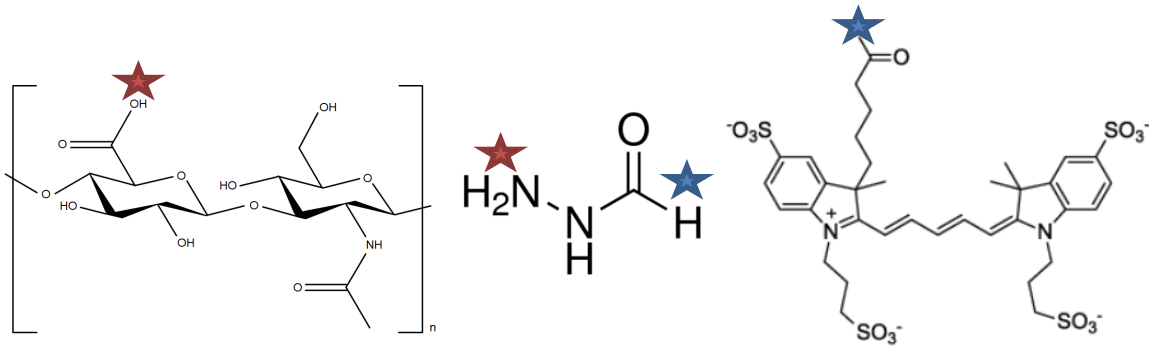

Figure 32. The fluorophore binding to hyaluronan is facilitated by a hydrazide. The red stars represent where the hydrazide will bind to the hyaluronan. The blue starts represent where the fluorophore is bound to the hydrazide component. Structure of hydrazide image downloaded from https://www.sigmaaldrich.com/catalog/product/aldrich/166375. Structure of Alexa Fluor 647 image downloaded from https://www.atdbio.com/content/34/Alexa-dyes in March 2019.

Finally, it is important to highlight the significance of the use of EDC chemistry here. This is the same chemistry used to reinforce the brushes. The time for labeling (1 hr) and the time for reinforcement (overnight) differs significantly, but the reactions necessary are very sensitive to water as the reactive intermediates of the carbodiimide chemistry are unstable to hydrolysis and have a half-life on the order of minutes, depending on temperature and pH.[119, 120] If the labeled brushes are being effectively reinforced while also being labeled, then any molecular weight distribution extracted from unreinforced brushes might not map directly to these brushes. Further work investigating the effect of timing on reinforcement should be performed, such as application of SDS to a labeled brush, as well as a comparative analysis of the molecular weight distribution of the unlabeled and labeled brushes for a given growth time.

4.9.4 Comparison of brush height as determined by fluorescent dye vs particle exclusion assay

We noticed that the particle exclusion assays (PEA) consistently seemed to underestimate the thickness of the brush when compared to the fluorescent profile, as there is clearly brush present (profile continues) beyond the PEA-defined edge. An alternative method for brush height determination would use the fluorescent dye profile itself. Therefore, the edge (or upper surface that defines the thickness) of the brush is defined as where the difference between 2 indices of the dye profile is greater than twice the moving standard deviation across 5 indices of the dye profile. This will capture where the profile starts to level off and defines a background by examining a moving standard deviation across the entire profile.

Figure 33 and Figure 34 show average fluorescent profiles for 1, 2, 4, and 16 hr brushes in 150 mM NaCl and water with PEA brush heights and dye profile brush heights labeled. (Quantified in Table 5). Applying the moving difference/moving standard deviation method of determining where the profile becomes background consistently determines the brushes to be thicker than PEA when measured in salt solution. The 4 and 16 hr brushes in water have the opposite trend. It is likely that this is due to a lack of profile to run the moving difference/moving standard deviation algorithm over since the brushes are so thick and the zstacks do not capture a significant amount of the profile above the brush, as is the case with the salted brushes and with the shorter 1 and 2 hr brushes in water. Repeating this experiment and collecting more data above the brush will determine if this

is a real phenomenon or an artifact. Another reason the brush heights as determined by the different methods could be different is because the dye profile is collected without any of the 200 nm beads that are necessary for brush height via PEA measurements. The presence of 200 nm beads could have an osmotic pressure effect on the height of the brush, driving the brush height down from the real thickness in the absence of nanoparticles.

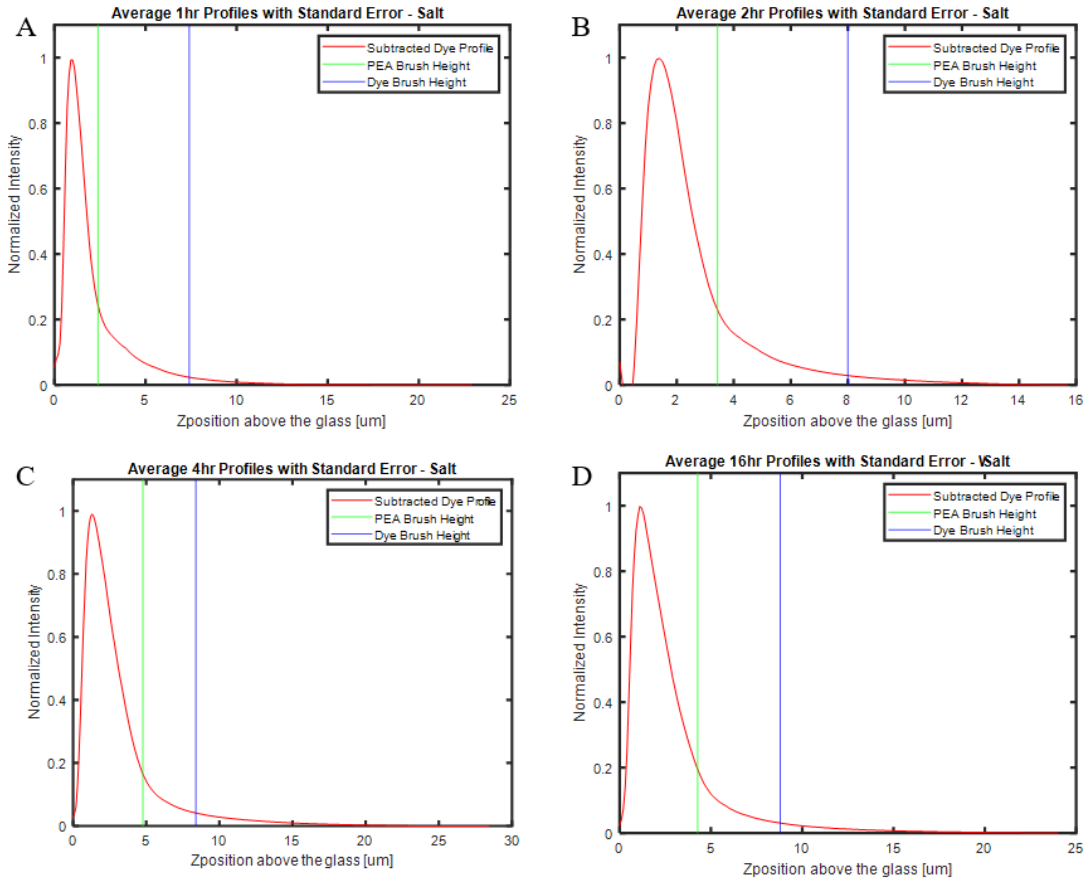

Figure 33. Fluorescent profiles (red) for 1, 2, 4, and 16 hr brushes in 150 mM NaCl where the height of the brush as determined by PEA is marked green and as determined by the dye profile background is marked in blue.

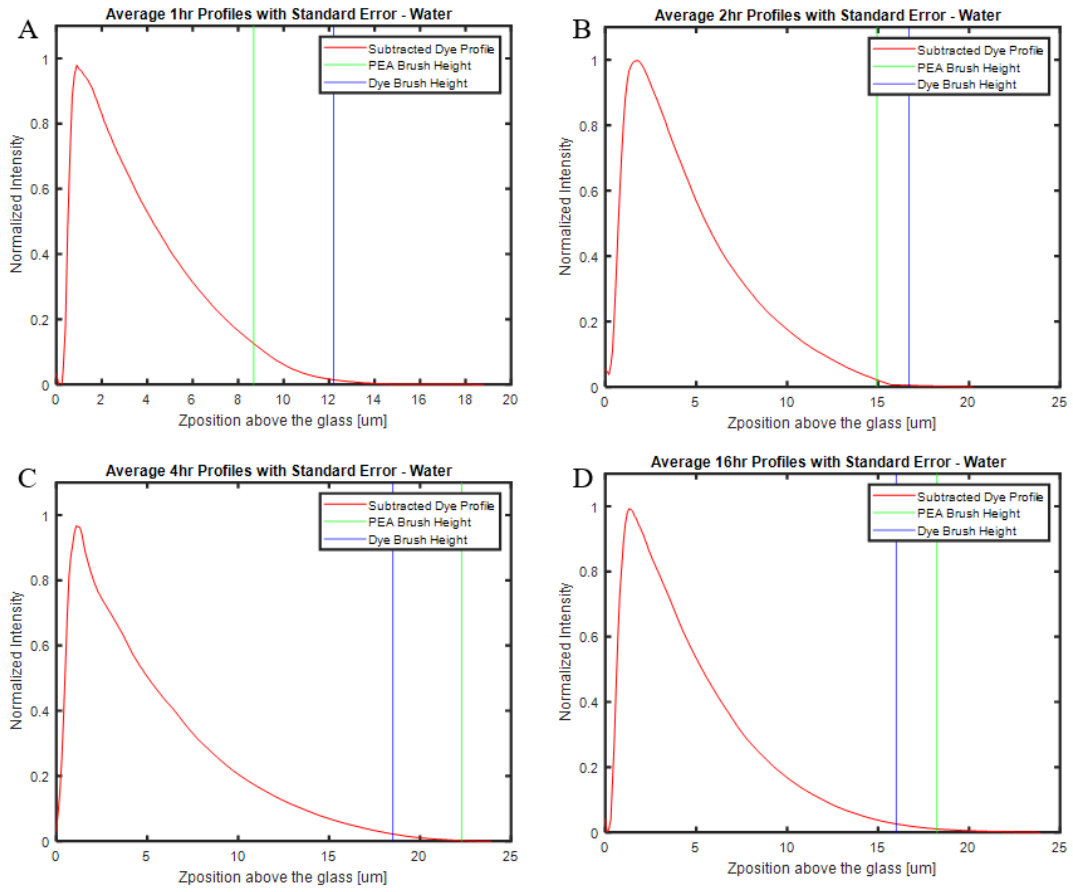

Figure 34. Fluorescent profiles (red) for 1, 2, 4, and 16 hr brushes in water where the height of the brush as determined by PEA is marked green and as determined by the dye profile background is marked in blue.

Table 5. Summary of brush heights (in microns) as determined by particle exclusion assay or dye profile assessment for 1, 2, 4, and 16 hr brushes in 150 mM NaCl (salt) and water.

	Particle Exclusion Assay		Dye	
t_{growth}	Salt	Water	Salt	Water
1	2.39	8.68	7.4	12.2
2	3.43	14.94	8	16.7
4	4.77	22.28	8.4	18.5
16	4.27	18.23	8.8	16

4.9.5 Azide "click" chemistry

"Click" chemistry, as defined by Kolb, Finn, and Sharpless in 2001, is an approach to building molecules that requires the reactions be "modular, wide in scope, give very high yields, generate only inoffensive byproducts that can be removed by nonchromatographic methods, and be stereospecific … include simple reaction conditions (ideally, the process should be insensitive to oxygen and water), readily available starting materials and reagents, the use of no solvent or a solvent that is benign (such as water) or easily removed, and simple product isolation."[121] The resulting reactions are fast and highly selective. Despite copper-mediated chemistries are the first choice in most cases[122], we chose a non-copper-mediated reaction as a first trial run as the components tend to be cheaper and the Finn lab, with whom we collaborated, had the necessary non-copper reagents immediately available.

We first had to verify that GlcNAz would be incorporated into the HA polymers via the HA synthase. Li et al suggested that a ratio of 1:9:10 GlcNAz : GlcNAc : GlcUA would result in successful incorporation[44]. Indeed, when we attempted a 1:1 ratio of GlcNAz : GlcUA, no brush was grown. When we scaled back the ratio to 1:9:10, a brush was successfully grown. The resulting brush was shorter in height (~4 μm in 150 mM NaCl, 4 hr growth) than a brush grown with non-azide monomers (~6 μm in 150 mM NaCl, 4 hr growth). This could be a result of poor HAS-HA binding due to the modified sugar or the HAS synthesis kinetics are affected by the new monomer.

Originally, the dye was donated from the Finn lab in DMSO. We maintained a DMSO environment on the brush during labeling, but each time this would result in no

brush when it came time to image. We determined that the DMSO was likely destroying the brush in a similar fashion to SDS since high concentrations of DMSO have been shown to disrupt cell membranes and might therefore disrupt our fragments.[123] Moving forward, the dye was dissolved in water (since it is also miscible in water) and all labeling was performed in water.

The Finn lab also advised that the dye should incubate with the sample at 30-37ºC for 8 hrs or even overnight. We determined that even though that might result in the most efficient environment for the dye to bind to the azide monomers, an unreinforced brush is not stable for long enough at high temperatures for enough brush to remain after the labeling is finished in order to be imaged. Therefore, reinforced brushes should be used or unreinforced brushes can be used, but should only be allowed to sit at room temperature rather than incubated at higher temperatures. Unfortunately, we found that the azide brushes (both 4 hr and 16 hr growth) do not hold up well to reinforcement. They are often completely lost or so much is lost that by the time labeling is finished, not enough remains to extract a profile. Therefore, only unreinforced brushes are used for this study until the reinforcement of azide brushes can be further troubleshooted.

Figure 35 shows the fluorescent profile from one spot measured on an unreinforced 16 hr brush that was grown with GlcNAz present and then labeled with a dye that will only interact (click!) with the azide monomers. Despite the long growth time, it can be easily seen that the brush is much shorter (~6 μm) than a typical 16 hr brush. Due to the brush being so short, it is not as immediately obvious that there is dye present when comparing

to a brush labeled with carbodiimide chemistry. As evidenced by B, there is clearly dye present within the brush, indicating that azide monomers were successfully incorporated.

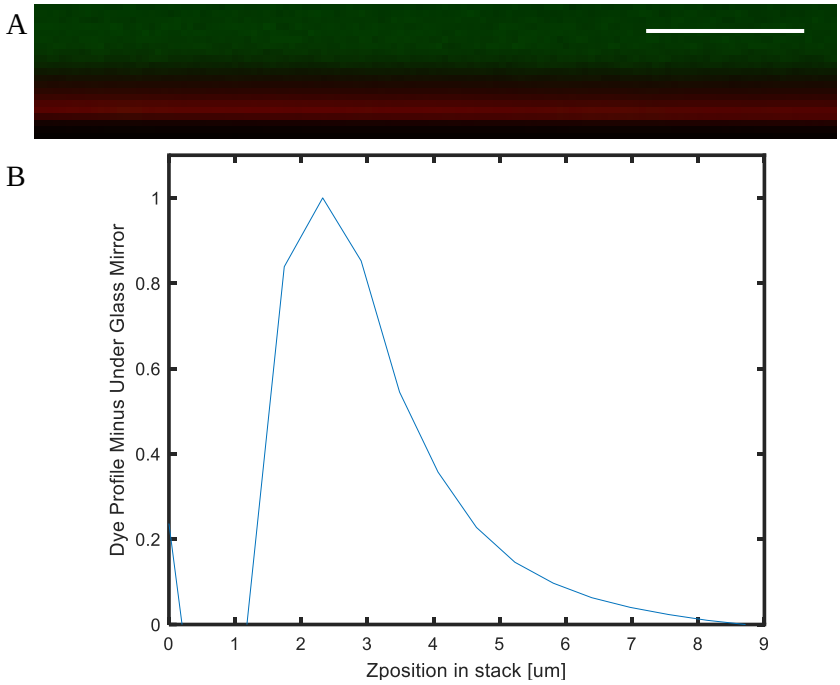

Figure 35. A) XZ average side view of fluorescently labeled, unreinforced, 16 hr brush. Dye (red) and 200 nm excluded nanoparticles (green). Scale bar is 10 µm. B) 'Mirror subtracted' fluorescent profile.

Further work must be done to optimize the labeling. Achieving thicker brushes would make the profile much clearer and more obvious to the naked eye. It is difficult to know if growing the brushes for longer would result in thicker brushes. Normal brush growth levels off around 16 hrs, but it is very likely that a growth curve representing azide-incorporated brushes would be different and therefore the maximum achievable brush height for these new brushes would be different.

The aging and loss of brush height due to incubation at high temperatures for long periods could be addressed with a swap to a copper-mediated clickable fluorophore. Now

that we have demonstrated that the azide monomer is being incorporated into the HA brush, we can proceed with the more reliable click-labeling method. A copper-mediated reaction will be much faster which would preserve more brush between growth and imaging. It might also result in brighter profiles as it would be a more efficient reaction.

Azide monomer incorporation into a synthesized HA polymer will allow for a wide variety of future studies, in addition to the fluorescent labeling of the brush polymers. The charge along the HA backbone could be modified by clicking in a positively charged species or more negatively charged species. The brush could be crosslinked to create a stiff brush interface or to modify the pore size of the brush to adjust nanoparticle or flow penetration. Experimentally extracting the polymer concentration profile and molecular weight distribution, especially for a polydisperse brush, was important to de Vos and Leermakers who said, "We believe that the question of the distribution function will become more relevant when good experiments on the effects of polydispersity become available, and can be compared to the model results."[67] The HA brush system is perfectly poised to do just that.

CHAPTER 5. TOPOGRAPHY

Parts of the following chapter have been previously published:

Sculpting Enzyme-Generated Giant Polymer Brushes. Jessica L. Faubel, Wenbin Wei, and Jennifer E. Curtis. *ACS Nano* **Article ASAP**. DOI: 10.1021/acsnano.0c06882

5.1 Patterning

Three-dimensional nanostructured polymer brushes are finding increasing applications in materials science, chemistry, and the biosciences.[124-129] Polymer brush gradients and other topographies have been used in combinatorial studies of a broad range of physiochemical phenomena,[130-135] enable the directed transport of soft materials like nanoparticles and cells,[136, 137] facilitate the screening of design strategies for protein and cell-substrate interactions,[138, 139] and are useful tools in expediently exploring the fundamental behavior of the brushes.[128, 132, 133, 140] Sculpted brushes can also be used to tune the local environment (*e.g.* porosity, stiffness, roughness)[134, 141] or orchestrate the organization of complex materials such as structured nanoparticle-polymer film composites.[142-144]

5.1.1 General patterning methods

Various strategies exist to sculpt polymer brushes, typically by spatially varying the grafting density [145-149] or the molecular weight.[131, 150-152] Generally, brush topography can be programmed through controlled placement of the polymer initiators *via* lithographic techniques or the availability of monomers.[59, 153-156] Another strategy

involves varying the feature density - the spacing of discrete, constant density nanobrushes - in order to achieve impressively complex architectures.[157] One commonality of all these examples, however, is that the sculpted brushes are almost always less than a few hundred nanometers thick.

Ultrathick three-dimensional polymer brushes present many advantages especially in domains where brush gradients or more complex topography are desirable. Micron-sized brushes provide a larger dynamic range for height manipulation and associated properties like porosity and stiffness. The increased degree of polymerization inherently provides more volume for uptake of molecules and a greater number of binding sites to bind, organize, or sort molecules and particles, for example in separations applications.[158, 159] For applications dependent on non-linear topographies, larger brushes offer a thicker template on which to execute complex patterns. Microns-thick polymer brushes also have the unusual advantage of being directly characterizable using optical microscopy (Figure 8B, C), potentially diversifying design possibilities and read out for various applications.

However, sculpting the giant brush by spatially modifying the grafting density or varying the molecular weight is non-trivial. This is because in order to harness the impressive capabilities of HA synthase, we must stabilize this lipid-dependent transmembrane protein in its natural membrane environment.[99] This is achieved by collecting fragments of membrane from bacteria which have been genetically-manipulated to overexpress the HA synthase enzyme. The membrane fragments contain dense configurations of active HA synthase. HA brushes are then fabricated by decorating a substrate with the membrane fragments and initiating polymerization by providing the prerequisite sugar monomers (Figure 1a). This explains why traditional lithographic

patterning of grafting density is difficult, as the grafting density is governed by the HA synthase expression levels in the bacterial membrane fragments.

5.1.2 Chapter outlook

In this chapter, we investigate whether visible light can be used to alter HA synthase function and hence modify the underlying grafting density of the enzyme-generated brushes for the controlled sculpting of structured three-dimensional brushes. Simple experiments establish that quantitative changes in brush height can be achieved by varying laser intensity, exposure time or wavelength. We demonstrate how this insight enables brush sculpting by creating an ultrathick linear brush gradient with a height increase of 90 nanometers per micron from 0 to six microns. We then delve into determining the mechanism of the brush height patterning by implementing a series of experiments based on our understanding of how visible light interacts with hyaluronan, lipids, and proteins. Integrating the knowledge gained by comparing patterning results before and after brush growth and in the presence and absence of bacterial membrane fragments, we provide strong evidence that reactive oxygen species (ROS), generated by light-membrane fragment interactions, are the agent by which HA synthase function is destroyed.

5.1.3 Prepatterning

We explored the potential for photopatterning the HA brush with a 405 nm laser motivated by the idea that near UV or blue light might damage proteins and thus provide a way to manipulate the HA synthase and hence the brush's grafting density. Testing this hypothesis with a laser scanning confocal microscope was straightforward because it inherently enables photo-micropatterning, variation of intensity, exposure time, and

wavelength. We started by prepatterning the HA synthase substrates with no brush (Figure 36A). The confocal's 405 nm laser was focused on the surface and raster scanned in a selected region at fixed power. Upon completion of the laser application, HA synthesis was switched on by adding the two required uridine diphosphate (UDP)-sugar monomers and then the brush growth was allowed to proceed for t_{growth} =16 hrs (Figure 36B). Experimentation established that regions exposed to at least ~200 μJ/μm^2 lose the capacity to generate a polymer brush (see Materials and Methods). This energy density was achieved by scanning each patterned area five consecutive times at 200 μs/pixel at the desired laser intensity, which could be varied from 0 to 100% ($P_{405,max}$ = 561 μW).

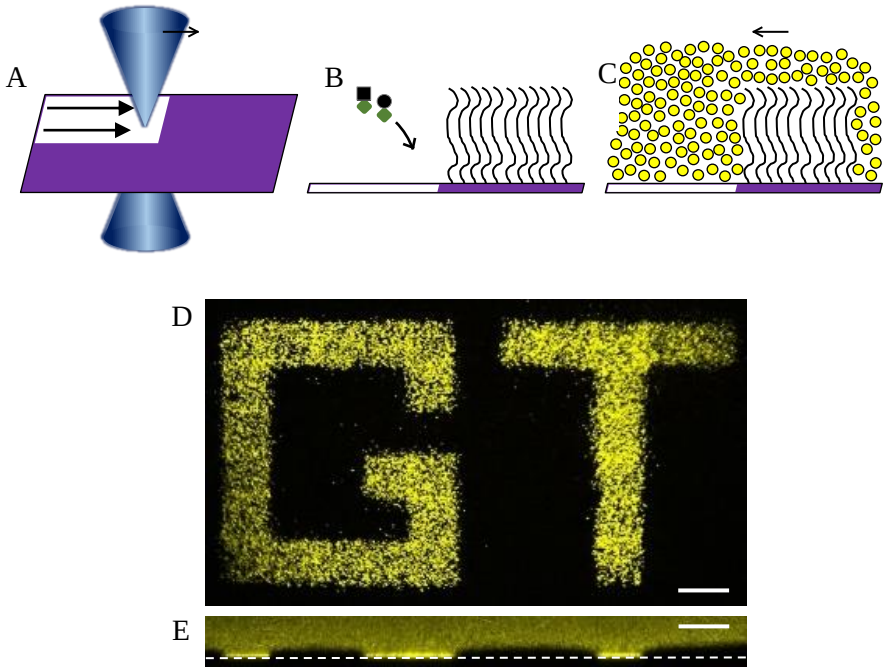

Figure 36. A) Schematic of laser treatment of the enzyme-rich (purple) surface. White areas indicate photo-treated areas. B) After photopatterning, components necessary for enzymatic synthesis of the HA are added and HA is generated in unirradiated regions. C) Fluorescent 200 nm particles are excluded from areas with brush present and allowed to fill in gaps where brush is absent which allows for visualization of the pattern. D) Binary patterning in the form of a GT (*i.e.* Georgia Institute of Technology). Top down (XY) confocal microscope view at the glass interface. 200 nm beads (false colored yellow) appear in areas without brush. Black regions are where brush is present. t_{growth} = 16 hrs. E) Side (XZ) confocal microscope view across the middle of the top image, as indicated by the black arrows. The glass interface is labeled with a white dotted line. Scale bars are 20 µm.

The resulting patterns are readily visualized with the same confocal microscope by implementation of a particle exclusion assay (Figure 36C).[86, 92] As demonstrated in previous work,[22] fluorescent nanoparticles of 200 nm are sterically hindered from penetrating the HA brush and thus serve as a means of outlining a brush's upper interface. Figure 36D, E demonstrates the binary patterning of the brush in a ~200 µm x 100 µm area.

In this XY view taken at the glass substrate, the 200 nm yellow nanoparticles appear in areas where the 405 nm laser was applied. The laser exposure fully disrupts the HA synthase function as evidenced by the lack of brush growth. In the untreated sample areas, the brush grew normally, excluding the 200 nm particles.

5.1.4 Intermediate brush heights

Next, we explored whether the brush could be tuned to reach intermediate heights with reduced exposures to the 405 nm laser. In a 4x3 array, twelve different laser intensities were applied for the same exposure time to square areas (17.4 x 17.4 μm^2). Then, the brush was grown for 16 hrs and the height in each patterned region was analyzed. Results from three such experiments are summarized in Figure 37. Figure 37a shows the XY view at the glass interface with regions of increasing energy density (left to right, top to bottom). The subsequent decreases in the thickness of the brush is visualized by the increasing amounts of the 200 nm red fluorescent beads present at the glass interface and by the decreasing gap present between the black glass interface and the red nanoparticles in the XZ side views in Figure 37b. The energy densities necessary to achieve a range of final brush heights (0-8 microns, t_{growth}=16 hr) is plotted for constant exposure time (405 nm, 5 scans at 200 μs/pixel) and variable laser intensity in Figure 37c.

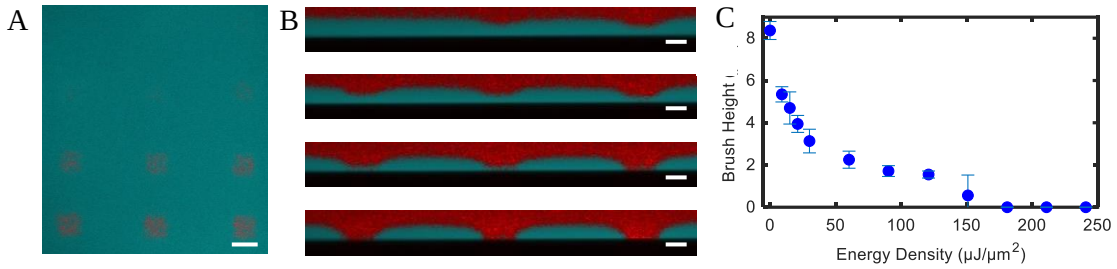

Figure 37. A) XY confocal image of square patterned areas with increasing laser energy density applied, viewed at the surface. Red fluorescent 200 nm particles are sit closer and closer to the surface in areas treated with higher energy densities. Cyan colored dextran highlights regions where brush is present. Scale bar is 20 μm. B) Average intensity XZ side views of each row corresponding with the image in (a). Black is the glass substrate. Scale bars are 10 μm. C) Energy density of the applied laser *versus* the resulting height of brushes grown for 16 hrs. N = 3 brushes. λ = 405 nm.

Notably, distinct brush curvature in the evenly patterned areas likely arises from polymer splay at the edges of the patterned area.[160, 161] The effect is increasingly pronounced in the areas where the brush height is reduced so that more free space is available for the surrounding brush spill over and distort the brush profile. In the future, we will systematically investigate these effects, as they are fundamentally interesting and they will clearly impact any sophisticated sculpting of the brush topography.[161]

5.1.5 Gradient

With fine-tuned photo-manipulation of the brush height established, one can create more complex brush topographies. To explore this, we designed a brush gradient with a height that linearly increases six-fold over an extent of ~56 microns (Figure 38). At its highest point, the brush height is 5.8 μm. To create this gradient, the data from Figure 37C was used to determine the necessary energy densities to realize height decreases in half-micron steps. Small rectangular areas (6.25 μm x 20 μm) were irradiated in nine adjacent

regions, as outlined with dashed lines in Figure 38A. After this prepatterning treatment, the brush was grown for 4 hours. The resultant brush heights in Figure 38C show that the height decreases in a linear fashion by approximately one half-micron (~590 nm) per 6.25 μm region, corresponding to a ~90 nm change in brush height per lateral micron. Although the patterning is discrete, the final brush appears as a continuous gradient (Figure 38B) – an effect resulting from the significant splay arising in thick polymer brushes.

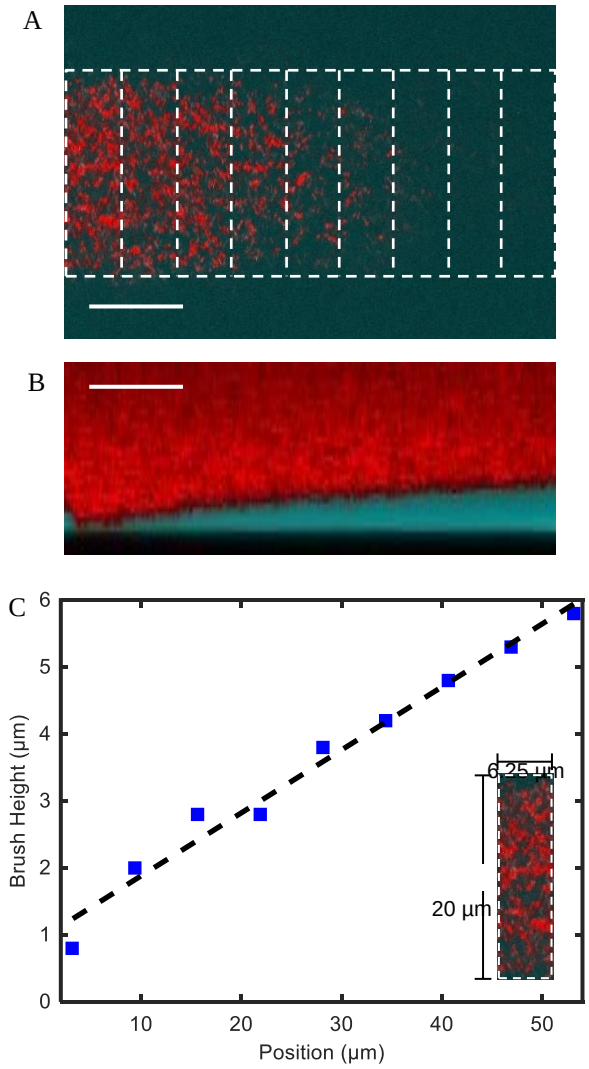

Figure 38. A) XY view at the glass substrate under the brush. The white outlined areas depict the nine regions patterned at pre-selected energy densities. The brush thickness increases linearly in height to the right. B) Side view of the linear brush gradient. The maximum height is 5.8 μm. All scale bars are 10 μm. C) Average height of the brush in each patterned region. N = 1 brush. λ = 405 nm, t_{growth}= 4 hr. Black dotted line is a linear fit, H = 0.94 + 0.09x, where x is in microns.

5.1.6 Postpatterning

Polymer brush patterning schemes are typically limited to either prepatterning or postpatterning (before or after brush growth) and most are incapable of doing both,

especially using the same method. In Figure 39, we illustrate the capacity to implement both approaches on one sample. This capability was expected since photo-disruption of the HA synthase is the hypothesized mechanism, but an unforeseen outcome was the nearly overlapping brush heights after pre- and postpatterning at the same energy densities. Below, we will use this result to shed insight on the mechanism behind the brush height photopatterning and use it to address the possible connection to grafting density.

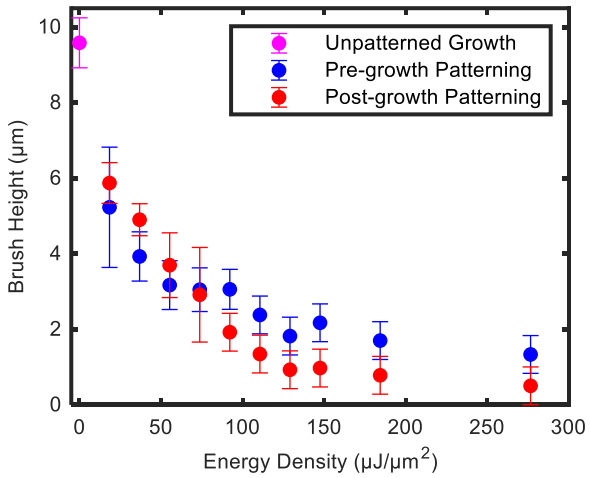

Figure 39. Brush height *versus* energy density. λ = 405 nm. Purple is unpatterned growth, N = 3 brushes. Blue is pre-growth patterning, N = 3 brushes. Red is post-growth patterning, N = 1 brush.

5.1.7 Multiwavelength patterning capabilities

To investigate the mechanism of the photopatterning and to potentially expand the methodology's flexibility, we examined whether longer wavelengths also enable manipulation of brush height. Similar results can be achieved using λ = 488 nm and λ = 635 nm (Figure 40). The efficiency of the patterning is reduced with increasing wavelength, however, requiring higher energy densities. Due to the efficiency of patterning with the 405 nm laser, very little exposure time was required to pattern. Therefore, the only way to achieve a spread of energy densities was to vary the intensity of the laser from 0 to 100% with a set exposure time. With longer wavelengths, exposure time necessary to eliminate the brush increased significantly. In Figure 40, 488 nm and 635 nm data represents varied exposure time, rather than varied laser intensity as with the 405 nm.

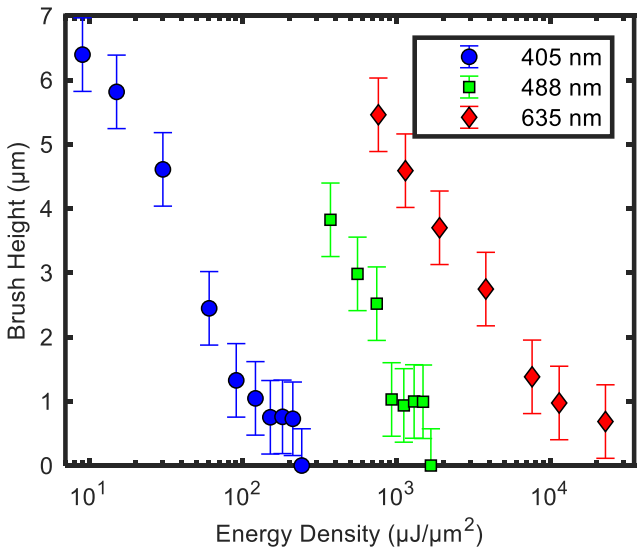

Figure 40. Energy density of the applied laser *versus* the resulting brush height. Blue: t_{growth} = 16 hrs. λ = 405 nm. N = 3 brushes. Green: t_{growth} = 16 hrs. λ = 488 nm. N = 1 brush. Red: t_{growth} = 16 hrs. λ = 635 nm. N = 1 brush.

5.1.8 Patterning reinforced brushes

Future applications of the HA brushes will likely adopt a chemically stabilized version of the brush because they are more amenable to long-term usage. Indeed, the HA brushes studied thus far are inherently unstable, decaying over a few days due to the release of HA from the HA synthase.[22] To resolve this issue, we previously established that robust chemical attachment to the underlying substrate can be achieved using carbodiimide chemistry to generate an amide bond between the HA's available carboxyl groups and the amines present on the surface due to the polyethyleneimine (PEI) film used in the scheme for fragment attachment.[22]

For these chemically-stabilized 'reinforced' brushes, the grafting density is independent of viable HA synthase, unlike for the 'unreinforced' brushes where the HA synthase must both make and anchor the HA. The reinforced brush's independence from HA synthase was previously established by using the surfactant, sodium dodecyl sulfate (SDS), which we applied to remove the bacterial membrane fragments. Elimination of the membrane fragments destroyed unreinforced brushes as expected; reinforced brushes remained unchanged.[22] Hence, in the reinforced brush case, the loss of stability or activity in HA synthase due to photopatterning should not affect the final brush height.

Yet, despite this seemingly well-founded prediction, we found that photopatterning the reinforced brushes also enables manipulation of the brush height. Figure 41a, b shows a brush that was grown for 4 hours, reinforced, and then successfully patterned with the same exposure settings previously determined to result in no brush growth in a prepatterning scheme. This unexpected result may in fact be the most useful

implementation of the patterning method since it is demonstrated to work on stabilized, ultrathick, HA brushes. Such brushes are ideal for applications and combining their stability with access to postpatterning enables their fabrication, storage, and future patterning as needed.

5.1.9 Investigating the influence and origin of ROS

To further investigate the mechanism behind the HA brush sculpting, we designed a simple experiment to investigate whether ROS, generated by photo-interactions with the samples, might be involved. It is well-known that UV-irradiation can directly denature enzymes,[162] but our patterning scheme works well into the visible spectrum. Proteins cannot be damaged by visible light unless they contain side groups that are capable of absorbing those wavelengths, like flavins in flavoproteins.[163] However, visible light can indirectly damage proteins through the production of ROS resulting from the light's interaction with cellular components. The resulting ROS can, in turn, cleave peptide bonds[163-165] as well as drive lipid peroxidation.[166-168]

We increased levels of the antioxidant dithiothreitol (DTT) to sequester ROS and block its presumed role in brush patterning.[169, 170] The results are revealing (Figure 41c, d). Increasing DTT significantly (50 mM) reduces the patterning efficacy, such that under conditions that would normally prevent brush growth in standard growth buffer (w/5 mM DTT) (Figure 41c), a substantial brush is still able to grow (Figure 6d). We then verified that for reinforced brushes, high DTT (50 mM) also significantly reduces the photopatterning efficacy (Figure 41e). Together these results confirm that ROS plays a crucial role in the photo-patterning mechanism.

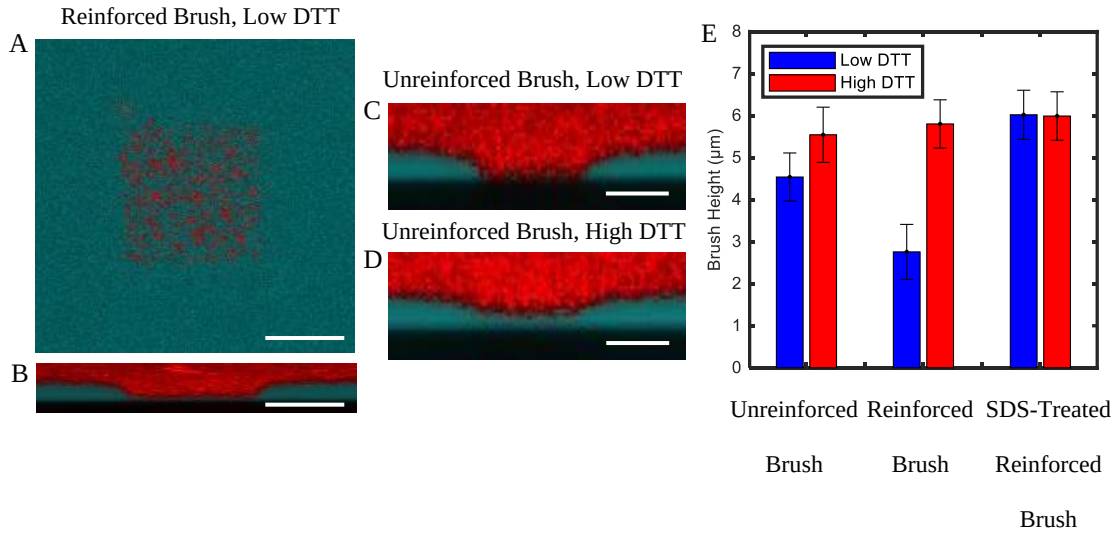

Figure 41. A) A 4 hr growth *reinforced* brush with a square patterned region at the center. B) XZ average side view confirms brush elimination in patterned region. C) 5 mM DTT. Average XZ side view of a post-patterned 4 hr brush shows full brush removal. D) 50 mM DTT. Increased DTT significantly reduces the photopatterning efficacy. All scale bars are 10 μm. E) Height of different brush types *versus* DTT concentration after postpatterning. N = 3 brushes per type, t_{growth} = 4 hr. λ = 405 nm, ~280 μJ/μm^2.

Although some ROS species have been shown to degrade HA,[171, 172] the agreement between pre- and postpatterning results (Figure 39) indicates that direct ROS degradation of HA during postpatterning is not a dominating mechanism behind change in brush height. Additionally, HA has been shown to not absorb visible light wavelengths so it is unlikely that HA-light interactions play a role.[173, 174] We therefore hypothesize that during prepatterning and postpatterning of *unreinforced brushes*, the ROS directly interacts with HA synthase through cleavage of peptide bonds and/or with the surrounding lipids, destabilizing the local membrane and disrupting the transmembrane HA synthase.[99] As HA synthase enzyme structures are destabilized, their function can be lost, decreasing the fraction of active enzymes on the surface able to produce and/or stably anchor HA. The agreement between pre- and postpatterning (Figure 39) strongly supports

the conclusion that the enzyme activity is destroyed rather than altered. We can thus draw a particularly important conclusion: photopatterning HA synthase-generated HA brushes with visible light enables the local tuning of the grafting density of the HA brush for both pre-patterned and post-patterned unreinforced brushes *via* ROS destruction of HA synthase function.

What is the origin of the ROS? Since we have established that the photopatterning works even in the absence of HA (during prepatterning), we therefore hypothesized that the ROS originates from light-surface interactions rather than light-HA interactions. ROS generated from light-surface interactions could arise from either photochemistry with molecules in the protein and lipid-rich membrane fragments; or from reactions with the underlying polyethyleneimine-glutaraldehyde (PEI-GA) film used to bind the fragments to the substrate. To distinguish between these two possibilities, we attempted to pattern reinforced brushes with a reduced fragment presence through treatment with SDS to remove the membrane fragments.[22] The patterning failed at high and low concentrations (see Figure 41e), with the initial brush height remaining unchanged at both DTT concentrations. This provides compelling evidence that light interactions with the membrane fragments are the likely source of ROS production. It also provides further evidence that photon-HA interactions and photon-PEI/GA interactions are not significant enough to detectably alter brush height.

The last puzzle in this story is the mechanism of the postpatterning of reinforced brushes. We have established that HA synthase plays no final role in these brushes; the membrane fragments are necessary to generate ROS and for patterning to work; and that ROS interactions with HA polymers are negligible. This led us to consider the vulnerability

of the HA linkages (amide bonds) to the underlying substrate. We hypothesize that just like the peptide bonds in HA synthase, which are in fact a type of amide bond between amino acids, these amide bonds are disrupted by the ROS, which damages the HA anchoring to the surface. As these bonds are broken, the HA strands are lost from the brush and the height decreases.

5.1.10 Summary

Table 6 summarizes the insights collected from integrating the results from the three photo-patterning strategies used here on unreinforced (pre-/post-) and reinforced brushes (postpatterning). Overall, the strategy to use visible light, in particular 405 nm, is effective in locally tuning brush height, creating sculpted topographies, and is amenable to different types of patterning and brushes. Using longer wavelengths is also possible, but requires higher energy densities (higher power and/or more exposure time) to achieve the same patterning results. In our lab, the maximum power available for the green and red lasers on the confocal microscope made patterning prohibitively time consuming; however stronger light sources would circumvent this limitation.

Table 6. Summary of the patterning mechanism for each brush type and the evidence from each type of experiment that supports these conclusions.

Summary of Patterning Mechanism by Brush Type			
Brush Type	**Does it pattern?**	**Patterning Mechanism**	**Evidence and Conclusions**
Unreinforced (Pre-patterning)	Yes	HA synthase function disrupted by ROS	Conclusion: • Patterning mechanism must be independent of HA.
Unreinforced (Post-patterning)	Yes	HA synthase function disrupted by ROS	Evidence: • Similar results from pre- and post-patterning suggest same mechanism. Conclusions: • HA-light interactions are minimal. • HA-ROS interactions are minimal.
Reinforced	Yes	HA-PEI amide bonds cleaved by ROS	Evidence: • Amide bonds are susceptible to ROS.
SDS-Treated Reinforced	No	None	Conclusions: • ROS are generated from fragments. • HA-light interactions are minimal. • PEI/GA-light interactions are minimal.

5.1.11 Future work

Expanding to mask-dependent photopatterning will facilitate rapid tailoring of the polymer brushes on much larger scales. Access to larger patterned areas will also enable atomic force microscope measurements of dry brush height in order to verify our conclusion that photopatterning of the brush topography results from direct manipulation of the HA grafting density. Future studies comparing theoretical predictions of the shape and concentration profiles of patterned polymer brushes with the very evident splay observed in these studies (Figure 37b) are of interest and moreover, will be crucial to help develop design rules for integrating expected splay into engineered brush topographies.

Although the method is currently limited to enzyme-fabricated HA brushes, the biopolymer can be post-modified to manipulate its chemical identity for diversification of its scope of applications. [175-177] Ultimately, the ROS–photopatterning method introduced here might be extended to a growing class of enzyme-derived polymer brushes and films, which already include DNA[21] and polyhydroxyalkanoate (PHA)[20] materials made by the enzymes deoxynucleotidyl transferase and PHA synthase, and may include future materials made by untapped enzymes such as cellulose synthase.[178]

5.2 Splay

During patterning experiments, it became increasingly evident that the patterned areas did not have perfectly vertical polymer walls at the edges of the region, but rather a slow, non-linear increase in height out to an equilibrium brush height. This can be clearly seen in Figure 37b. To determine if this was an effect of ROS diffusion or a physical effect

due to polymers splaying or spilling into the empty space, we grew a brush for 16 hrs, reinforced it, and used a razor blade to put a scratch through it. (Figure 42)

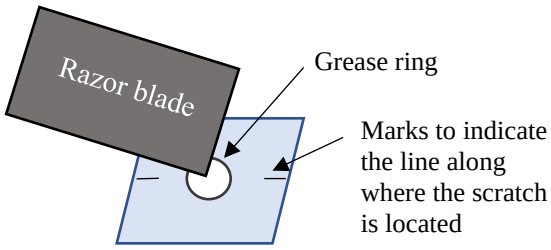

Figure 42. Schematic representation of how the brush is scratched by a razor blade.

Figure 43 shows that the same splay can be seen when the only change has been mechanical (a scratch), rather than chemical (ROS). Since there is a gap present, the HA bordering the scratch is not sterically forced perpendicular to the glass, but can rather spread (or splay) into the empty space created by the scratch. Interestingly, when the salinity is dropped to zero and the brush gets taller, the width of the gap of the gash decreases from ~16 μm (yellow line in Figure 43A, B) to ~14 μm (yellow line Figure 43 D, E). The decrease in apparent gash width from salt solution to water is representative of the spillover of polymers further into the gap due to HA extension in water and increased steric hinderance from hydrated neighbors. This splaying effect remained relatively local when in salt, only extending about 9 μm to either side of the scratch. Whereas in water, this effect extends out 25 μm to either side.

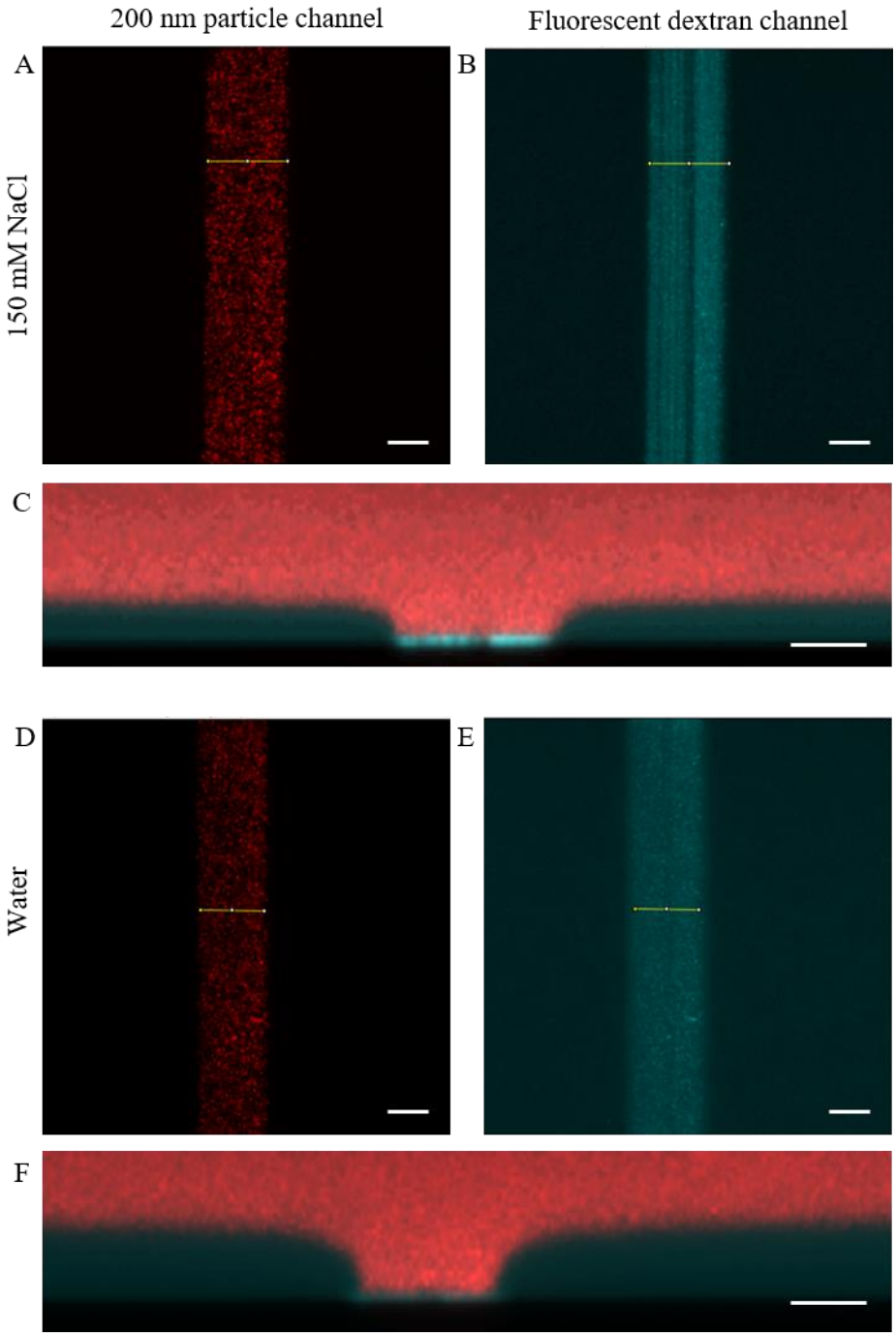

Figure 43. 16 hr, reinforced and scratched brush in 150 mM NaCl and water. 150 mM NaCl: A) Top down view of scratch. Only 200 nm red nanoparticles are present inside the scratch. Yellow line width = ~16 um. B) Top down view of scratch. Fluorescent dextran penetrates both the brush and the scratch. More dextran appears to stick inside the scratch, highlighting it. Yellow line width = ~16 um. C) XZ average side view of the scratch. Water: A) Top down view of scratch. Only 200 nm red nanoparticles are present inside the scratch. Yellow line width = ~14 um. B) Top down

view of scratch. Fluorescent dextran penetrates both the brush and the scratch. More dextran appears to stick inside the scratch, highlighting it. Yellow line width = ~14 um. C) XZ average side view of the scratch.

If the same experiment is repeated on a 4 hr, unreinforced brush in salt solution, the extent of polymer splay becomes significantly farther reaching. In Figure 44, it appears that the splay affects the brush height ~100 μm away from the scratch area, two orders of magnitude further than in the taller, reinforced brush case. In a reinforced brush, polymers can rearrange within the brush, but they cannot be expelled from the brush due to forces experienced during this rearrangement nor due to decreased steric hinderance from one side. In the unreinforced brush case, it is possible to lose polymers due to brush disturbances both from shear and polymer rearrangements and equilibration. This loss due to brush disturbances could propagate until they are negligible where the brush height equilibrates. It is feasible that this is a one-off result and duplicate scratch tests should be performed in both cases.

Figure 44. XZ average side view of a 4hr, unreinforced and scratched brush in 150 mM NaCl. Scale bar is 20 μm.

Nonetheless, this series of experiments demonstrates that the splay of polymers and curvature of the brush topography in the area around a gap or brush void is more likely a mechanical effect than chemical. Further work, ideally paired with simulation, could model this polymer splay and determine if there is a curvature dependence or scaling on brush height. Predictability in the curvature along with the patterning methodology would lead to fine-tuned topographical control.

CHAPTER 6. RESPONSE TO STIMULUS

The following chapter has been previously published:

Giant Hyaluronan Polymer Brushes Display Polyelectrolyte Brush Polymer Physics Behavior. Jessica L. Faubel, Riddhi P. Patel, Wenbin Wei, Jennifer E. Curtis, and Blair K. Brettmann. *ACS Macro Letters* **2019** *8* (10), 1323-1327. DOI: 10.1021/acsmacrolett.9b00530

6.1 Reversibility of response to salt

Hyaluronan is a weak polyelectrolyte and therefore sensitive to ionic strength and changes in pH. Figure 45A, B illustrates the stimulus responsiveness and reversibility of the HA brushes to changes in ionic strength. The planar brushes nearly double in height upon reduction of the ionic strength from 130 mM to 1.3 mM. For brushes grown for 16 h, the height increases from 12.1 ± 0.2 μm to 22.2 ± 2.5 μm (± is st. dev.), and it can be reversibly collapsed and stretched by exchange of the solvent, as shown in Figure 3. Similar results were found for brushes grown for 4 h which increase more than 200% from ~7 μm to ~15 μm (Figure 45C, D). In both cases, there is a small decrease in height with each solvent exchange, with more HA loss from the inherently thicker brushes.

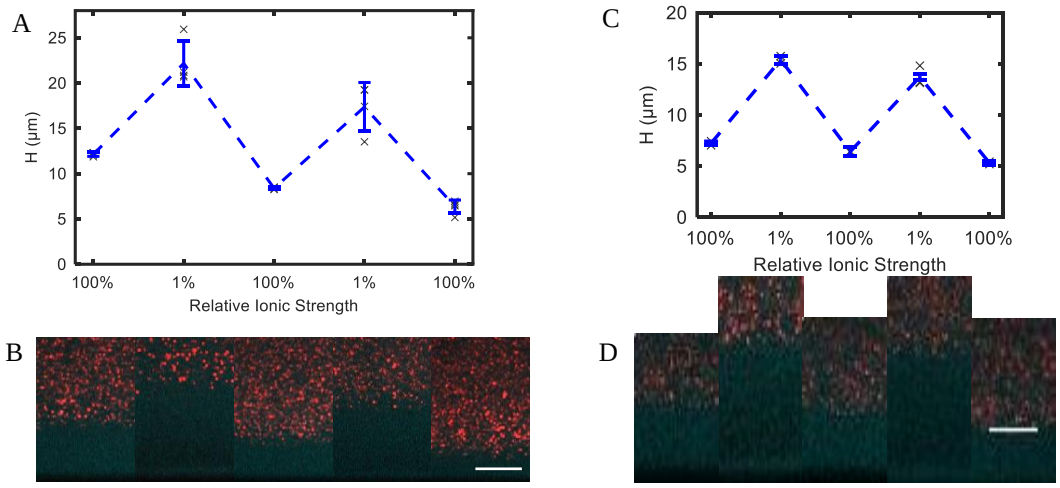

Figure 45. A) Brush height during a series of solvent swaps from 133 mM to 1.33 mM for a brush previously grown for 16 h. B) Quantification of the brush height shows that at ultra-low ionic strengths, the brush stretches out by nearly 200%, peaking at 22.0 ± 2.5 μm (st. dev.) during the first exchange. While the brush swelling and shrinking is reversible, the repeated handling (and tension induced by stretching) leads to some loss of the HA, which is weakly bound to the HA synthase. As a consequence, a gradual decrease in the overall brush height is observed. Each grey data point corresponds to five independent measurements (211 x 211 μm^2 area) from one sample. Blue data points show the mean and st. dev. C) Height measurements from (D) for 5 regions of a brush grown for 4 h reported by grey x's (region area was 211 x 211 μm^2). The blue shows mean and st. dev of the measurements on the same brush. D) XZ profile of a HA brush's stimulus responsiveness and reversibility to ionic strength swapping; switching from 100% to 1% dilution of the imaging buffer with deionized water. In contrast to the extreme example displayed in A and B, this shorter brush stretches only to ~15 μm (from ~7 μm) rather than 22 μm; but it also is more reversible, losing less height with each solvent swap. All scale bars 10 μm.

6.2 Osmotic and salted brush regime

A key characteristic of a polyelectrolyte brush is its response to solution ionic strength. At low ionic strengths, the brush is in the osmotic regime, where the large osmotic pressure difference between the counterions in the brush and the bulk solution causes strong stretching of the chains and the brush height is constant with concentration. At

higher salt concentrations, the brush enters the salted regime, where there is a power law dependence between brush height and ionic strength with an exponent of -1/3 due to the release of counterions that are localized in the brush in the osmotic regime, leading to the reduction in the osmotic pressure difference between the bulk and the brush. This exponent results from the balance of counterion osmotic pressure with Gaussian elasticity and neglects the excluded volume effect and finite chain extensibility. Finally, at very high salt concentrations, the brush behaves similarly to a neutral brush and the brush height is no longer a function of salt concentration.[3, 27, 179] To determine whether the HA brushes prepared through enzyme-mediated growth behave similarly to traditional polyelectrolyte brushes, we analyze their response to salt concentration in the context of the expected theoretical behavior.

The height of the brush as a function of $NaNO_3$ concentration was measured for HA brushes prepared through enzyme-mediated growth (Figure 46A). Brush height is measured directly with confocal visualization of excluded 200 nm nanoparticles as validated in (Figure 46B). Previous work showed that without further reinforcement, the brush can be damaged by rinsing. To stabilize the brush after growth, the sample is treated with EDC/NHS chemistry to generate covalent binding between carboxyl side groups on the HA and secondary amine groups on the underlying substrate. This binding results in reinforced brushes that are stable long-term and resistant to shear induced brush height losses due to solvent exchanges. All experiments with the reinforced brush were performed

on the same brush and the brush height as a function of $NaNO_3$ concentration is shown in Figure 46A.

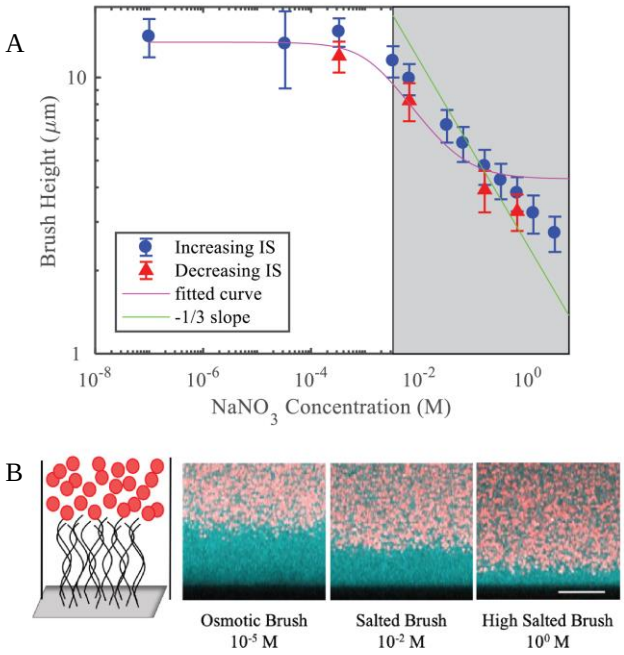

Figure 46. A) Brush height as a function of $NaNO_3$ concentration for a reinforced HA brush prepared through enzyme-mediated growth (4 hr growth time). Each data point represents at least 4 locations sampled on the brush. The lowest data point in the increasing ionic strength data is ultrapure water, assumed to have an ionic strength equivalent to 10^{-7} M $NaNO_3$ from H+ ions. B) XZ confocal microscope images of the brush cross section at 10^{-5}, 10^{-2}, and 10^{0} M. Cyan coloring is fluorescent dextran (R_g ~ 4 nm) that penetrates the brush, effectively highlighting the brush, and red coloring is the excluded large beads. The substrate is black. Scale bar is 10 μm.

The reinforced brush exhibits the first two stages of polyelectrolyte brush behavior as the salt concentration is increased. At low salt concentrations, the brush height is constant at approximately 14 μm. At a $NaNO_3$ concentration of 0.003 M, the brush enters the salted brush regime and the height decreases with concentration with an apparent power law exponent of -0.210 ± 0.004. The neutral regime may have been reached at approximately 1 M, as the decrease in brush height as a function of concentration

decreased, but we were unable to test at a sufficiently high salt concentration to verify due to the aggregation of the excluded beads at high salt concentrations. The brush regimes can also be clearly seen in the images in Figure 46B, where the cyan area is the brush, the red is the excluded beads and the black is the substrate. The brush is most extended in the osmotic regime, while it is least extended late in the salted brush regime.

The exponent for the power law dependence of height on salt concentration was shown experimentally to be -0.210 ± 0.004, lower than the theoretically predicted -1/3 slope. In the simple model that predicts the -1/3 exponent, the intrinsic excluded volume and finite chain extensibility were neglected.[179] Chen *et al*. developed a Flory-type mean-field model that takes into account these additional factors by defining the system as a balance of three pressures:

$$\pi_{cb} + \pi_{el} + \pi_{ev} = 0 \qquad 13$$

where π_{cb} is the osmotic pressure of mobile ions, π_{el} is the elastic pressure and π_{ev} is the pressure due to excluded volume.[180] Using the model described Chen et al. with a fit parameter of A = 5, we calculated a theoretical curve for brush height vs. salt concentration that accounts for excluded volume and chain extensibility (full model details in Chen et al. and Section 6.2.1). A comparison of this curve to our experimental data in Figure 46A shows that this model is a better representation of the HA brush response to salt than the -1/3 power law exponent. This is also consistent with a study on a smaller 'grafted to' HA brush (~ 2.5 microns), which showed that the experimental data fit well to a similar model where the excluded volume and finite extensibility were accounted for.[64] One distinction between the previous work on HA brushes and our work is that of polydispersity. The

previous work focused on monodisperse brushes, whereas the brushes used in this work are distinctly polydisperse which could also contribute to the deviation of the model from the experimental data at the highest salt concentrations. Despite their extra-large size, the brushes prepared through enzyme-mediated growth behave similarly to smaller brushes prepared via a grafting to approach.

6.2.1 Model for brush height with excluded volume and finite chain extensibility

The theoretical model used to predict brush height as a function of salt concentration was first reported in Chen *et al.* and is based on a balance of pressures as described in Equation 13. Details in Chen *et al.*, but we briefly explain here. Two simplifying quantities are defined: 1) The stretching ratio:

$$r = \frac{H}{aN} \tag{14}$$

where H is the brush height, a is the monomer size and N is the contour length. A quantity, y:

$$y = \frac{2C_s ar}{f\sigma} \tag{15}$$

where C_s is the salt concentration, f is the charge fraction of the polymer and σ is the grafting density.

Using a charge balance with Donnan equilibrium for π_{cb}, the free energy of a freely jointed chain considering the finite extensibility of the chain for π_{el}, and a mean-field approximation for the excluded volume interactions, the pressure balance becomes:

$$Afr\left[\sqrt{1+y^2}-y\right] - r^3\frac{3-r^3}{1-r^2} + \frac{v_o\sigma}{a} = 0 \tag{16}$$

where A is a fitting parameter and ν_o is the excluded volume parameter.

We estimated the excluded volume parameter by solving the equation above for the neutral brush:

$$\nu_o = \frac{a r_o^3}{\sigma} \frac{3 - r_o^2}{1 - r_o^2} \qquad 17$$

We assumed that the brush height at the highest salt concentration measured, 2.75 microns, is equivalent to a neutral brush (neutral brush regime). This is likely an overestimate, but unlike the simulations in Chen *et al.* we do not have a neutral brush equivalent to measure. As we do not have a measured molecular weight of the polymer chains, we used the brush height at its most extended to approximate the contour length, N. This is likely an underestimate, but hyaluronan brushes are known to stretch very strongly at low ionic strengths, so it is reasonable for this simple model. We used the value of a = 1 nm for the monomer size of hyaluronan and σ = 0.0021 nm^2 (calculated from our estimated grafting spacing of 22 nm) and thus calculated a ν_o of 27.9.

Assuming a charge fraction, f = 1, we used fmincon in MATLAB to minimize the square of the pressure balance function and calculated r (and thus the brush height) for a range of C_s. Rather than fit the value of A numerically, we selected a value of A by hand to obtain a reasonable fit. This was done due to the low number of experimental data points and a good fit was found at A = 5.

6.3 Response to ethanol

Solvent quality can also be used as a stimulus to influence brush behavior, with the brush being extended in a good solvent and collapsed in a poor solvent. Polyelectrolyte brushes display this behavior and are known to transition into a dense film at high grafting

densities, to form pinned micelle (or octopus micelle) structures in a poor solvent at moderate grafting densities, and to assume single chain globule conformations at low grafting densities.[181] We used ethanol as a poor solvent for the HA backbone, which decreases the effective polyelectrolyte charge due to a decrease in the dielectric constant ($\varepsilon_{ethanol}$=24.5, ε_{water}=80.1) and further decreases solubility through the dehydration of the side groups.[182, 183] The maximum ethanol content achievable for testing is 90% due to water present in the fluorescent nanoparticle bead solution. Starting with a reinforced brush, we measured the height in pure water (16.2 ± 1.2 μm) and then removed the water, washed with ethanol three times and then monitored the brush height over 4 hours. The brush height dropped abruptly to 0.70 ± 0.04 μm, a 96% decrease in thickness (Figure

47A). This is close to the resolution of the microscope (approximately 0.6 μm), so should be taken as an approximate value that represents a very collapsed brush.

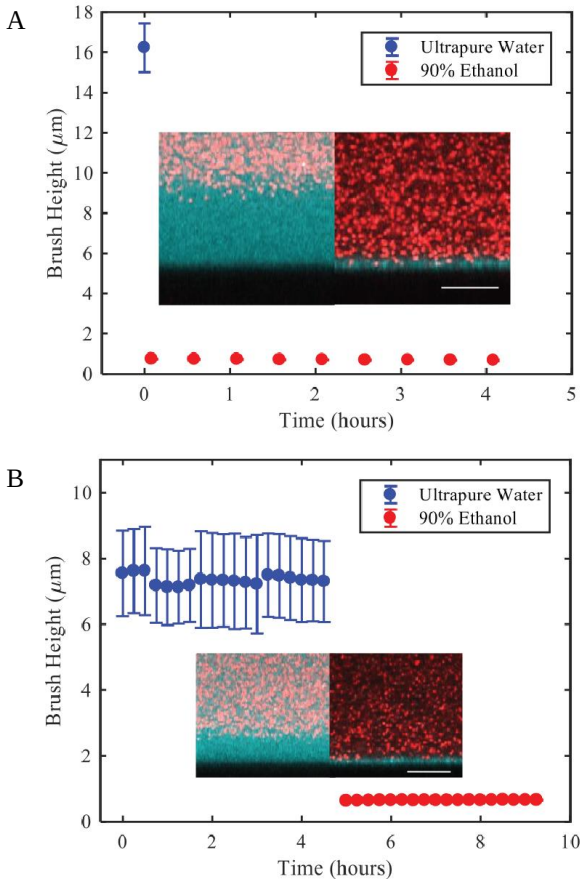

Figure 47. A) Brush height over time through the first solvent exchange. Each data point represents 5 locations sampled on the brush. B) Brush height over time through the second solvent exchange. Each data point represents 2-5 locations sampled on the brush. XZ confocal microscope images of the brush cross section in the different regimes are shown in the insets. Cyan coloring is fluorescent dextran that penetrates the brush, effectively highlighting the brush, and red coloring is the excluded large beads. The substrate is black. All scale bars are 10 μm.

A simple theoretical estimate for polyelectrolyte brush height in a poor solvent can be obtained if we assume a sufficiently dense brush that collapses homogeneously into a film.[64, 181, 182] Due to the very high degree of polymerization (~16,200 for the brushes in this study) and the low grafting spacing (estimated to be approximately d = 22 nm within the fragment), we assume a dense brush, where the collapsed height may be estimated as

$$H = \frac{N\, a^3}{\tau\, d^2} \qquad 18$$

where N is the number of monomers, a is the monomer size (1 nm) and τ is the second virial coefficient indicating the solvent quality ($\tau = \chi^{-1/2}$)). This is the same approach as for a neutral brush, but has shown to be a reasonable estimate for a fully collapsed, dense polyelectrolyte brush.[97] Using values of N = 16,200 and d = 22 nm, as well as τ = 1/2 for a moderately poor solvent, we obtain an estimate for the brush height of a collapsed brush of 67 nm, or a 99.6% decrease in height from its contour length (16,200 nm). This predicts greater brush shrinkage than that observed in the experiments (700 nm, 96%), which is expected for two reasons: 1) the limit of resolution of the confocal microscope method is ± 600 nm, so we are at the limit in measuring the collapsed state and 2) the brush is in 90% ethanol/10% water, which still contains a significant amount of good solvent. It is known that the charges in polyelectrolyte brushes enable them to maintain their extended conformations in much poorer solvent environments than neutral polymers, [97] which can limit full collapse.

6.3.1 Hysteresis in ethanol

Further testing was done on the same brush sample to examine whether it could be re-expanded and re-collapsed. To allow sufficient time for the brush to recover, it was

stored in ultrapure water for two weeks, then rinsed 3 times with fresh ultrapure water and imaged. Figure 3-b shows that the brush height returned partway to the height of the original measurements in water, with an average height of 8.1 ± 1.2 μm. The solvent was then switched to ethanol using 3 washes and the brush height dropped immediately to 0.65 ± 0.03 μm, a 92% decrease in the brush height, consistent with the drop to 0.70 ± 0.04 μm (96% decrease) seen in the first solvent change to ethanol. This shows that re-expansion and collapse occur for the brush, but that the extent of re-expansion is limited, potentially due to slow diffusion of the good solvent into the thick, dense collapsed brush.

To examine the brush expansion and collapse further, we performed a gradual solvent exchange, moving from 100% water to 90% ethanol incrementally. The brush height remained similar to that of pure water up to the 80% ethanol-in-water solution, where it decreased to 2.02 μm compared to the height of the brush in pure water 16.9 μm (88% decrease) (Figure 48). At 90% ethanol-in-water, the brush height decreased to 0.64 compared to the height of the brush in pure water 16.9 μm (96% decrease), identical to the 96% (16.2 to 0.70 μm) drop seen previously from water to 90% ethanol. This indicates that a critical amount of poor solvent is necessary to induce collapse. Interestingly, when the ethanol content is then dropped incrementally from 90% to 0%, the brush height does not recover. Unlike the prior experiment, here the brush was rinsed 3 times with each new solvent and imaged immediately, it was not allowed to incubate for hours in the new solvent. These results show a clear hysteresis in the brush collapse and expansion: when the brush collapses, it does so on the order of minutes, while when the brush re-expands, it only does so after long incubation periods, and even then, not fully.

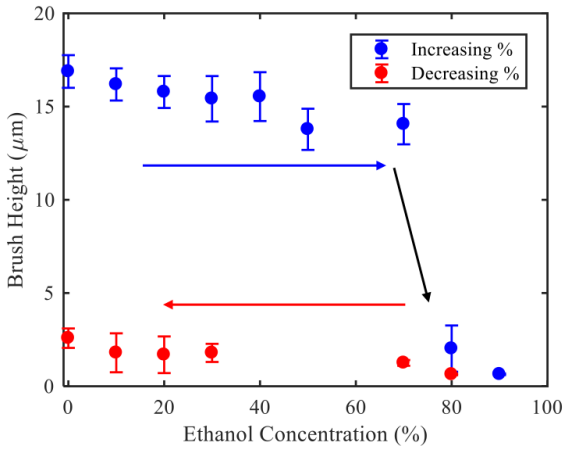

Figure 48. Brush height as a function of ethanol content. Blue data points indicate solvent exchanges proceeding from 0% to 90% (left to right) and red data points indicate solvent exchanges proceeding from 90% to 0% (right to left). Each data point represents at least 4 locations sampled on the brush.

6.4 Summary

In this chapter, we demonstrated that, despite the significantly larger size of the HA brushes prepared through enzyme-mediated growth, they behave similarly to other polyelectrolyte brushes and we can observe this behavior using confocal microscopy. By examining the height of the brush as a function of salt concentration, we demonstrate that the brush displays the osmotic and salted brush regimes that are well known for polyelectrolytes. We also examine the brush conformation in a poor solvent, showing that the brush undergoes a substantial decrease in height (>95%) in 90% ethanol/10% water compared to pure water. This collapse is rapid when changing from a good to a poor solvent, but re-expansion is very slow when changing back to the good solvent.

CHAPTER 7. EFFECT OF FLOW ON BRUSH STRUCTURE

The effect of flow on brushes is an open question for polymer physicists, particularly for polydisperse and polyelectrolyte brushes. Surfaces covered in polymer brushes can be used to influence flow in micro- or nanofluidics. They can act as responsive gating and valves. One could capitalize on the responsive nature of some polymers to control brush permeability and pore size. These smart surfaces are useful in the areas of filtration, fouling resistance, and drug delivery.[184-186] They are even analogs to the glycocalyx found in the vascular system. The glycocalyx, a polymer brush-like meshwork of carbohydrates and proteins surrounding endothelial cells, is exposed to flow in blood vessels. Catheters and intravenous tubes are exposed to flow and are often sources of infection and infection associated with coronary artery stents are rare, but almost always deadly.[187, 188] If a polymer brush coated one of these implants, it would need to withstand flows ranging from 37 μL/sec to 2 mL/sec for tubing or as high as 250 mL/min through the artery.[189, 190] Understanding how polymer brushes respond to dynamic environments like these can allow for the design of such smart materials. Specifically, studying flow on the HA brush will give insight into the stability of the brush in a perturbed environment, as well as allow for its potential applicability to industrial settings to be solidified and quantified.

7.1 Single polymer dynamics

One must begin a discussion of flow over an assembly of polymers by first considering how flow affects an individual polymer since single molecule dynamics can give insight into bulk properties.[191] Single molecule (frequently DNA) dynamics is often

studied through the use of optical tweezers or microfluidic devices paired with fluorescence.[192-194] Perkins et al. said that while the extension of an end-tethered polymer under flow is a balance of hydrodynamic drag and elasticity, many neglect that there is hydrodynamic coupling within the chain. The motions along one part of the chain cause changes in the flow surrounding another part of the chain which therefore changes the resulting hydrodynamic force.[195] Including this component led them to the conclusion that a chain in a steady-state could be modeled like a dumbbell, where there are two beads connected with a spring. The fluctuations of their chains is described by simple Brownian motion and hydrodynamic drag with coupling. Additionally, on fluorescently labeled DNA, they noticed that there is a higher density of monomers at the free end of the polymer, rather than a uniform extension.

Smith and Chu looked at how the conformation of a polymer will affect its extensibility rate.[196] Kinked polymers (an elongated polymer with a coiled section in the middle) and dumbbell shapes (an elongated polymer with one or two coiled ends) unravel quickly when exposed to flow compared to folded polymers (a polymer that doubles back on itself). These polymers with coils extend easier and faster because they are effectively just unraveling. Folded polymers have the disadvantage of having the hydrodynamic drag canceled out along portions of the polymer which will slow the extension rate. In a polymer brush, chains are more likely to be in a semi-dumbbell conformation with the free end coiled to some extent. In 2000, Doyle et al. highlighted the cyclic dynamics of tethered chains whose fluctuations result in a continuous tumbling or recirculation motion. This motion is a result of a gradient in the velocity flow field and thermal fluctuations.[197] In a polymer brush, the bulk dynamics will be affected by the individual dynamics of the

polymers therein. The extent to which those individual chains are affected by flow is determined by the structure of the polymer brush (aka the conformations of the chains) and the density (the extent to which chains will affect their neighbor).

7.2 Conflicting literature

There has been quite a lot of work, both theoretical and experimental, done to tease out a predictable response of polymer brushes to flow. Such work has not resulted in a coherent model for polymer brush response as there is a lot of conflicting literature where applications of flow to a brush resulted in brush height increasing [198], no change [199, 200] [201], decreasing, [202] [203] [204] or where the result depends on a critical flow rate which is influenced by the grafting density.[205] [204] Beyond this critical flow (or shear) rate, desorption can happen abruptly which would result in shear-induced thinning.[200, 202] Harden et al found through theoretical modeling of a polyelectrolyte brush that the stretching of polymers in the brush due to flow was dependent on the charge fraction of the polymer.[198, 206] Lanotte et al found that the longest chains in a polydisperse brush contributed to increased drag and a reduction in flow rate through microchannels coated in brushes.[207]

Interestingly, there has been a lot of discussion around cases of unchanging brush height and decreasing brush height. Zuckerman modeled polymers under flow and showed that they would uncoil which would lead to an increase in brush height, but due to the application of perpendicular flow, these polymers tilted to align with the flow.[201] This stretching and tilting would result in a negligible change in brush height. In 1996, Aubouy et al proposed a “dual chain” model where they said there were two types of chains within

a brush under flow: 1) “dragged chains,” which are exposed to the flow and 2) “quiescent chains” which are deeper within the brush and screened from the flow. Karniadakis suggested that a strong shear flows, untangled polymers perform cyclic and tumbling motions which serve to not only decrease the brush height, but also allows the brush to be penetrated by the flow and a flow reversal at the brush surface. In weak flows, there would be no tumbling of the polymers and thus the brush would remain undisturbed.[204]

7.3 Monodisperse and polydisperse brushes in flow

Milner was one of the first to theorize on the effects of flow across a monodisperse polymer brush. He suggested that the parabolic density profile of a brush dictated the depth that a flow can penetrate (Figure 49A, B).[208, 209] Recently, through theoretical modeling and simulation, Qi et al found that the depth of flow penetration into the brush increases with increasing polydispersity.[208]

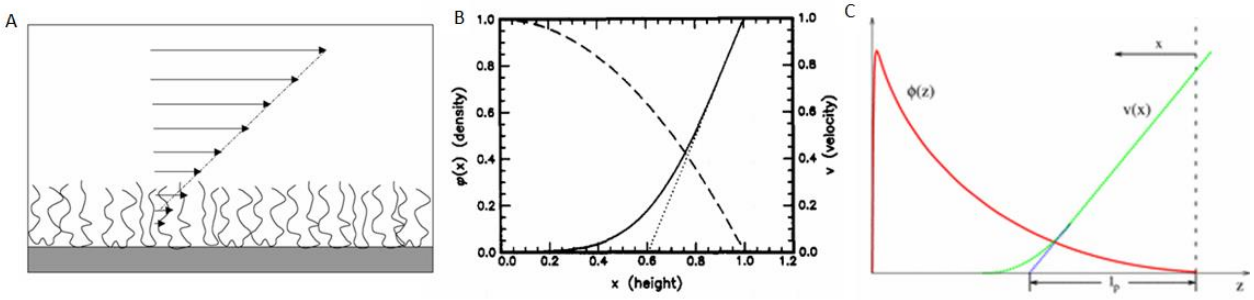

Figure 49. A) Shear flow over a polymer brush where the penetration depth is the depth at which the velocity of the shear flow vanishes. B) The penetration depth (solid line) plotted with respect to the parabolic density profile (dashed line) of a monodisperse brush. C) The penetration depth (green line) plotted with respect to the density profile (red) of a polydisperse brush. These images were originally published by, respectively, McLean et al [94,103], Milner [94], and Qi et al [93]. Reprinted here under the Attribution-NonCommercial 4.0 International (CC BY-NC 4.0).

7.4 Experimental work to add to the field

There is a considerable lack of experimental work, especially in the case of polydisperse brushes, which are of particular interest as they are the best analogs to natural systems. To elucidate the behavior of a polydisperse brush, one could perform the following studies. For unreinforced brushes, flow rate could be varied and compared to the molecular weight of HA collected in the effluent to changes in the brush structure as evidenced by fluorescent labeling or azide-modification. In addition to allowing for brush structure to be investigated, these studies would additionally open the door to try to answer questions about the strength of HA to HAS binding. With reinforced brushes, flow penetration without loss of polymers would be possible to study. Particle penetration under flow would also be possible to study as there are predictions for penetration based on polymer blob size which is hypothesized to decrease with increasing flow. [210] These kinds of characterizations will be important to understand and control if the HA brush is to be used as a biomaterial in a future application. Importantly, different molecular weights of HA have different effects in the body. Low molecular weight HA causes inflammatory responses and is associated with adverse pathologies, whereas high molecular weight can play a protective role and is generally considered beneficial.[26] Based on the molecular weight of HA in the effluent at different time points, the characteristics of the biomaterial can be tuned and possibly manufactured to shed desirable HA.

7.5 Need for a new sample holder

Growing the HA brush in capillaries had a two-fold motivation: 1) increasing the resolution of brush profiles and 2) flow studies. In 2012, Lanotte et al fabricated what they

termed “hairy” capillaries where they coated the interior of a capillary space with a polymer brush on the order of 100-400 nm thick.[207] They used pressure-driven flow to study the velocity profile across the width of the capillary and determined there was a significant reduction in flow due to the presence of the polymer brush on the walls of the capillary. They noted specifically that the reduction in flow could not be accounted for solely by assuming a thinner capillary by an amount equal to two times the height of the brush. They hypothesized that their system had some polydispersity and that the longer chains caused a drag effect which decreased the maximum velocity through the channel. They also proposed that since the polymers can tumble that the subsequent flow reversal at the surface could also serve to decrease the maximum flow velocity. This study is a nice precursor to our studies of our “hairy” capillaries. They had thorough studies of the brushes on planar surfaces and noted that it was very difficult to perform qualitative characterization of the capillary brushes without damaging the capillaries themselves. Therefore, they did not do extensive characterization of the brush within the capillaries and relied on their planar studies to inform their interpretation of the results. It is also important to note that there is still room for our studies of flow on brush structure and possible desorption since this study focused on the effect of the brush on flow rather than the opposite.

7.6 Brush growth in glass capillaries

To support these studies, we have shown that HA brushes can be grown on the interior of 800 μm square glass capillary tubes (Figure 50A). To determine the brush height of a planar brush, the laser scanning confocal microscope takes a series of XY images in the z-direction (perpendicular to the substrate), which constitutes a “z-stack”. The intensity profile of the fluorescent nanoparticles in the images are analyzed as previously described

and the resulting height has a minimum resolution of ~500 nm. With the square capillary, images of the side walls can be taken in XY. Since the brush will be covering all the interior of the capillary, the brush will be visible in one XY image (Figure 50B) and the maximum resolution will be ~200 nm. This will allow more precise measurements to be taken of the brush height, as well as being able to capture dynamics faster since taking one XY image is faster than a series of XY images for a z-stack.

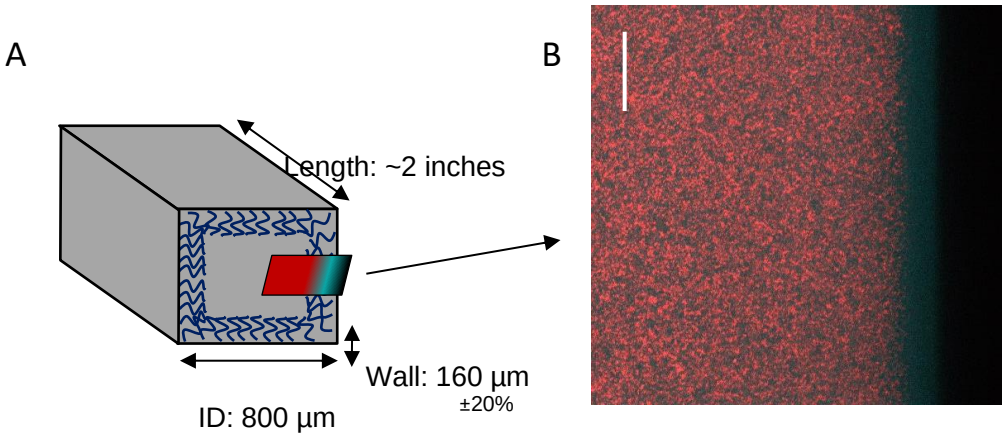

Figure 50. A) Schematic of the glass capillary tubes and their dimensions; length, wall thickness, and inner diameter. The XY image (B) of the 4 hr brush taken at a height Z along the wall. The red, 200 nm particles are excluded from the brush. The cyan fluorescent dextran between the glass wall and the edge of red beads is where the brush is present. Scale bar is 20 µm.

7.7 Modifying the sample holder

To be able to image a level capillary, a new microscope stage mount had to be fabricated. An existing Teflon ring holder was easily modified in the GT Machining Mall by cutting a square channel just slightly larger than the width of the capillary. Additionally,

some of the Teflon had to be removed from the bottom of the ring because the objective could not be raised height enough to meet the capillary in this configuration. Figure 51 shows the final product.

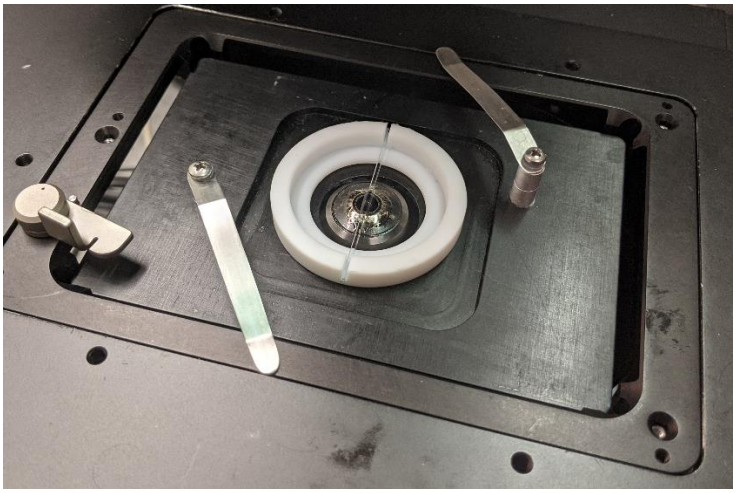

Figure 51. The modified Teflon ring holder with a grove cut through it matching the width of the glass capillary. The 60x oil objective has access to the capillary through the hole of the ring and due to the decreased thickness of the Teflon ring after modification.

7.8 Capillary corners

A few imaging hiccups occurred along the way that still need to be resolved before quantitative studies can be pursued. It seemed that the brush height on the bottom of the tube (viewed as just a planar brush) was not consistent across the entire bottom. (Figure 53) The image in the figure is five images stitched together to capture the complete width of the capillary. There appears to be brush in the very center stripe along the wall of the capillary, but as the walls are approached, there are wide gaps where there does not appear

to be brush present. We hypothesized that the plasma cleaning was not effective in such tight spaces and therefore the subsequent layer depositions were ineffective near the corners. Piranha cleaning was employed instead, but the effect persisted.

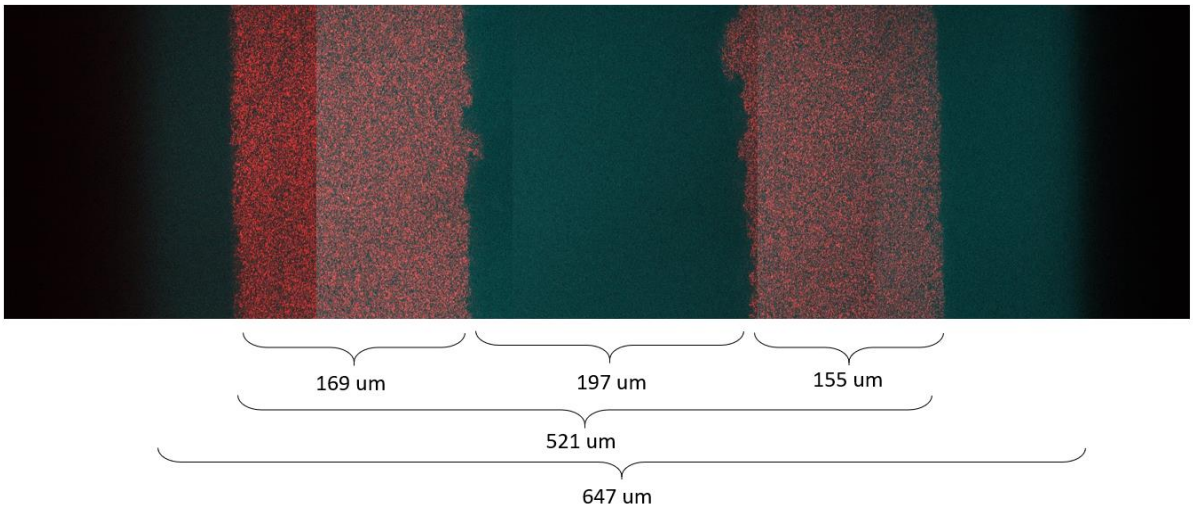

Figure 53. A top-down view of the bottom of the capillary across the entire width. The approximate width of the relevant sections are labeled. 200 nm red fluorescent particles show areas with no brush and cyan fluorescent dextran is present everywhere.

When looking at brush height along the walls of the capillaries, it appeared that the brushes got thicker and thicker as the z-position of the images decreased. In Figure 52, the height above the bottom of the capillary is noted and the gap between the glass (black) and

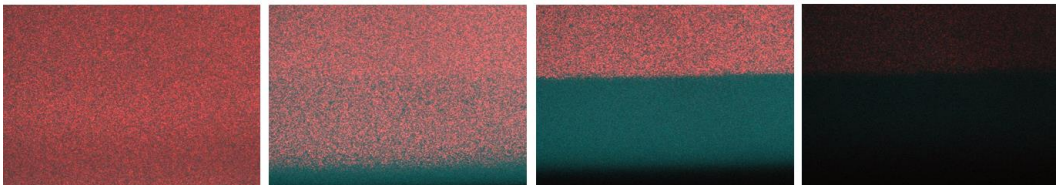

Figure 52. Apparent increase in brush thickness as height above the bottom of the capillary decreased (from left to right).

red beads shows the brush. The brush appears to be thickest closest to the bottom and decreases with increasing height.

This motivated a closer look at the corners of the capillaries as it is unlikely that they perfect square corners and more likely to have some curvature present. The manufacturer (Vitrocom) was unable to provide any characterization of the interior corners. In Figure 54, the capillary was filled with fluorescent dextran and imaged in a 100 µm zstack. There is clearly some curvature present in the corners. There also appears to be some aberration occurring during imaging as we pass from the curved portion to the flat upper wall since there appears to be a discontinuity in the bright band of fluorescent dextran that is non-specifically bound to the interior surface. Importantly, along the wall, the bright band of dextran gets hazy and so attempts to use surface labeling to find the bottom of the brush (aka, the glass interface of the wall) could prove tricky.

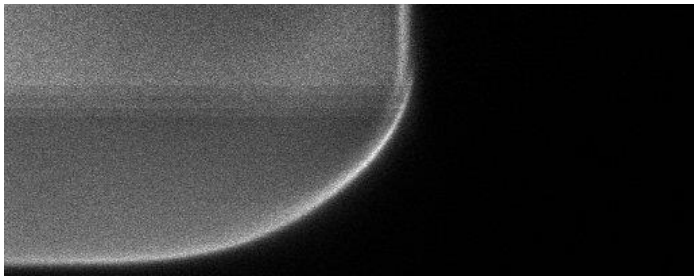

Figure 54. The bottom corner of a capillary filled with fluorescent dextran.

7.9 Preliminary flow set up

Despite imaging the walls of the capillary posing some technical difficulties, we pressed on to try to do some preliminary flow work since effluent could easily be collected and analyzed. Setting up a syringe pump mediated flow proved to be non-trivial. Attaching microfluidic tubing (by pushing the capillary into the tubing) to the capillary twists the

capillary ever so slightly, but it is enough to cause the capillary to not sit flush in the Teflon ring. The microfluidic tubing also has a “square peg in a round hole” problem in that the capillary is square and the tubing is round. When flow is applied, you can see fluid slowly leaking out of the connection points. (Figure 55A) This can be remedied by applying vacuum grease at the connection point and wrapping with saran wrap. (Figure 55B) But that has the disadvantage of excessive handling of the tubing while there is liquid present and it can flow from side to side within the capillary, applying unknown shear to the brush before it can even be imaged. The tubing could be applied and secured before brush growth, but the handler would need be to very careful about changing the syringes from flowing in growth media to imaging media. If the handler ensures that all tubing connections and syringes remain in the same XY plane, there should be minimal changes to the fluid levels in the tubes and minimal unknown flows applied during solution swaps.

The twisting of the capillary due to the microfluidic tubing could possibly be mediated by spending some time unraveling the tubing prior to use. It is stored in a tightly coiled state and dedicating time to straightening the inherent coil would help. (Figure 55C) Even if one could straighten out the tubing, there is still an issue with the tubing getting pulled and kinked as it approaches the Teflon ring due to the stage insert. (Figure 55D, E) The recessed nature of the stage insert requires the tubing to make a quick plane change that results in the tubing pulling the capillary upwards or even putting a kink in the tubing which could negatively affect the flow rate.

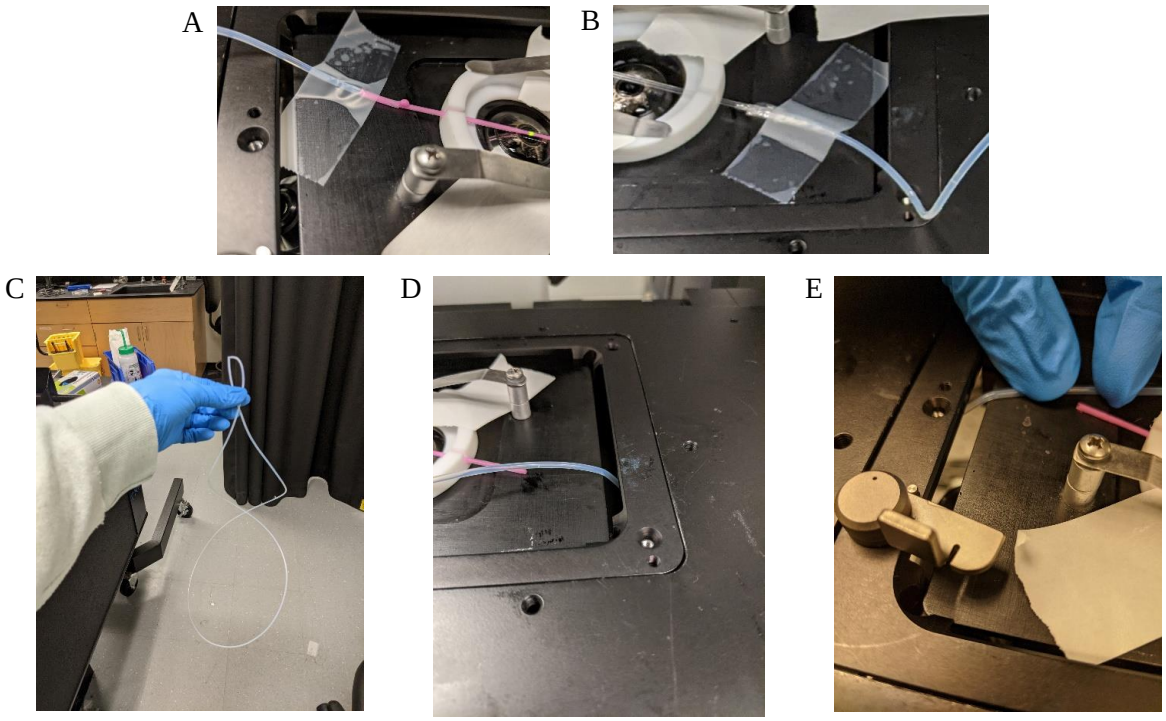

Figure 55. A) Solution leaking from the capillary-tubing connection point. B) The capillary-tubing connection point covered in vacuum grease and wrapped in saran wrap as a seal. C) The tubing is store tightly coiled and this is the relaxed state of the tubing after unpacking. D) The tubing kinks slightly as it approaches the capillary which results in the tubing pulling the capillary out of the Teflon ring unless the tubing is taped to the stage. A similar thing happens if the tubing approaches from above the stage as in B. E) Similar tubing kink as the tubing leaves the capillary on the other side.

CHAPTER 8. OUTLOOK

8.1 Kinetics of brush collapse and re-expansion

For kinetic studies, we have explored transition timescales to ensure we can capture the brush reconfiguration in real time. We pushed this limits of laser scanning confocal microscopy to track the brush interface upon changes of environmental conditions. Preliminary experiments determined that the timescale in which a brush interface moves to a new equilibrium position occurs in less than 16 sec. To achieve high speed imaging of the brush interface, we increased the rate of imaging full z-stacks of the brush by reducing the area (to ~50 x 50 μm^2) and the resolution (to 64 x 64). This sharply reduced the acquisition time to eight seconds per brush scan, which consisted of 31 slices with 0.5 µm resolution. This was sufficient to capture some of the transition when exchanging salt solutions (150 mM) with ultra-pure water. Figure 56 shows the outcome of these experiments.

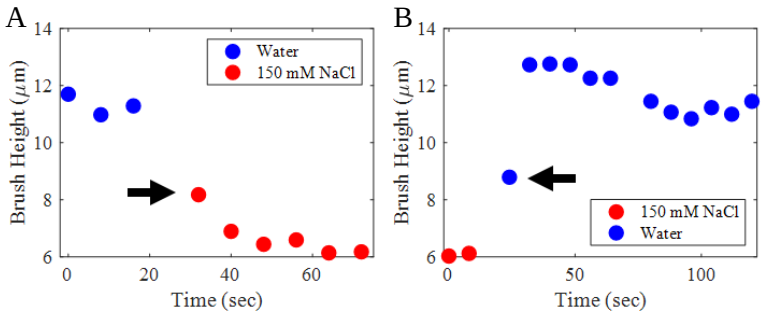

Figure 56. A) Brush in ultrapure water for three images before solution is exchanged for 150 mM NaCl. This causes the brush to rapidly shrink from 11.3 ± 0.3 µm to 6.3 ± 0.3 µm. B) Transition back to water reveals transition step and return to the extended height of 11.2 ± 0.3 µm. The black arrows indicate transition steps from one equilibrium to the other.

The black arrows indicate the single event where the moving brush front is clearly captured, first in the brush collapse after exposure to salt (Figure 56A) and then the brush exposure to ultra-pure water (Figure 56B). In the data in the second transition (salt to water), an interesting effect may be hinted at. It is seen that the brush shoots up to a height of ~12.5 μm and then relaxes to a height of ~11.2 μm. Complete analysis is limited by the resolution of the measurement, but with refinement (use of capillary brushes) such resolution could be achieved. This temporary overshoot could be due to a combination of effects from ion diffusion, equilibration of molecules between the brush and the bulk, and polymer chain relaxation effects. These potentially interesting results and our ability to clarify the details highlight the power that this experimental platform will provide.

Looking to the future, the Spinning Disk confocal microscope, available in core facilities at GT or other approaches can further improve the time resolution in these experiments. We estimate frame rates up to about 1 Hz (1 full brush z-stack per second) can be easily achieved with Spinning Disk confocal. This would provide nearly 10-fold increase in speed compared to the data shown in Figure 56 – likely sufficient to resolve the kinetics of interest in the myriad of conditions we propose to explore. Additionally, if faster timescales are desirable, an alternative route is to work with brushes grown in glass capillaries (Figure 50), where lateral imaging in the x-y plane can correspond to brush profile. This would enable visualization of the full brush in one single time step. On the CSLM then, we could reduce the number of z-slices from 30 to 5 (to enable some averaging). This will increase the rate of imaging by a factor of 6 (to 1.3 Hz). On the spinning disk confocal, we could do the same and achieve a rate of 6 brush scans per second

(6 Hz). Reducing the redundancy in z (now perpendicular to the brush profile) would further increase the speed up to ~30 Hz.

8.2 Optimize reinforcement

There have been times over the last year where reinforcement has been unreliable. Despite purchasing fresh EDC and Sulfo-NHS for the carbodiimide chemistry and having different students perform the reinforcement, there has been inconsistent results – both in final brush height and long-term stability. Future work should begin with a methodical approach to troubleshooting the brush reinforcement protocol, including validating preliminary results that suggests less 'rounds' of EDC/Sulfo-NHS exposure is just as effective as multiple 'rounds'. (Figure)

It is an accepted fact in our lab that the reinforcement protocol results in some brush loss. This is due to a combination of factors. The reinforcement protocol requires multiple stages of washing the brush, it requires long periods of time where the brush is sitting at room temperature on the bench, and it is done in water. It should be determined if the reinforcement could be performed in 150 mM NaCl, which might help retain the brush height since unreinforced brushes in water lose polymers which reduces the subsequent brush height.

The fluorescent labeling protocol with an Alexa Fluor hydrazide dye uses the same carbodiimide chemistry, but the solution must be at a pH of 4.75 or the labeling does not occur. The reinforcement protocol solutions are all at a pH of ~7.3. Preliminary attempts to investigate if reinforcement would be more effective if a lower pH was employed resulted in no brush being visible after reinforcement.

8.3 Brushes in confinement

HA brushes could be studied in confined geometries by investigating the corners of capillaries and by purchasing sufficiently skinny capillaries such that the walls are only separated by a distance equal to a few brush heights in salt. Studies of how the brushes interact when swollen or under flow would be enhanced through fluorescent labeling of the brush itself. These confined geometry studies would be useful since they would mimic realistic environments. PDMS microfluidic channels could also be constructed as an alternative to capillaries for flow studies.

8.4 Nanoparticle penetration profiles

Graduate students Lars Veldscholte, Parisa Mollaei, and Katherine Powell have all contributed to ongoing work to determine nanoparticle penetration profiles for brushes of different growth times and salinities. This work is important to determine the pore size of the brush and how that size is affected by salt concentration, flow, and molecular weight distribution. Crosslinking of the brush would also affect both the stiffness of the brush (an important material property for biomedical applications) and the porosity.

8.5 Change fragment immobilization scheme

As is abundantly clear, the membrane fragment surface is very sticky and all manner of proteins and dyes will bind to the surface which often interferes with the quantitative analysis of the respective experiments. The scheme for fragment immobilization could be modified to decrease the potential for non-specific surface binding

of reagents in solution. If the fragments and glass surface could be biotinylated, streptavidin could be used to bridge the link between them.

8.6 AFM modulus and grafting density

In collaboration with the Hu lab, graduate student Dongjing He has begun work studying the dependence of brush stiffness on growth time (and hence MW distribution). The stiffness of the brushes is dependent on not only the polydispersity, but also possibly crosslinking and the presence of side groups such as aggrecan or a fluorophore. Future work is planned to extract the grafting density through AFM scratch testing for brushes of various growth time to demonstrate a consistent grafting density, as well as extract the exact grafting density of patterned regions.

8.7 Freezer storage time of samples

Undergraduate student Ellen Park is investigating how prepared fragment surfaces perform vs time stored in -20 ºC freezer by measuring one surface every few months. The Covid-19 pandemic has pushed this work to extend beyond a year once finished and preliminary findings suggest that 4 hr brush height is unaffected by 161 days of storage of the surface pre-growth. These results would enable more efficient surface prep ahead of time by preparing samples in bulk.

8.8 Anti-biofilm properties and biomedical applications

Motivated by the possibility of biomaterials applications such as implants and treatment of chronic wounds, in collaboration with fellow graduate student Hemaa Selvakumar, we explored the interaction of bacteria with the HA brushes. [211] The

prevention of bacterial infection is another crucial aspect of both implants and wound treatments – in particular the problem of biofilm formation and adhesion. Encouraged by the observation that the brushes sterically exclude particles greater than 100 nm, and that HA is a known anti-fouling polymer, we examined whether the biofilm forming bacteria *Pseudomonas aeruginosa* (PAO1) are capable of irreversibly attaching to the brush interface and establishing a biofilm.[212-215] Both natural and reinforced brushes repelled the bacteria, natural brushes for at least one week (until the brush decays) and reinforced brushes for at least two weeks when the experiments ended – as determined by high resolution confocal microscopy. Few bacteria reached the underlying substrate in this time. In both cases, removing the bacteria from the brush interfaces was straightforward, and verified with confocal microscopy.

Next, systematic characterization of the brush-bacterial interaction was repeated three times, exposing reinforced brushes to GFP-expressing PAO1 bacteria for one and/or five days, rinsing, and then imaging remnant bacteria attached to or embedded within the brush. Each sample was randomly imaged at five locations and the total volume occupied by bacteria assessed to estimate the number of bacteria (Figure 57A-D). The results were compared with PAO1 biofilm formation on glass and HA thin films. The images in the left column correspond to the three surfaces (glass, HA film, HA brush) prior to washing. The right column shows the same samples after washing. Quantification of the total number of bacteria under each condition is summarized in Figure 57D (and Table 7). The percentage bacteria relative to the glass slide was dramatically decreased on both the HA film and even more so on the HA brush at 1 and 5 days. (See Figure 57D and Table 8) The glass surfaces retain 99% more bacteria than the HA brushes after one day. As expected, the HA film

shows improved resistance to fouling, yet it still retains six times more bacteria than the HA brush (Figure 57C) after both 1 and 5 day exposures. On the HA brushes, only 1-2% of the remnant adhered bacteria were found at the underlying brush-glass interface. Addressing the brush uniformity, not yet optimized, could further improve the outcomes.

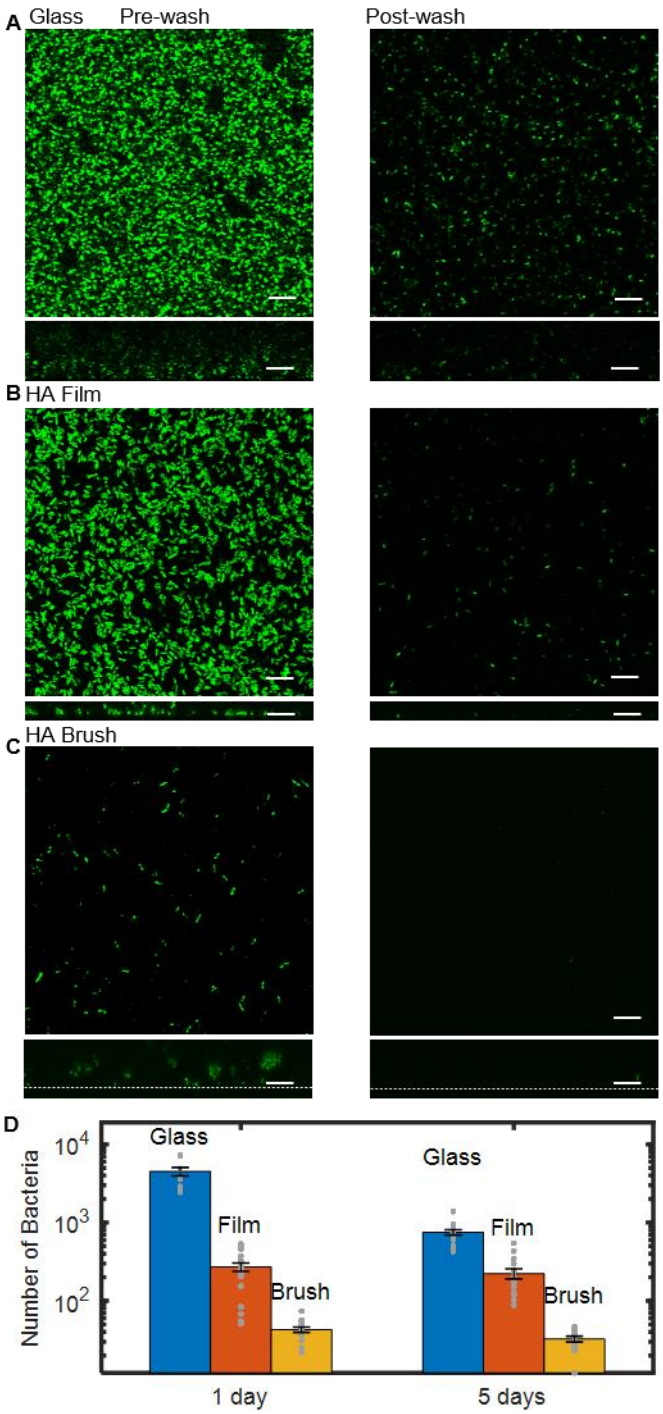

Figure 57. Confocal micrographs of GFP-producing *Pseudomonas aeruginosa* (PAO1) interacting with a glass interface (A), a HA film (B), and a reinforced HA brush (C). All images were taken at the glass interface. Left: biofilm growth before washing (1 day). Right: biofilm growth after washing (1 day). Dextran was used to identify the glass interface beneath the brush. XZ side views of the biofilms are presented below each respective XY top view of the samples. Scale bars, 10 μm in A, B, and C. D) Comparison of the number of bacteria retained after washing different surfaces. Data were taken in triplicates and averaged over 5 regions per sample. Error is SEM.

Table 7. Retainment of Bacteria in Biofilms on Different Substrates. Total number of PAO1 bacteria post-wash on glass, HA film and HA brush in a 211 x 211 x 5 um^3 volume averaged over 5 measured areas.

	# of bacteria	Glass	Film	Brush
1 day	**Mean**	4518	271	43
	SEM	567	33	3
5 days	**Mean**	752	224	32
	SEM	58	33	3

Table 8. % Retainment of Bacteria in Biofilms on Different Substrates. Relative percentage PAO1 bacteria adherent to HA film and HA brush post-washing as compared to the bacteria sticking to the glass substrate.

	% (rel. glass)	Glass	Film	Brush
1 day	**Mean**	100%	6.0%	0.95%
	SEM	13.0%	0.7%	0.07%
5 days	**Mean**	100%	30%	4.3%
	SEM	7.8%	4.4%	0.34%

In future work, the antifouling properties of the brush could be complemented with doping the brush with anti-microbial compounds using straightforward and accessible chemistry associated with HA. Further, the selective biointeractivity, i.e. inhibition of pathogenic microbial adhesion but enhancement of beneficial host cell responses, establishes the HA brush interface an interesting option for coating implants, bandages or other materials with similar requirements. [216] Biomedical tools that could benefit from this technology such as implants or bandages may require large surface areas. It is possible to scale up the surface area covered. We estimate that 1 L of (*E. coli*) bacterial culture can be used to cover ~2 m^2 of area. Binding the membrane fragments to other materials such as plastic or titanium, i.e. for catheters or implants, should be achievable using modified surface functionalization schemes.

REFERENCES

1. Milner, S.T., T.A. Witten, and M.E. Cates, *Theory of the grafted polymer brush.* Macromolecules, 1988. **21**(8): p. 2610-2619.

2. Zhulina, E.B. and O.V. Borisov, *Structure and interaction of weakly charged polyelectrolyte brushes: Self-consistent field theory.* The Journal of Chemical Physics, 1997. **107**(15): p. 5952-5967.

3. Balastre, M., et al., *A Study of Polyelectrolyte Brushes Formed from Adsorption of Amphiphilic Diblock Copolymers Using the Surface Forces Apparatus.* Macromolecules, 2002. **35**(25): p. 9480-9486.

4. S. Sanjuan, P.P., N. Pantoustier, and Y. Tran, *Synthesis and Swelling Behavior of pH-Responsive Polybase Brushes.* Langmuir, 2007. **23**: p. 5769-5778.

5. Brettmann, B.K., et al., *Bridging contributions to polyelectrolyte brush collapse in multivalent salt solutions.* Journal of Polymer Science Part A: Polymer Chemistry, 2016. **54**(2): p. 284-291.

6. Brettmann, B., P. Pincus, and M. Tirrell, *Lateral structure formation in polyelectrolyte brushes induced by multivalent ions.* Macromolecules, 2017. **50**(3): p. 1225-1235.

7. Yu, J., et al., *Multivalent ions induce lateral structural inhomogeneities in polyelectrolyte brushes.* Science advances, 2017. **3**(12): p. eaao1497-eaao1497.

8. Yadav, V., et al., *Tuning Bacterial Attachment and Detachment via the Thickness and Dispersity of a pH-Responsive Polymer Brush.* ACS Applied Materials & Interfaces, 2017. **9**(51): p. 44900-44910.

9. Omar Azzaroni, S.M., Tamer Farhan, Andrew A. Brown, and Wilhelm T. S. Huck, *Switching the Properties of Polyelectrolyte Brushes via "Hydrophobic Collapse".* Macromolecules, 2005. **38**: p. 10192-10199.

10. Yu, J., et al., *Structure of Polyelectrolyte Brushes in the Presence of Multivalent Counterions.* Macromolecules, 2016. **49**(15): p. 5609-5617.

11. Yu, J., et al., *The effect of multivalent counterions to the structure of highly dense polystyrene sulfonate brushes.* Polymer, 2016. **98**: p. 448-453.

12. Martin Gelbert, M.B., Jurgen Ruhe, and Diethelm Johannsmann, *Collapse of Polyelectrolyte Brushes Probed by Noise Analysis of a Scanning Force Microscope Cantilever.* Langmuir, 2000. **16**: p. 5774-5784.

13. Raviv, U., et al., *Lubrication by charged polymers.* Nature, 2003. **425**(6954): p. 163-165.

14. Fan, R., et al., *Integrated barcode chips for rapid, multiplexed analysis of proteins in microliter quantities of blood.* Nature Biotechnology, 2008. **26**(12): p. 1373-1378.

15. Drummond, T.G., M.G. Hill, and J.K. Barton, *Electrochemical DNA sensors.* Nature Biotechnology, 2003. **21**(10): p. 1192-1199.

16. Farina, R., et al., *Brushes of strong polyelectrolytes in mixed mono- and tri-valent ionic media at fixed total ionic strengths.* Soft Matter, 2013. **9**(44): p. 10458-10472.

17. Cheesman, B.T., et al., *Polyelectrolyte brush pH-response at the silica–aqueous solution interface: a kinetic and equilibrium investigation.* Physical Chemistry Chemical Physics, 2013. **15**(34): p. 14502-14510.

18. Farhan, T., O. Azzaroni, and W.T.S. Huck, *AFM study of cationically charged polymer brushes: switching between soft and hard matter.* Soft Matter, 2005. **1**(1): p. 66-68.

19. Bracha, D. and R.H. Bar-Ziv, *Dendritic and nanowire assemblies of condensed DNA polymer brushes.* J Am Chem Soc, 2014. **136**(13): p. 4945-53.

20. Kim, Y.-R., et al., *Enzymatic Surface-Initiated Polymerization: A Novel Approach for the in Situ Solid-Phase Synthesis of Biocompatible Polymer Poly(3-hydroxybutyrate).* Biomacromolecules, 2004. **5**: p. 889-894.

21. Barbee, K.D., M. Chandrangsu, and X. Huang, *Fabrication of DNA polymer brush arrays by destructive micropatterning and rolling-circle amplification.* Macromolecular Bioscience, 2011. **11**(5): p. 607-17.

22. Wei, W., et al., *Self-regenerating giant hyaluronan polymer brushes.* Nature Communications, 2019. **10**(1): p. 5527.

23. Allison, D. and K. Grande-Allen, *Review. Hyaluronan: A Powerful Tissue Engineering Tool.* Tissue engineering, 2006. **12**: p. 2131-40.

24. Chircov, C., L.E. Grumezescu Am Fau - Bejenaru, and L.E. Bejenaru, *Hyaluronic acid-based scaffolds for tissue engineering.* (2066-8279 (Electronic)).

25. Karbownik, M.S. and J.Z. Nowak, *Hyaluronan: towards novel anti-cancer therapeutics.* (1734-1140 (Print)).

26. Bohaumilitzky, L., et al., *A Trickster in Disguise: Hyaluronan's Ambivalent Roles in the Matrix.* Frontiers in Oncology, 2017. **7**.

27. Weigel, P.H., *Hyaluronan Synthase: The Mechanism of Initiation at the Reducing End and a Pendulum Model for Polysaccharide Translocation to the Cell Exterior.* Int J Cell Biol, 2015. **2015**: p. 367579.

28. Faubel, J.L., et al., *Giant Hyaluronan Polymer Brushes Display Polyelectrolyte Brush Polymer Physics Behavior.* ACS Macro Letters, 2019. **8**(10): p. 1323-1327.

29. Iuliana Gatej, M.P., and Marguerite Rinaudo, *Role of the pH on Hyaluronan Behavior in Aqueous Solution.* Biomacromolecules, 2005. **6**: p. 61-67.

30. Mero, A. and M. Campisi, *Hyaluronic Acid Bioconjugates for the Delivery of Bioactive Molecules.* Polymers, 2014. **6**(2).

31. Israels, R., et al., *pH-Controlled Gating in Polymer Brushes.* Macromolecules, 1994. **27**(22): p. 6679-6682.

32. Toole, B.P., *Hyaluronan: from extracellular glue to pericellular cue.* Nat Rev Cancer, 2004. **4**(7): p. 528-39.

33. DeAngelis, P.L., *Hyaluronan synthases: fascinating glycosyltransferases from vertebrates, bacterial pathogens, and algal viruses.* Cellular and molecular life sciences : CMLS, 1999. **56**(7-8): p. 670-682.

34. Weigel, P.H. *Bacterial Hyaluronan Synthases*. [cited 2017; Available from: http://glycoforum.gr.jp/science/hyaluronan/HA06/HA06E.html.

35. Stern, R., *Hyaluronan catabolism: a new metabolic pathway.* European journal of cell biology, 2004. **83**(7): p. 317-325.

36. Kakizaki, I., et al., *Up-regulation of hyaluronan synthase genes in cultured human epidermal keratinocytes by UVB irradiation.* Archives of Biochemistry and Biophysics, 2008. **471**(1): p. 85-93.

37. Rangaswamy, V. and D. Jain, *An efficient process for production and purification of hyaluronic acid from Streptococcus equi subsp. zooepidemicus.* Biotechnology Letters, 2008. **30**(3): p. 493-496.

38. Evanko, S.P., et al., *Hyaluronan-dependent pericellular matrix.* Advanced Drug Delivery Reviews, 2007. **59**(13): p. 1351-1365.

39. Kawada, C., et al., *Oral administration of hyaluronan prevents skin dryness and epidermal thickening in ultraviolet irradiated hairless mice.* Journal of Photochemistry and Photobiology B: Biology, 2015. **153**: p. 215-221.

40. Goto, M., et al., *Intra-articular injection of hyaluronate (SI-6601D) improves joint pain and synovial fluid prostaglandin E2 levels in rheumatoid arthritis: A multicenter clinical trial.* Clinical and Experimental Rheumatology, 2001. **19**: p. 377-383.

41. Campo, G.M., et al., *Hyaluronan reduces inflammation in experimental arthritis by modulating TLR-2 and TLR-4 cartilage expression.* Biochimica et Biophysica Acta (BBA) - Molecular Basis of Disease, 2011. **1812**(9): p. 1170-1181.

42. Berezney, J.P. and O.A. Saleh, *Electrostatic Effects on the Conformation and Elasticity of Hyaluronic Acid, a Moderately Flexible Polyelectrolyte.* Macromolecules, 2017. **50**(3): p. 1085-1089.

43. D'Agostino, A., et al., *In vitro analysis of the effects on wound healing of high- and low-molecular weight chains of hyaluronan and their hybrid H-HA/L-HA complexes.* BMC Cell Biology, 2015. **16**(1): p. 19.

44. Li, S., et al., *Sequential one-pot multienzyme synthesis of hyaluronan and its derivative.* Carbohydr Polym, 2017. **178**: p. 221-227.

45. Tlapak-Simmons, V.L., C.A. Baron, and P.H. Weigel, *Characterization of the purified hyaluronan synthase from Streptococcus equisimilis.* Biochemistry, 2004. **43**(28): p. 9234-9242.

46. Kumari, K. and P.H. Weigel, *Molecular cloning, expression, and characterization of the authentic hyaluronan synthase from group C Streptococcus equisimilis.* Journal of Biological Chemistry, 1997. **272**(51): p. 32539-32546.

47. Valarie L. Tlapak-Simmons, B.A.B., Tracy Clyne, and Paul H. Weigel, *Purification and Lipid Dependence of the Recombinant Hyaluronan Synthases from Streptococcus pyogenes and Streptococcus equisimilis.* THE JOURNAL OF BIOLOGICAL CHEMISTRY, 1999. **274**(7): p. 4239–4245.

48. Baggenstoss, B.A. and P.H. Weigel, *Size exclusion chromatography-multiangle laser light scattering analysis of hyaluronan size distributions made by membrane-bound hyaluronan synthase.* Anal Biochem, 2006. **352**(2): p. 243-51.

49. Weigel, P.H. and B.A. Baggenstoss, *Hyaluronan synthase polymerizing activity and control of product size are discrete enzyme functions that can be uncoupled by mutagenesis of conserved cysteines.* Glycobiology, 2012. **22**(10): p. 1302-10.

50. Paul H. Weigel, V.C.H., and Markku Tammii, *Hyaluronan Synthases.* THE JOURNAL OF BIOLOGICAL CHEMISTRY, 1997(22): p. 13997–14000.

51. Milner, S.T., *Polymer Brushes.* Science, 1991. **251**(4996): p. 905-914.

52. Gennes, P.G.d., *Conformations of Polymers Attached to an Interface.* Macromolecules, 1980. **13**: p. 1069-1075.

53. Costerton, J.W., R.T. Irvin, and K.-J. Cheng, *The Bacterial Glycocalyx in Nature and Disease.* Annual Review of Microbiology, 1981. **35**: p. 299-324.

54. Weigel, K.K.a.P.H., *Molecular Cloning, Expression, and Characterization of the Authentic Hyaluronan Synthase from Group C Streptococcus equisimilis.* THE JOURNAL OF BIOLOGICAL CHEMISTRY, 1997. **272**(51): p. 32539–32546.

55. Reitsma, S., et al., *The endothelial glycocalyx: composition, functions, and visualization.* Pflügers Archiv - European Journal of Physiology, 2007. **454**(3): p. 345-359.

56. Zhou, F. and W.T. Huck, *Surface grafted polymer brushes as ideal building blocks for "smart" surfaces.* Phys Chem Chem Phys, 2006. **8**(33): p. 3815-23.

57. Chen, W.-L., et al., *50th Anniversary Perspective: Polymer Brushes: Novel Surfaces for Future Materials.* Macromolecules, 2017. **50**(11): p. 4089-4113.

58. Shen, Y., et al., *Multifunctioning pH-responsive nanoparticles from hierarchical self-assembly of polymer brush for cancer drug delivery.* AIChE Journal, 2008. **54**(11): p. 2979-2989.

59. Barbey, R., et al., *Polymer Brushes via Surface-Initiated Controlled Radical Polymerization: Synthesis, Characterization, Properties, and Applications.* Chemical Reviews, 2009. **109**: p. 5437–5527.

60. Alexander, S., *Adsorption of chain molecules with a polar head a scaling description.* Journal de Physique, 1977. **38**(8): p. 983 - 987.

61. Zhulina, E.B., O.V. Borisov, and V.A. Priamitsyn, *Theory of steric stabilization of colloid dispersions by grafted polymers.* Journal of Colloid and Interface Science, 1990. **137**(2): p. 495-511.

62. Gennes, P.D., *Scaling theory of polymer adsorption.* Journal de Physique, 1976. **37**: p. 1445-1452.

63. Currie, E.P.K., et al., *Structure of Monodisperse and Bimodal Brushes.* Macromolecules, 1999. **32**(26): p. 9041-9050.

64. Attili, S., O.V. Borisov, and R.P. Richter, *Films of end-grafted hyaluronan are a prototype of a brush of a strongly charged, semiflexible polyelectrolyte with intrinsic excluded volume.* Biomacromolecules, 2012. **13**(5): p. 1466-1477.

65. S. T. Milner, T.A.W., M. E. Cates, *Effects of Polydispersity in the End-Grafted Polymer Brush.* Macromolecules, 1989. **22**: p. 853-861.

66. Birshtein, T.M., Y.V. Liatskaya, and E.B. Zhulina, *Theory of supermolecular structures of polydisperse block copolymers: 1. Planar layers of grafted chains.* Polymer, 1990. **31**(11): p. 2185-2196.

67. de Vos, W.M. and F.A.M. Leermakers, *Modeling the structure of a polydisperse polymer brush.* Polymer, 2009. **50**(1): p. 305-316.

68. Israels, R., et al., *Charged Polymeric Brushes: Structure and Scaling Relations.* Macromolecules, 1994. **27**(12): p. 3249-3261.

69. A., H., T. M., and L. T.P., *Tethered chains in polymer microstructures. In: Macromolecules: Synthesis, Order and Advanced Properties,* in *Advances in Polymer Science*. 1992, Springer: Berlin, Heidelberg.

70. Pincus, P., *Colloid Stabilization with Grafted Polyelectrolytes.* Macromolecules, 1991. **24**: p. 2912-2919.

71. Cheesman, B.T., et al., *Polyelectrolyte brush pH-response at the silica-aqueous solution interface: a kinetic and equilibrium investigation.* Phys Chem Chem Phys, 2013. **15**(34): p. 14502-10.

72. V. A. Pryamitsyn, F.A.M.L., G. J. Fleer, E. B. Zhulina, *Theory of the Collapse of the Polyelectrolyte Brush.* Macromolecules, 1996. **29**: p. 8260-8270.

73. R. Israéls, F.A.M.L., and G. J. Fleer, *On the Theory of Grafted Weak Polyacids.* Macromolecules, 1994. **27**: p. 3087-3093.

74. Misra, S., S. Varanasi, and P.P. Varanasi, *A polyelectrolyte brush theory.* Macromolecules, 1989. **22**(11): p. 4173-4179.

75. Bracha, D., et al., *Entropy-driven collective interactions in DNA brushes on a biochip.* Proc Natl Acad Sci U S A, 2013. **110**(12): p. 4534-8.

76. Wynveen, A. and C.N. Likos, *Interactions between planar stiff polyelectrolyte brushes.* Physical Review E, 2009. **80**(1): p. 010801.

77. Wynveen, A. and C.N. Likos, *Interactions between planar polyelectrolyte brushes: effects of stiffness and salt.* Soft Matter, 2010. **6**(1): p. 163-171.

78. Fazli, H., et al., *Rod-like polyelectrolyte brushes with mono- and multivalent counterions.* Europhysics Letters (EPL), 2006. **73**(3): p. 429-435.

79. Günther, J.U., et al., *Bundle Formation in Polyelectrolyte Brushes.* Physical Review Letters, 2008. **101**(25): p. 258303.

80. Tlapak-Simmons, V.L., et al., *Kinetic characterization of the recombinant hyaluronan synthases from Streptococcus pyogenes and Streptococcus equisimilis.* Journal of Biological Chemistry, 1999. **274**(7): p. 4246-4253.

81. Markovitz, A., J.A. Cifonelli, and A. Dorfman, *The Biosynthesis of Hyaluronic Acid by Group A Streptococcus: VI. BIOSYNTHESIS FROM URIDINE NUCLEOTIDES IN CELL-FREE EXTRACTS.* Journal of Biological Chemistry, 1959. **234**(9): p. 2343-2350.

82. Baggenstoss, B.A. and P.H. Weigel, *Size exclusion chromatography–multiangle laser light scattering analysis of hyaluronan size distributions made by membrane-bound hyaluronan synthase.* Analytical Biochemistry, 2006. **352**(2): p. 243-251.

83. Dukes, D., et al., *Conformational transitions of spherical polymer brushes: synthesis, characterization, and theory.* Macromolecules, 2010. **43**(3): p. 1564-1570.

84. Heldin, P. and H. Pertoft, *Synthesis and Assembly of the Hyaluronan-Containing Coats around Normal Human Mesothelial Cells.* Experimental Cell Research, 1993. **208**(2): p. 422-429.

85. Cohen, M., et al., *Organization and Adhesive Properties of the Hyaluronan Pericellular Coat of Chondrocytes and Epithelial Cells*. Biophysical Journal, 2003. **85**(3): p. 1996-2005.

86. McLane, L.T., et al., *Spatial organization and mechanical properties of the pericellular matrix on chondrocytes.* Biophysical journal, 2013. **104**(5): p. 986-996.

87. Zoppe, J.O., et al., *Surface-Initiated Controlled Radical Polymerization: State-of-the-Art, Opportunities, and Challenges in Surface and Interface Engineering with Polymer Brushes.* Chemical Reviews, 2017. **117**(3): p. 1105-1318.

88. Vorobii, M., et al., *Synthesis of non-fouling poly [N-(2-hydroxypropyl) methacrylamide] brushes by photoinduced SET-LRP*. Polymer Chemistry, 2015. **6**(23): p. 4210-4220.

89. Button, B., et al., *A Periciliary Brush Promotes the Lung Health by Separating the Mucus Layer from Airway Epithelia.* Science, 2012. **337**(6097): p. 937.

90. Tan, K.Y., et al., *Study of thiol–ene chemistry on polymer brushes and application to surface patterning and protein adsorption.* Polymer Chemistry, 2016. **7**(4): p. 979-990.

91. Qi, S., *Particle Penetration into Polydisperse Polymer Brushes: A Theoretical Analysis.* Macromolecular Theory and Simulations, 2017. **26**(5).

92. Chang, P.S., et al., *Cell surface access is modulated by tethered bottlebrush proteoglycans.* Biophysical journal, 2016. **110**(12): p. 2739-2750.

93. Rivas, F., et al., *Label-free analysis of physiological hyaluronan size distribution with a solid-state nanopore sensor.* Nature Communications, 2018. **9**(1): p. 1037.

94. Jijin, Y., et al., *Rapid and precise scanning helium ion microscope milling of solid-state nanopores for biomolecule detection.* Nanotechnology, 2011. **22**(28): p. 285310.

95. Fologea, D., et al., *Detecting Single Stranded DNA with a Solid State Nanopore.* Nano Letters, 2005. **5**(10): p. 1905-1909.

96. Quinn, P., G. Griffiths, and G. Warren, *Density of newly synthesized plasma membrane proteins in intracellular membranes II. Biochemical studies.* The Journal of Cell Biology, 1984. **98**(6): p. 2142.

97. Ross, R.S. and P. Pincus, *The polyelectrolyte brush: poor solvent.* Macromolecules, 1992. **25**(8): p. 2177-2183.

98. Cowman, M.K. and S. Matsuoka, *Experimental approaches to hyaluronan structure.* Carbohydrate Research, 2005. **340**(5): p. 791-809.

99. Tlapak-Simmons, V.L., et al., *Purification and Lipid Dependence of the Recombinant Hyaluronan Synthases from Streptococcus pyogenes and Streptococcus equisimilis.* Journal of Biological Chemistry, 1999. **274**(7): p. 4239-4245.

100. Rivas, F., et al., *Label-free analysis of physiological hyaluronan size distribution with a solid-state nanopore sensor.* Nature communications, 2018. **9**(1): p. 1037-1037.

101. Frazier, S.B., et al., *The Quantification of Glycosaminoglycans: A Comparison of HPLC, Carbazole, and Alcian Blue Methods.* Open glycoscience, 2008. **1**: p. 31-39.

102. Guerrini, M., et al., *Complex glycosaminoglycans: profiling substitution patterns by two-dimensional nuclear magnetic resonance spectroscopy.* Analytical Biochemistry, 2005. **337**(1): p. 35-47.

103. Malvern, *Zetasizer Nano User Manual*, M.I. Limited, Editor. 2013: United Kingdom.

104. Lonza, *Section IV: Detection and Sizing of DNA in Agarose Gels*.

105. Yuan, H., et al., *Molecular mass dependence of hyaluronan detection by sandwich ELISA-like assay and membrane blotting using biotinylated hyaluronan binding protein.* Glycobiology, 2013. **23**(11): p. 1270-1280.

106. Haserodt, S., R.A. Aytekin M Fau - Dweik, and R.A. Dweik, *A comparison of the sensitivity, specificity, and molecular weight accuracy of three different commercially available Hyaluronan ELISA-like assays.* (1460-2423 (Electronic)).

107. *Quantikine®ELISA Hyaluronan Immunoassay*, *DHYALO*, I. R&D Systems, Editor. 2017. p. 16.

108. *Acclaim Size Exclusion Chromatography (SEC) Columns*, ThermoScientific, Editor. 2012.

109. Cesaretti, M., et al., *A 96-well assay for uronic acid carbazole reaction.* Carbohydrate Polymers, 2003. **54**(1): p. 59-61.

110. Blundell, C.D., et al., *Use of 15N-NMR to resolve molecular details in isotopically-enriched carbohydrates: sequence-specific observations in hyaluronan oligomers up to decasaccharides.* Glycobiology, 2004. **14**(11): p. 999-1009.

111. Harmita, H., H. Hayun, and M.H. Geofani, *Quantification of Hyaluronic Acid and Methylsulfonylmethane in Dietary Supplements.* International Journal of Applied Pharmaceutics, 2020: p. 143-148.

112. Izunobi, J.U. and C.L. Higginbotham, *Polymer Molecular Weight Analysis by 1H NMR Spectroscopy.* Journal of Chemical Education, 2011. **88**(8): p. 1098-1104.

113. *Synergy of Complementary Nanomaterial Characterization Techniques: NTA+DLS [White paper]*. 2016, Malvern Instruments Limited. p. 8.

114. Einstein, A., *Über die von der molekularkinetischen Theorie der Wärme geforderte Bewegung von in ruhenden Flüssigkeiten suspendierten Teilchen.* Annalen der Physik, 1905. **4**(17): p. 549-560.

115. Guettari, M., R. Gomati, and A. Gharbi, *Determination of the Flory Exponent by Study of Steady Shear Viscosity.* Journal of Macromolecular Science, Part B, 2011. **51**(1): p. 153-163.

116. Lakowicz, J.R., *Principles of Fluorescence Spectroscopy*

2nd ed. 1999, New York: Kluwer Academic/Plenum Publishers.

117. Katoh, R., et al., *Origin of the stabilization energy of perylene excimer as studied by fluorescence and near-IR transient absorption spectroscopy.* Journal of Photochemistry and Photobiology A: Chemistry, 2001. **145**: p. 23-24.

118. *Alexa dyes*. [cited 2019; Available from: https://www.atdbio.com/content/34/Alexa-dyes.

119. Madison, S.A. and J.O. Carnali, *pH Optimization of Amidation via Carbodiimides.* Industrial & Engineering Chemistry Research, 2013. **52**(38): p. 13547-13555.

120. *Amine-Reactive Crosslinker Chemistry*. [cited 2018; Available from: https://www.thermofisher.com/us/en/home/life-science/protein-biology/protein-biology-learning-center/protein-biology-resource-library/pierce-protein-methods/amine-reactive-crosslinker-chemistry.html.

121. Kolb, H.C., M.G. Finn, and K.B. Sharpless, *Click Chemistry: Diverse Chemical Function from a Few Good Reactions.* Angewandte Chemie International Edition, 2001. **40**: p. 2004 - 2021.

122. Moses, J.E. and A.D. Moorhouse, *The growing applications of click chemistry.* Chemical Society Reviews, 2007. **36**(8): p. 1249-1262.

123. de Ménorval, M.A., et al., *Effects of dimethyl sulfoxide in cholesterol-containing lipid membranes: a comparative study of experiments in silico and with cells.* (1932-6203 (Electronic)).

124. Xie, Z., et al., *Recent Progress in Creating Complex and Multiplexed Surface-Grafted Macromolecular Architectures.* Soft Matter, 2020. **16**(38): p. 8736-8759.

125. Zhou, X., et al., *3D-patterned polymer brush surfaces.* Nanoscale, 2011. **3**(12): p. 4929-4939.

126. Benetti, E.M., *Quasi-3D-Structured Interfaces by Polymer Brushes.* Macromolecular Rapid Communications, 2018. **39**(14).

127. Bhat, R.R., et al., *Surface-Grafted Polymer Gradients: Formation, Characterization, and Applications*, in *Surface-Initiated Polymerization II*, R. Jordan, Editor. 2006, Springer Berlin Heidelberg: Berlin, Heidelberg. p. 51-124.

128. Genzer, J., *Surface-Bound Gradients for Studies of Soft Materials Behavior.* Annual Review of Materials Research, 2012. **42**(1): p. 435-468.

129. Genzer, J. and R.R. Bhat, *Surface-Bound Soft Matter Gradients.* Langmuir, 2008. **24**: p. 2294-2317.

130. Bhat, R.R. and J. Genzer, *Combinatorial study of nanoparticle dispersion in surface-grafted macromolecular gradients.* Applied Surface Science, 2006. **252**(7): p. 2549-2554.

131. Chang Xu, T.W., Charles Michael Drain, James D. Batteas, Michael J. Fasolka, and Kathryn L. Beers, *Effect of Block Length on Solvent Response of Block Copolymer Brushes: Combinatorial Study with Block Copolymer Brush Gradients.* Macromolecules, 2006. **39**: p. 3359-3364.

132. Wu, T., K. Efimenko, and J. Genzer, *Combinatorial Study of the Mushroom-to-Brush Crossover in Surface Anchored Polyacrylamide.* Journal of the American Chemical Society, 2002. **124**: p. 9394-9395.

133. Wu, T., et al., *Behavior of Surface-Anchored Poly(acrylic acid) Brushes with Grafting Density Gradients on Solid Substrates: 1. Experiment.* Macromolecules, 2007. **40**: p. 8756-8764.

134. Zhao, B., *A Combinatorial Approach to Study Solvent-Induced Self-Assembly of Mixed Poly(methyl methacrylate)/Polystyrene Brushes on Planar Silica Substrates: Effect of Relative Grafting Density.* Langmuir, 2004. **20**: p. 11748-11755.

135. Bhat, R.R., M.R. Tomlinson, and J. Genzer, *Orthogonal surface-grafted polymer gradients: A versatile combinatorial platform.* Journal of Polymer Science Part B: Polymer Physics, 2005. **43**(23): p. 3384-3394.

136. Chen, T., et al., *Manipulating the Motion of Gold Aggregates Using Stimulus-Responsive Patterned Polymer Brushes as a Motor.* Advanced Functional Materials, 2012. **22**(2): p. 429-434.

137. Ren, T., et al., *Directional migration of vascular smooth muscle cells guided by a molecule weight gradient of poly(2-hydroxyethyl methacrylate) brushes.* Langmuir, 2013. **29**(21): p. 6386-95.

138. Benetti, E.M., et al., *Mimicking natural cell environments: design, fabrication and application of bio-chemical gradients on polymeric biomaterial substrates.* Journal of Materials Chemistry B, 2016. **4**(24): p. 4244-4257.

139. Mei, Y., et al., *Tuning Cell Adhesion on Gradient Poly(2-hydroxyethylmethacrylate)-Grafted Surfaces.* Langmuir, 2006. **21**: p. 12309-123014.

140. Ionov, L., et al., *Inverse and Reversible Switching Gradient Surfaces from Mixed Polyelectrolyte Brushes.* Langmuir, 2004. **20**: p. 9916-9919.

141. Oh, S.H., et al., *Investigation of Pore Size Effect on Chondrogenic Differentiation of Adipose Stem Cells Using a Pore Size Gradient Scaffold.* Biomacromolecules, 2010. **11**: p. 1948–1955.

142. Bhat, R.R., et al., *Controlling the assembly of nanoparticles using surface grafted molecular and macromolecular gradients.* Nanotechnology, 2003. **14**: p. 1145–1152.

143. Bhat, R.R., M.R. Tomlinson, and J. Genzer, *Assembly of Nanoparticles using Surface-Grafted Orthogonal Polymer Gradients.* Macromolecular Rapid Communications, 2004. **25**(1): p. 270-274.

144. Luzinov, I., S. Minko, and V.V. Tsukruk, *Responsive brush layers: from tailored gradients to reversibly assembled nanoparticles.* Soft Matter, 2008. **4**(4): p. 714-725.

145. Wang, X., et al., *Length Scale Heterogeneity in Lateral Gradients of Poly(N-isopropylacrylamide) Polymer Brushes Prepared by Surface-Initiated Atom Transfer Radical Polymerization Coupled with In-Plane Electrochemical Potential Gradients.* Langmuir, 2006. **22**: p. 817-823.

146. Schuh, C., et al., *Polymer Brushes with Nanometer-Scale Gradients.* Advanced Materials, 2009. **21**(46): p. 4706-4710.

147. Chen, T., R. Jordan, and S. Zauscher, *Dynamic microcontact printing for patterning polymer-brush microstructures.* Small, 2011. **7**(15): p. 2148-52.

148. Liu, X., Y. Li, and Z. Zheng, *Programming nanostructures of polymer brushes by dip-pen nanodisplacement lithography (DNL).* Nanoscale, 2010. **2**(12): p. 2614-8.

149. Steenackers, M., et al., *Engineered Polymer Brushes by Carbon Templating.* Advanced Materials, 2009. **21**(28): p. 2921-2925.

150. Higashi, J., et al., *High-Spatioresolved Microarchitectural Surface Prepared by Photograft Copolymerization Using Dithiocarbamate: Surface Preparation and Cellular Responses.* Langmuir, 1999. **15**: p. 2080-2088.

151. Liu, X., S. Guo, and C.A. Mirkin, *Surface and Site-Specific Ring-Opening Metathesis Polymerization Initiated by Dip-Pen Nanolithography*. Angewandte Chemie, 2003. **115**(39): p. 4933-4937.

152. Harris, B.P. and A.T. Metters, *Generation and Characterization of Photopolymerized Polymer Brush Gradients.* Macromolecules, 2006. **39**(8): p. 2764-2772.

153. Chen, T., I. Amin, and R. Jordan, *Patterned polymer brushes.* Chemical Society Reviews, 2012. **41**(8): p. 3280-96.

154. Zhang, J. and Y. Han, *Active and responsive polymer surfaces.* Chemical Society Reviews, 2010. **39**(2): p. 676-93.

155. Ducker, R., et al., *Polymeric and biomacromolecular brush nanostructures: progress in synthesis, patterning and characterization.* The Royal Society of Chemistry, 2008. **4**: p. 1774–1786.

156. Lin, X., Q. He, and J. Li, *Complex polymer brush gradients based on nanolithography and surface-initiated polymerization.* Chemical Society Reviews, 2012. **41**(9): p. 3584-93.

157. Zhou, X., et al., *Fabrication of arbitrary three-dimensional polymer structures by rational control of the spacing between nanobrushes.* Angewandte Chemie International Edition, 2011. **50**(29): p. 6506-10.

158. Ulbricht, M. and H. Yang, *Porous Polypropylene Membranes with Different Carboxyl Polymer Brush Layers for Reversible Protein Binding via Surface-Initiated Graft Copolymerization.* Chemistry of Materials, 2005. **17**: p. 2622-2631.

159. Saito, K., *Charged polymer brush grafted onto porous hollow-fiber membrane improves separation and reaction in biotechnology.* Separation Science and Technology, 2007. **37**(3): p. 535-554.

160. Mathieu, M., et al., *Surface-initiated polymerization on laser-patterned templates: morphological scaling of nanoconfined polymer brushes.* Langmuir, 2009. **25**(20): p. 12393-8.

161. Lee, W.K., et al., *Scaling behavior of nanopatterned polymer brushes.* Small, 2007. **3**(1): p. 63-6.

162. Neurath, H., J.P. Greessteis, and F.W.E. Putnam, John O., *The Chemistry of Protein Denaturation.* Chemical Reviews, 1943. **34**: p. 157-265.

163. Lavi, R., et al., *Detailed analysis of reactive oxygen species induced by visible light in various cell types.* Lasers in Surgery and Medicine, 2010. **42**(6): p. 473-80.

164. de Jager, T.L., A.E. Cockrell, and S.S. Du Plessis, *Ultraviolet Light Induced Generation of Reactive Oxygen Species*, in *Ultraviolet Light in Human Health, Diseases and Environment*, S.I. Ahmad, Editor. 2017, Springer International Publishing: Cham. p. 15-23.

165. Gracy, R.W., et al., *Reactive oxygen species: the unavoidable environmental insult?* Mutation Research, 1999. **428**: p. 17-22.

166. Hayyan, M., M.A. Hashim, and I.M. AlNashef, *Superoxide Ion: Generation and Chemical Implications.* Chemical Reviews, 2016. **116**(5): p. 3029-85.

167. Araki, T. and H. Kitaoka, *The Mechanism of Reaction of Ebselen with Superoxide in Aprotic Solvents as Examined by Cyclic Voltammetry and ESR.* Chemical and Pharmaceutical Bulletin, 2001. **49**(5): p. 541-545.

168. Li, R., et al., *Surface Oxidation of Graphene Oxide Determines Membrane Damage, Lipid Peroxidation, and Cytotoxicity in Macrophages in a Pulmonary Toxicity Model.* ACS Nano, 2018. **12**(2): p. 1390-1402.

169. Maisin, J.R. and G. Mattelin, *Reduction in Radiation Lethality by Mixtures of Chemical Protectors.* Nature, 1967. **214**: p. 207-208.

170. Bick, Y.A.E. and W.D. Jackson, *Chemical Protection against X-irradiation by a New Reducing Agent 1,4-Dithiothreitol in Marsupial Leucocytes in Culture.* Nature, 1968. **217**: p. 479-480.

171. Duan, J. and D.L. Kasper, *Oxidative depolymerization of polysaccharides by reactive oxygen/nitrogen species.* Glycobiology, 2011. **21**(4): p. 401-9.

172. Soltes, L., et al., *Degradative Action of Reactive Oxygen Species on Hyaluronan.* Biomacromolecules, 2006. **7**: p. 659-668.

173. Huang, Y.C., et al., *Gamma-Irradiation-Prepared Low Molecular Weight Hyaluronic Acid Promotes Skin Wound Healing.* Polymers (Basel), 2019. **11**(7).

174. Hafsa, J., et al., *Effect of ultrasonic degradation of hyaluronic acid extracted from rooster comb on antioxidant and antiglycation activities.* Pharmaceutical Biology, 2017. **55**(1): p. 156-163.

175. Burdick, J.A. and G.D. Prestwich, *Hyaluronic acid hydrogels for biomedical applications.* Adv Mater, 2011. **23**(12): p. H41-56.

176. Chow, D.C., et al., *Enzymatic Fabrication of DNA Nanostructures: Extension of a Self-assembled Oligonucleotide Monolayer on Gold Arrays.* Journal of the American Chemical Society, 2005. **127**: p. 14122-14123.

177. Galvin, C.J. and J. Genzer, *Applications of surface-grafted macromolecules derived from post-polymerization modification reactions.* Progress in Polymer Science, 2012. **37**(7): p. 871-906.

178. Klemm, D., et al., *Bacterial synthesized cellulose - artificial blood vessels for microsurgery.* Progress in Polymer Science, 2001. **21**: p. 1561-1603.

179. Borisov, O.V., E.B. Zhulina, and T.M. Birshtein, *Diagram of the States of a Grafted Polyelectrolyte Layer.* Macromolecules, 1994. **27**(17): p. 4795-4803.

180. Chen, L., et al., *Polyelectrolyte Brushes: Debye Approximation and Mean-Field Theory.* Macromolecules, 2011. **44**(8): p. 3109-3116.

181. Williams, D., *Grafted polymers in bad solvents: octopus surface micelles.* JOURNAL DE PHYSIQUE II, 1993. **3**: p. 1313-1318.

182. Lago, G., et al., *Isolation, purification and characterization of Hyaluronan from human umbilical cord residues.* Carbohydrate Polymers, 2005. **62**: p. 321-326.

183. Yang, P.-F. and C.-K. Lee, *Hyaluronic acid interaction with chitosan-conjugated magnetite particles and its purification.* Biochemical Engineering Journal, 2007. **33**(3): p. 284-289.

184. Gao, G., et al., *The biocompatibility and biofilm resistance of implant coatings based on hydrophilic polymer brushes conjugated with antimicrobial peptides.* Biomaterials, 2011. **32**(16): p. 3899-3909.

185. Nejadnik, M.R., et al., *Bacterial adhesion and growth on a polymer brush-coating.* Biomaterials, 2008. **29**(30): p. 4117-4121.

186. Hadjesfandiari, N., et al., *Polymer brush-based approaches for the development of infection-resistant surfaces.* Journal of Materials Chemistry B, 2014. **2**(31): p. 4968-4978.

187. Yu, K., et al., *Anti-adhesive antimicrobial peptide coating prevents catheter associated infection in a mouse urinary infection model.* (1878-5905 (Electronic)).

188. Dieter, R.S., *Coronary Artery Stent Infection.* Catheterization and Cardiovascular Interventions, 2000. **23**: p. 808-810.

189. Graber, D. and R.H. Dailey, *Catheter flow rates updated.* Journal of the American College of Emergency Physicians, 1977. **6**: p. 518.

190. Ramanathan, T. and H. Skinner, *Coronary blood flow.* Continuing Education in Anaesthesia Critical Care & Pain, 2005. **5**(2): p. 61-64.

191. Schroeder, C.M., *Single polymer dynamics for molecular rheology.* Journal of Rheology, 2018. **62**(1): p. 371-403.

192. Chu, S., *Laser Manipulation of Atoms and Particles.* Science, 1991. **253**(5022): p. 861.

193. Chu, S. and S. Kron. *Optical manipulation of DNA.* in *International Quantum Electronics Conference*. 1990. Anaheim, California: Optical Society of America.

194. Quake, S.R. and A. Scherer, *From Micro- to Nanofabrication with Soft Materials.* Science, 2000. **290**(5496): p. 1536.

195. Perkins, T.T., et al., *Stretching of a single tethered polymer in a uniform flow.* Science, 1995. **268**(5207): p. 83.

196. Smith, D.E. and S. Chu, *Response of Flexible Polymers to a Sudden Elongational Flow.* Science, 1998. **281**(5381): p. 1335.

197. Doyle, P., B. Ladoux, and J.-L. Viovy, *Dynamics of a Tethered Polymer in Shear Flow.* Physical review letters, 2000. **84**: p. 4769-72.

198. Harden, J.L. and M.E. Cates, *Deformation of grafted polymer layers in strong shear flows.* Phys Rev E Stat Phys Plasmas Fluids Relat Interdiscip Topics, 1996. **53**(4): p. 3782-3787.

199. Ivkov, R., et al., *Effect of Solvent Flow on a Polymer Brush: A NeutronReflectivity Study of the Brush Height and Chain DensityProfile.* Langmuir, 2001. **17**: p. 2999-3005.

200. S. M. Baker, G.S.S., D. L. Anastassopoulos, C. Toprakcioglu, A. A. Vradis, andD. G. Bucknall, *Structure of Polymer Brushes under Shear Flow in a Good Solvent.* Macromolecules, 2000. **33**: p. 1120-1122.

201. Miao, L., H. Guo, and M.J. Zuckermann, *Conformation of Polymer Brushes under Shear: Chain Tilting and Stretching.* Macromolecules, 2006. **29**: p. 2289-2297.

202. Shashishekar P. Adiga, a.D.W.B., *Flow Control through Polymer-Grafted Smart Nanofluidic Channels: Molecular Dynamics Simulations.* Nano Letters, 2005. **5**(12).

203. Grest, G.S., *Polymer Brushes in Strong Shear Flow.* MRS Proceedings, 2011. **464**.

204. Deng, M., et al., *Simulation and modelling of slip flow over surfaces grafted with polymer brushes and glycocalyx fibres.* J Fluid Mech, 2012. **711**.

205. Anastassopoulos, D.L., et al., *Shear-induced desorption in polymer brushes.* Macromolecules, 2006. **39**(26): p. 8901-8904.

206. Müller, M. and C. Pastorino, *Cyclic motion and inversion of surface flow direction in a dense polymer brush under shear.* EPL (Europhysics Letters), 2007. **81**(2): p. 28002.

207. Lanotte, L., et al., *Flow reduction in microchannels coated with a polymer brush.* Langmuir, 2012. **28**(38): p. 13758-64.

208. Qi, S., et al., *Polydisperse Polymer Brushes: Internal Structure, Critical Behavior, and Interaction with Flow.* Macromolecules, 2016. **49**(24): p. 9665-9683.

209. Milner, S.T., *Hydrodynamic penetration into parabolic brushes.* Macromolecules, 1991. **24**(12): p. 3704-3705.

210. Binder, K., T. Kreer, and A. Milchev, *Polymer brushes under flow and in other out-of-equilibrium conditions.* Soft Matter, 2011. **7**(16).

211. Price, R.D., et al., *The role of hyaluronic acid in wound healing.* American journal of clinical dermatology, 2005. **6**(6): p. 393-402.

212. Liu, X., et al., *Grafting hyaluronic acid onto gold surface to achieve low protein fouling in surface plasmon resonance biosensors.* ACS applied materials & interfaces, 2014. **6**(15): p. 13034-13042.

213. Ombelli, M., et al., *Competitive protein adsorption on polysaccharide and hyaluronate modified surfaces.* Biofouling, 2011. **27**(5): p. 505-518.

214. Park, Y.D., N. Tirelli, and J.A. Hubbell, *Photopolymerized hyaluronic acid-based hydrogels and interpenetrating networks.* Biomaterials, 2003. **24**(6): p. 893-900.

215. Glass, J.R., et al., *Characterization of a hyaluronic acid-Arg-Gly-Asp peptide cell attachment matrix.* Biomaterials, 1996. **17**(11): p. 1101-1108.

216. Chua, P.-H., et al., *Surface functionalization of titanium with hyaluronic acid/chitosan polyelectrolyte multilayers and RGD for promoting osteoblast functions and inhibiting bacterial adhesion.* Biomaterials, 2008. **29**(10): p. 1412-1421.

VITA

Jessica Faubel was born and grew up in Georgia, USA. She received her Bachelor of Science in Physics from North Georgia College & State University in 2010. She began teaching high school science at her alma mater, Forsyth Central High School, in 2011. She attained her Master of Arts in Teaching from North Georgia College & State University in 2012. During her time at Forsyth Central High School, she was a teacher in the STEM Academy and helped the program receive state certification. She began her pursuit of her PhD in Physics at The Georgia Institute of Technology in 2016 and joined Dr. Jennifer E. Curtis' lab in 2017. During her time at The Georgia Institute of Technology, she received the President's Fellowship, 2018 STAMI Scientific Travel Award, 2018 Amelio Fund Travel Award, 2019 International Society of Hyaluronan Sciences (ISHAS) Travel Award, 2019 Amelio Fund Travel Award, 2019 Science and Technology of Advanced Materials and Interfaces (STAMI) Graduate Fellowship, and the 2019 Charles K. Rice Fellowship. She received her PhD in 2021.